# Università degli studi di Genova

**Scuola Politecnica**

**PhD Course in Science and Technology for Electrical Engineering, Marine Engineering and Complex Systems for Mobility: XXXII Cycle**

# Lightning-induced voltages on power lines: advances in modelling , computational effort optimization and innovative tools for the protection of overhead distribution lines


Advisor:

Prof. Renato Procopio

Candidate:

Eng. Daniele Mestriner

***"The noblest pleasure is the joy of understanding"***

***(Leonardo da Vinci)***

# Thanks

This work and this experience would never have been realized without the support and the love of my parents. My mother is giving me every day the unconditional support and silent force, which has helped me to become adult. My father has donated all his life trying to teach me the humility and the tenacity in everyday efforts. I will always thank them for this.

A special mention shall be done to my Professor, Renato Procopio: a leader, and not a boss, that has taught and provided me the methods to grow as a researcher and as a person.

How to forget the people of the NICES Laboratory, DITEN and IEE, which has helped me in many situations. It is impossible to mention you all, thank you for the long talks, exchange of ideas and laughs done together.

I want to thank all my friends who has supported me in these years and which are walking with me in all the experiences of my life. They are unified by two colours: the red and the white. Thank you people from Cus Genova and Dinamo PNI.

Last but not least, how can I forget Elisabetta. Thank you for every second spent with me. *"The most beautiful words of love are told in silence for a look"*

# Abstract

The continuous growth of MV overhead distribution systems requires a constant improvement in terms of security and power quality. One of the most critical event that can cause the fault of a distribution line is represented by the atmospheric discharges and, among them, the most dangerous one is no-doubt the lightning stroke.

In the transmission and distribution systems, lightning transients can be caused by either direct or indirect strikes. Indirect strikes are much more frequent than direct strikes and can cause flashovers, especially when the line insulation level is low.

The computation of the lightning induced-voltages (i.e. the one related to the indirect strikes, which represent the most critical issue in distribution systems) is a very complicated task for two main reasons: 1) the number of uncertain parameters is high: it involves a correct representation of the current that flows in the lightning channel as well as a correct representation of the soil conductivity where the power line is located. 2) The computational complexity of the calculations that allow evaluating the final overvoltage is high because in this case we are dealing with the computation of electromagnetic fields and with the effect of such fields on the power line.

Concerning the protecting measures the most widely employed are the use of shield wires, surge arresters and the increase of the line insulation level.

This thesis aims at improving the problem of the lightning-induced voltages in overhead distribution lines in terms of three main concepts: 1) innovation of the existing models, 2) optimization of the computational effort and 3) introduction of innovative tools for the protecting scheme. In this framework, the thesis proposes a new channel-bae current model (1), an analytical technique for the electromagnetic fields computation (2), a new scheme for the lightning-induced voltages computation (2), a new approach for reducing the computational effort of the lightning performance computation (2 and 3) and an innovative approach for the evaluation of the mitigation effect of shield wires on the lightning-induced voltages (3).

# Table of Contents

# 1 Introduction

The continuous growth of medium voltage (MV) overhead distribution systems requires a constant improvement in terms of security and power quality. One of the most critical events that can cause the fault of a distribution line is represented by the atmospheric discharges and, among them, the most dangerous one is no-doubt the lightning stroke. In MV overhead distribution systems, lightning transients can be caused by two main categories: direct and indirect strokes. The first category represents that type of lightning events that directly hit the power line, while the second category represents the ones striking the ground around the distribution line, causing possible overvoltages due to the coupling effect with the electromagnetic fields. Direct strikes are obviously much more dangerous although less probable, while indirect strikes are much more frequent than direct strikes and can cause flashovers especially when the line insulation level is low [1]. Direct strikes are modelled placing a current source taking the channel base current in parallel with the channel impedance in the point of the line in which the lightning is supposed to strike, while the computation of the effect of indirect strikes is much more complicated and takes into account many different aspects and parameters.

The computation of the lightning induced-voltages is a very complicated task for two main reasons: 1) the number of uncertain parameters is high: it involves a correct representation of the current that flows in the lightning channel as well as a correct representation of the soil conductivity where the power line is located (Section 1.1). 2) The computational complexity of the calculations that allow evaluating the final overvoltage is high because in this case we are dealing with the computation of electromagnetic fields and with the effect of such fields on the power line (Sections 1.2 and 1.3).

The goal of the evaluation of lightning-induced voltages is no-doubt the protection of overhead distribution lines. As proposed in Section 1.4 the main protecting techniques are based on the installation of surge arresters and shield wires, while the most important instrument for the evaluation of the effectiveness of such protecting techniques is the lightning performance procedure (Section 1.5).

## 1.1 The lightning current

The representation of the current flowing in the lightning channel has been an important topic involving many researchers. Different approaches have been presented in literature to model such current. According to [2], they can be divided into four categories:

1) Gas dynamic or physical models [3-5] which require the solution of three hydrodynamic equations representing the conservation of mass, momentum and energy and coupled to two equations of state with the input parameter being an assumed channel current versus time.
2) Electromagnetic models that consider the lightning channel as a lossy thin wire antenna [6, 7]. The solution of the resulting Maxwell equations (typically performed by means of the method of moments) provides the complete channel current (that is to say including both transmission line mode and antenna mode current [8])
3) Distributed circuit models which are an approximation of the electromagnetic models and adopt the telegrapher equations to represent the lightning channel[8]. The major limitation of this model is that analytical solutions are available only in the case of constant per-unit-length parameters, which is not the case of the lightning channel. Moreover, the validity of the Transverse Electro-Magnetic (TEM) assumption is questionable in particular near the return stroke tip where a relatively large longitudinal component of the electric field is present
4) Engineering models that basically provide an equation relating the channel current $I(z',t)$ at any time *t* and height $z'$ to the channel base current $I(0,t)$ .

For the purpose of the overvoltage analysis, the engineering models are the most widely adopted because of the compromise they guarantee between computational efforts and ability to adequately represent the electromagnetic fields at low to medium distances.

As mentioned and as will be shown in Section 2.1, the common idea is based on dividing the representation of the current in two main parts: i) the behaviour at the channel-base and ii) its propagation while it flows along the channel. Concerning the first issue, it has been possible to obtain reliable data thanks to the measurements obtained in different countries [9-13] and thanks to triggered lightning experiments [14]; according to these measurements many models have been developed trying to represent the channel-base current in an accurate and fast way [15-18]. The representation of the propagation along the lightning channel is a much more problematic task. This is mainly due to the fact that up to now it is not possible to measure what happens inside the lightning channel. The main idea of the researchers has been to try to invent a model representing how the current propagates along the channel that can match as well as possible the electromagnetic fields measurements. This task has led to the definition of many different models [19].

## 1.2 The electromagnetic fields

As will be proposed in Section 2.2 a first possibility for the computation of the electromagnetic fields is to assume that the ground is a perfect conductor and the lightning channel is vertical; in these conditions, expressions for the electromagnetic fields involving an integral over the channel have been derived both in the frequency and in the time domain [20, 21]. However, it has been shown that the ground finite conductivity plays an important role especially in the evaluation of the radial component of the electric field. The exact expressions of the field in presence of a lossy ground involves the so-called Sommerfeld integrals, whose exact computation, performed in [22-24], results prohibitive from a computational point of view. For this reason, an approximate approach has been proposed by Cooray and Rubinstein in [25, 26] in the frequency domain and then some alternative expressions in the time domain have been presented in [27-30]. However, to evaluate the overvoltage generated by one lightning strike on a line it is necessary to calculate the radial component of the electric field in the points in which the line is discretized and the vertical component of the electric field at the line extremities [31]. Moreover, when one aims at evaluating the lightning performance of a distribution system (Section 1.5), a statistical analysis has to be conducted according to which some thousands of lightning events have to be randomly generated characterized by different points of impact and different parameters of the channel base current [32-35]. From these considerations it is apparent that a huge number of field calculations is required, which makes the computational performance of such calculation a crucial aspect for this kind of application. In literature many approaches have faced this problem: in [36], analytical expressions for the fields were developed relying on the assumption of trapezoidal channel base current, while on the other hand in [35] a field database was developed. Unfortunately, the first solution can generate unacceptable deviations especially when the presence of surge arresters and flashovers occurrence is taken into account [37]. On the other hand, the field database does not completely solve the computational problems, because when one has to account for the main features of the channel base current waveform, the dimension of the database would be prohibitive.

## 1.3 The lightning-induced voltages

Once the electromagnetic fields are known, their effect on the power lines must be computed. Many models have been developed since 1957 [38], but the most commonly-used TL-based model to describe lightning electromagnetic fields coupling to overhead lines is the one proposed by Agrawal et al. in 1980 [31]. Since then, different implementations of this model have been proposed in literature that can be basically divided into two categories: analytical [39-44] and numerical [34, 35, 45-50]. The most popular methods belonging to the analytical

group are [40-44], where a mixed time-domain/frequency-domain approach is proposed. Many different approaches have been proposed on the numerical side, but the most widely employed computer code is LIOV [45-47] that has been improved over time in order to take into account more complex distribution systems [48]. LIOV has been interfaced both with EMPT-RV and with SymPower Systems program in the MATLAB Simulink environment. Recently, an advanced coupling code that can be interfaced with the PSCAD-EMTDC platform has been developed by the researchers of the University of Genoa [34, 35].

## 1.4 Protection of MV overhead distribution lines

The protection of MV overhead distribution lines from the lightning-induced voltages has been faced in many IEEE and CIGRE standards [1, 51] as well as in many research papers. The main protective measures against short interruptions and voltage sags can be identified as 1) increasing of the line insulation level and/or 2) the use of shielding wires and/or 3) the use of surge arresters.

### 1.4.1 Line insulation level

As pointed out in [1], the estimation of the line insulation level is not an easy task due to the atmospheric conditions (air density, humidity, rainfall), the polarity and rate of rise of the voltages and physical factors such as insulator shape, shape of metal hardware and insulator configuration. The total line insulation level (also known as Critical Flashover Voltage-CFO) of a distribution structure can be estimated by the knowledge of the contribution of each additional insulation component to the total CFO of the combination and by estimating the total CFO of the combination knowing the CFO of the insulation components.

### 1.4.2 Shield wires

The experience in using shield wires in MV distribution systems has been successful in the USA and South America thanks also to their combined use with surge arresters that provide complementary protection [1]. In some European countries, such as Italy, the introduction of shield wires is generally not used in MV distribution networks even though their effectiveness have been shown in some studies (e.g., [52]). Many papers have dealt with the use of shield wires, discussing the effect of parameters such as the distance between two subsequent grounding points [38, 53, 54], or presenting experimental results to assess their effectiveness [55-58]. The studies presented in [54] have focused on the parameters that affect the effectiveness of shield wires on the mitigation of lightning-induced voltages. The results obtained have demonstrated that the most relevant ones are the relative position of the shield

wire with respect to the phase conductors, the grounding interval and the ground resistance, but a thorough analysis is still missing.

### 1.4.3 Surge arresters

Arresters may be used to protect distribution line insulation by reducing the occurrence of flashovers and circuit interruptions. Several different types of arresters, such as internally gapped silicon carbide, internally, externally or non-gapped metal-oxide, have been used over time. From the point of view of protection, all perform in a similar manner. Differences in discharge voltage characteristics will cause only a small difference in the protection of insulation [1].

## 1.5 Lightning performance of overhead distribution lines

In order to evaluate the effectiveness of the aforementioned protection strategies, it is necessary to find adequate instruments.

One of the most important instrument for the protection of overhead distribution lines is represented by the lightning performance procedure.

The lightning performance procedure provides, for a power line, the number of dangerous events per square kilometer per year. In order to evaluate it is extremely important to have reliable data in terms of the parameters that characterize a lightning stroke and its incidence on the territory where the line is located. Among them, it is important to cite the peak current, the front duration, the maximum steepness, the total charge, the time-to-half value and the Ground Flash Density (GFD).

In literature many approaches have been proposed [1, 32-34, 59], but all of them rely on the same procedure based on the Monte-Carlo method, here briefly recalled:

1. A large number of lightning events is randomly generated
2. Each event is characterized by a point of impact, a channel-base peak current, front duration, maximum steepness, total charge and time-to-half value according to the probability density functions (PDF) taken into account.
   It is important to remind that usually the point of impact coordinates are uniformly distributed, while the other parameters follow the PDFs of the measurements [9]. In principle all the aforementioned parameters should follow their PDF, but usually the maximum steepness, the total charge and the time-to-half-value are not taken into account in the Monte-Carlo procedure and thus considered as constant values.
3. The ElectroGeometric Model (EGM) [60] distinguishes if the selected event is a direct or indirect stroke.

4. The overvoltage on the distribution line is computed. If it is a direct event, the computation procedure is simple and based on placing a current source taking the channel-base current in parallel with the channel impedance in the point of the line in which the lightning is supposed to strike. If the event is indirect, the computation is not an easy task and can be evaluated with a simplified formula [38] or with dedicated codes as mentioned in Section 1.3.
5. The overvoltage is compared with the line CFO and considered as dangerous if it overcomes that threshold.
6. The ratio between the number of dangerous events and the total number of events is computed and multiplied by the GFD.

It is important to remind that, in order to have a good convergence of the Monte-Carlo method, a high number of events is usually considered (>10000). This leads to an important problem in terms of computational effort, especially because each time that a different front duration is considered from the Monte-Carlo procedure, it is necessary to evaluate again the electromagnetic fields, which represent the most cumbersome part.

## 1.6 The goal of the proposed work

This thesis aims at improving the problem of the lightning-induced voltages in the overhead distribution lines in terms of three main concepts:

- Models innovation
- Computational effort optimization
- Introduction of innovative tools

### 1.6.1 Models innovation

#### *1.6.1.1 A new channel-base current*

According to Section 1.1, many models have been already introduced for describing the channel-base current. However, as described in the next paragraphs, each one of them has some advantages and disadvantages that need to be discussed deeply. This has led the author to introduce a new model for the channel-base current able to adequately describe the measurements with a few number of parameters. Section 2.1 describes deeply the existing models, while Section 3 introduces the theory of the new proposed model with the validation against the already existing ones.

### 1.6.2 Computational effort optimization

#### *1.6.2.1 Electromagnetic fields computation*

The computation of electromagnetic fields is probably the most cumbersome part in the lightning performance computation and more in generally, when one has to face the lightning-induced voltages problem. The well-known approach requires, for each time step, the solution of the integrals in the channel vertical coordinate (Section 2.2). In Section 4 a new approach, based on few assumptions is proposed and validated with the traditional method, focusing on the important reduction of the computational efforts.

#### *1.6.2.2 A new scheme for the lightning-induced voltages computation*

The majority of the codes for the lightning induced voltages computation are based on the 2D-FDTD schemes [61, 62]. The FDTD schemes are mainly based on the discretization of the problem in two dimensions: the space and the time. As will be proposed in Section 2.3.2, these schemes can be useful, but presents some limits that can introduce numerical instability. In order to overcome these limits, the most used technique is based on decreasing the time discretization step, which enlarges the computational effort. In Section 5 a possible solution for such numerical problems will be proposed and validated guaranteeing a decreasing of the computational effort with respect to the classical methods.

#### *1.6.2.3 A new approach for reducing the computational effort of the lightning performance computation*

As proposed in Section 1.5, the lightning performance requires a high computational effort, because for each power line, it is necessary to generate a high number of events in order to have a good convergence of the Monte-Carlo procedure.

In section 6, a methodology for reducing the computational effort of the lightning performance procedure is proposed and validated against the traditional method. The results will show that the proposed approach have the same validity of the most cumbersome methods.

### 1.6.3 Introduction of innovative tools

#### *1.6.3.1 A innovative approach for the evaluation of the mitigation effect of shield wires on lightning-induced voltages*

One of the most important protecting measurements against lightning-induced voltages is the shield wire (Section 1.4.2). Its effectiveness depends on many parameters, such as the height, the grounding interval, the grounding resistance and the position of the shield wire with respect to the phase conductors. The individual effect of each parameters is well described in [1, 54, 63] but a thorough analysis is still missing. In section 7 a new tool for evaluating the

effectiveness of such parameters on the ability of reduction lightning-induced voltages is proposed.

# 2 State of the art

The aim of this chapter is to describe the state of the art in the lightning-induced voltages theory starting from the models for the description of the lightning current, focusing on the computation of the electromagnetic fields with the traditional technique and finally concluding with the theory of the field-to-line coupling and its numerical implementation.

## 2.1 The lightning return stroke current

As mentioned in Section 1.1, the most-used representation for the lightning return stroke current in the engineering application is the engineering model. From now onwards, for sake of brevity, it will be referred to the lightning return stroke current as the "lightning current". In other, words, as commonly admitted, the electromagnetic radiation from lightning channel is essentially due to the return stroke phase.

An engineering model disregards the physics of the lightning processes and aims at producing lightning electromagnetic field results at various distances from the lightning stroke as close as possible to the experimentally measured ones, just by using a simple mathematical formulation of the lightning channel current and applying basic electromagnetic theory relations.

The necessity of such type of model is mandatory because the other three categories require a wide computational effort to evaluate the channel current while for the engineering models the lightning current is achieved just by knowing the channel base current time domain waveform and employing a small number of adjustable parameters.

According to [64, 65], the engineering models can be grouped into two broad categories:

- the Transmission Line type models
- the Traveling Current Source type models

In the following subsections, the main features of the two groups are briefly recalled.

### 2.1.1 Engineering models

#### *2.1.1.1 Transmission Line Type Models*

Transmission line type models assume that the channel current $I(z', t)$ is a function of height $z'$ and time $t$ which depends on the channel-base current $I_0(t) = I(0,t)$ and on the attenuation function $P(z')$. The channel current is given by:

$$I(z',t) = I_0\left(t - \frac{z'}{v}\right)P(z')u\left(t - \frac{z'}{v_f}\right) \tag{1}$$

being $u(t)$ the Heaviside unit function, $v_f$ the return stroke speed and $v$ the current wave propagation speed.

The most widely employed models belonging to this group are:

- TL model [66], according to which $v=v_f$ and $P(z')=1$
- MTLL model [67], according to which $v=v_f$ and $P(z')=1-\frac{z'}{H}$
- MTLE model [68], according to which $v=v_f$ and $P(z')=\exp\left(-\frac{z'}{\lambda}\right)$, $\lambda$ being the current decay factor

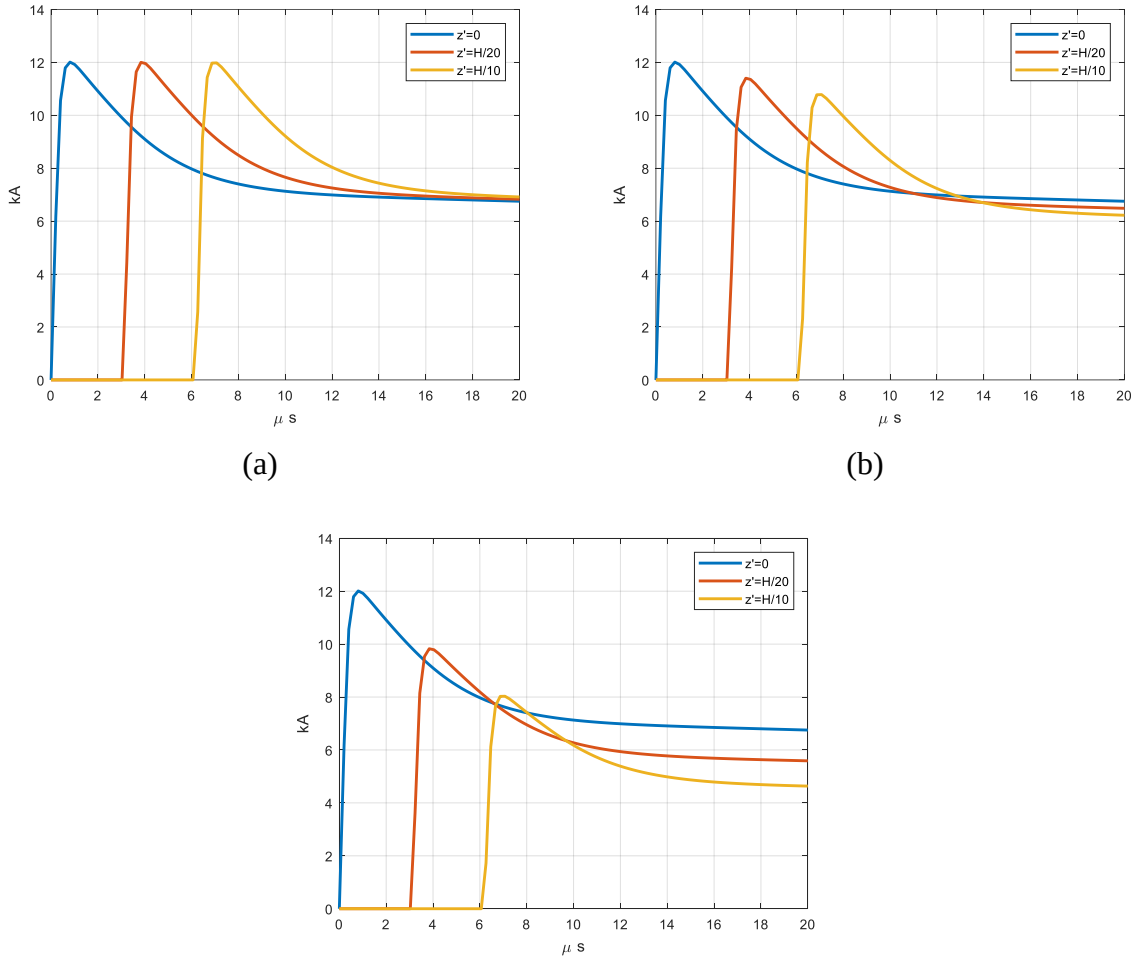


**Figure 1 propagation of the current along the channel according to the TL model (a), the MTLL model (b) the MTLE model (c). Channel-base waveform adopted: Heidler's first stroke [15].**

In Figure 1 an illustration of the propagation of the current along the channel according to the three above models is presented, highlighting the attenuation predicted by the MTLL and the MTLE with respect to the TL.

In [69] other four models that differ from the previous ones for the expression of the attenuation function *P* have been presented.

- MTLTCOS model, according to which $v=v_f$ and $P(z') = 0.95 - 0.95\frac{z'}{H} + 0.05\cos\left(5\pi\frac{z'}{H}\right)$
- MTLTSIN model according to which $v=v_f$ and $P(z') = 1 - \frac{z'}{H} - 0.1\sin\left(\frac{3\pi z'}{H}\right)$
- MTLT model, according to which $v=v_f$ and $P(z') = 0.5\left[1+\left(1-2\frac{z'}{H}\right)^3\right]$
- MTLT2 model, according to which $v=v_f$ and $P(z') = 0.25\left[1+\left(1-2\frac{z'}{H}\right)^3\right]^2$

In Figure 2 an illustration of the propagation of the current along the channel is sketched according to the four models proposed in [69].

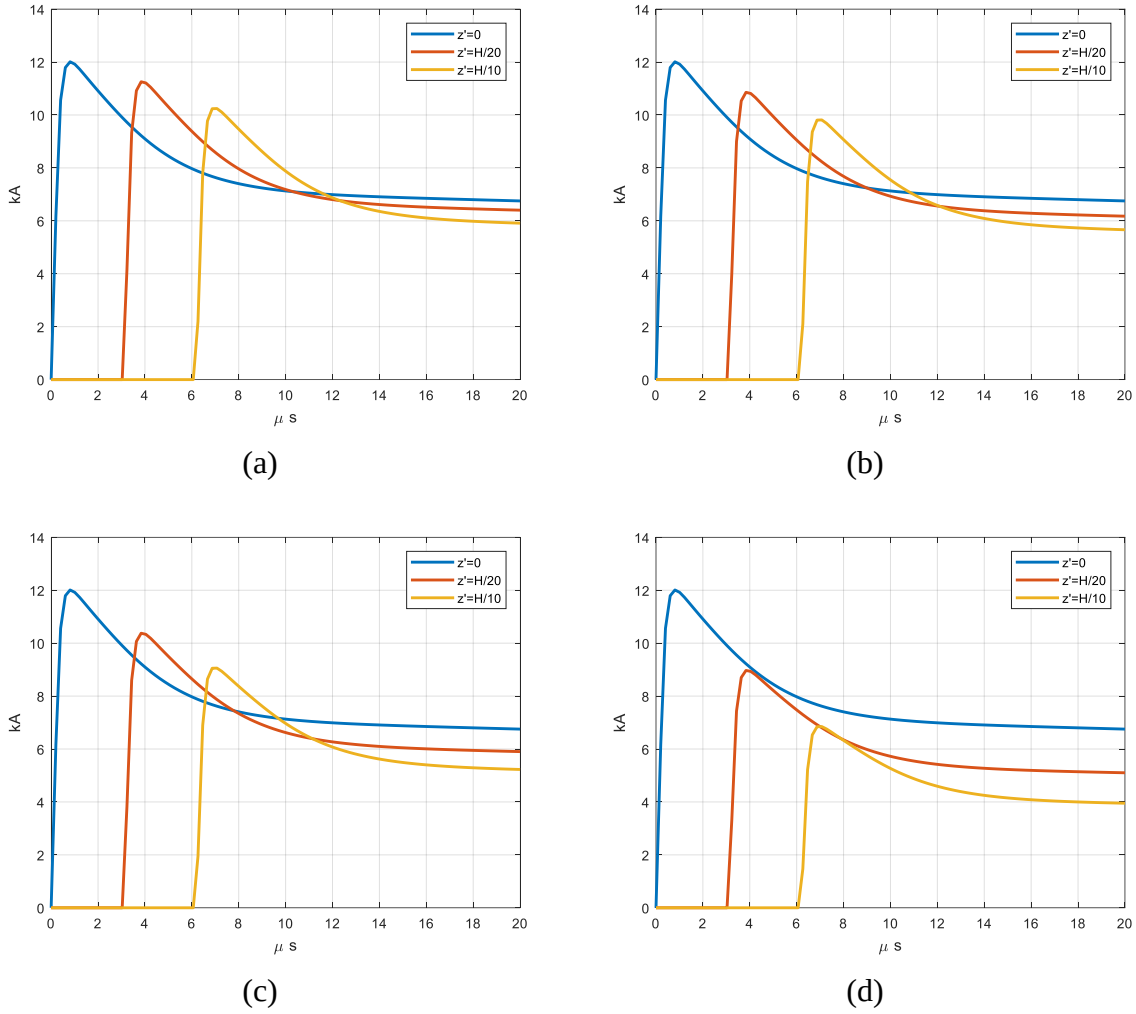


**Figure 2 propagation of the current along the channel according to the MTLTCOS model (a), MTLTSIN model (b) the MTLT model (c) the MTLT2 model (d). Channel-base waveform adopted: Heidler's first stroke [15].**

### *2.1.1.2 Traveling Current Source Type Models*

The basic idea of these models is that the return stroke current is generated at the upward moving return stroke front and propagates downward. The most widely employed models belonging to this category are:

- The BG model[2], which assumes that:

$$I(z',t) = I_0(t)\,u\left(t - \frac{z'}{v_f}\right) \tag{2}$$

- The TCS model [70] proposed by Heidler according to which:

$$I(z',t) = I_0\left(t + \frac{z'}{c}\right)u\left(t - \frac{z'}{v_f}\right) \tag{3}$$

- The DU model proposed by Diendorfer and Uman in [71]

$$I(z',t) = \left[I_0\left(t + \frac{z'}{c}\right) - I_0\left(\frac{z'}{v^*}\right)\mathrm{e}^{-\left(t-\frac{z'}{v_f}\right)\Big/\tau_D}\right]u\left(t - \frac{z'}{v_f}\right) \tag{4}$$

The BG model is based on the idea that no propagation exists, thus it has no physical validity and can be seen as a special case of the TL model with *v* equal to infinity. In the model proposed by Heidler in [70], the current may be viewed as a downward propagating wave originating at the upward moving front. This model has some physical lacks related to the instantaneous charge absorbed into the return stroke front, but nevertheless, it produces reasonable fields for the first few microseconds. To overcome this problem the DU model has been proposed, where $v^* = cv_f / (c + v_f)$ and $\tau_d$ is a positive number.

The first term of the DU model is the TCS formula, while the other is an opposite polarity current which has the aim of eliminating any current discontinuity at the front by arising instantaneously to the value equal in magnitude to the current at the front and then decaying according to $\tau_d$.

In Figure 3, an illustration of the propagation of the current along the channel is sketched according to the three traveling current source models. It can be seen that, differently form the Transmission Line type models, a distortion in the current waveform appears in all the three Traveling Current Source models.

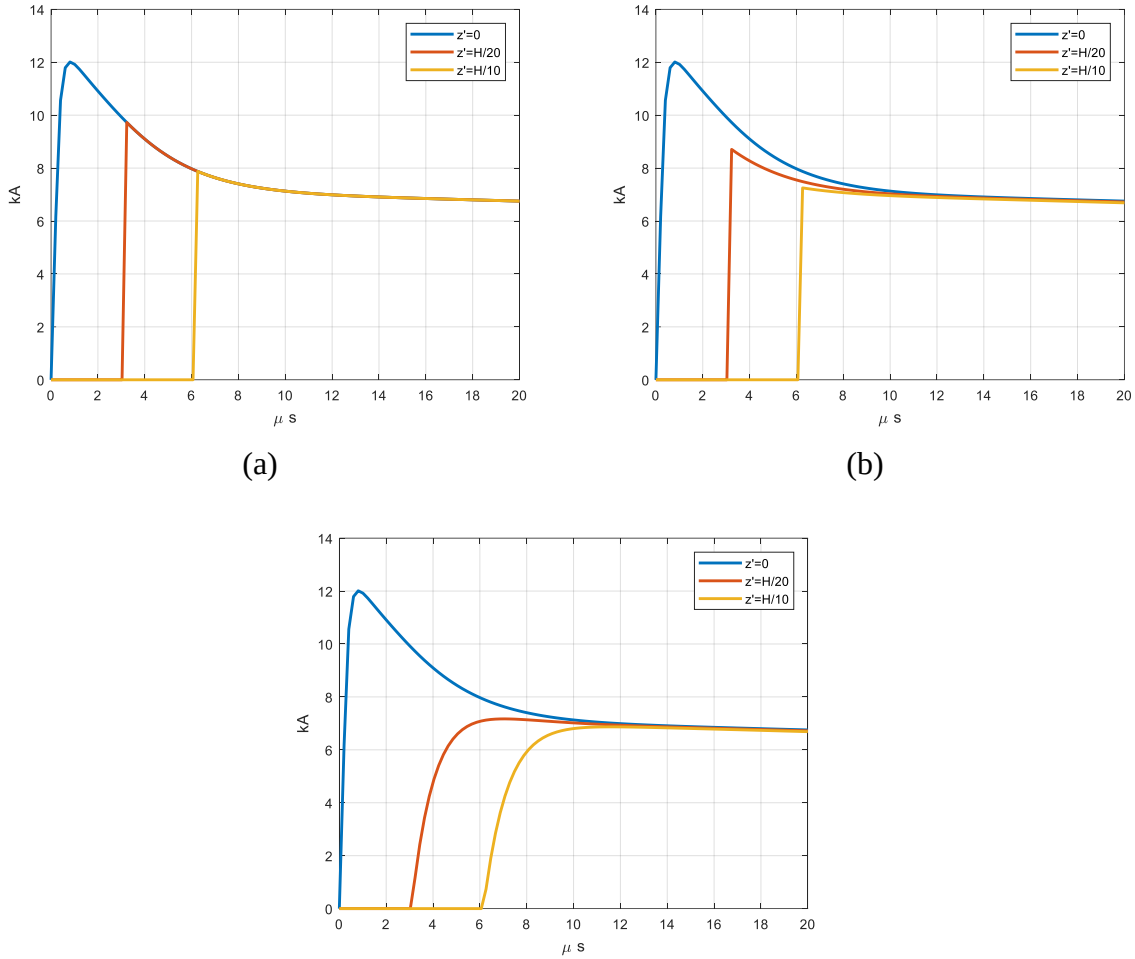


**Figure 3 propagation of the current along the channel according to the BG model (a), the TCS model (b) the DU model (c). Channel-base waveform adopted: Heidler's first stroke [15]**

### *2.1.1.3 The channel base current*

Both the Transmission Line and the Traveling Current Source models need as input the knowledge of the channel base current. The most widely adopted analytical expressions are:

- The double exponential waveform (DEXP) proposed by Golde in 1977

$$I_0(t) = I_m\left(e^{-\alpha t} - e^{-\beta t}\right) \tag{5}$$

where α and β are suitable constants, while $I_m$ is the normalization factor that can be adjusted in order to impose the current peak

- The well-known Heidler'waveform proposed in [15]

$$I_0(t) = \frac{I_S}{\eta} \frac{\left(\frac{t}{\tau_1}\right)^n}{1+\left(\frac{t}{\tau_1}\right)^n} e^{-\frac{t}{\tau_2}} \tag{6}$$

where $I_S$ is a constant affecting the peak value of the current, $\eta = \exp\left(-\frac{\tau_1}{\tau_2}\left(n\frac{\tau_2}{\tau_1}\right)^{\frac{1}{n}}\right)$ and $n$, $\tau_1$ and $\tau_2$ are constants whose values have to be adjusted to mimic measured channel base currents.

- The formula proposed by Javor in [17]

$$I_0(t) = \begin{cases} I_m \tau^a e^{a(1-\tau)} & 0 \le \tau \le 1 \\ I_m \sum_{i=1}^{n} c_i \tau^{b_i} e^{b_i(1-\tau)} & \tau > 1 \end{cases} \tag{7}$$

where $a$ is a coefficient that can be adjusted in order to represent the maximum steepness of the current, $\tau$ is defined as the ratio between $t$ and the time in which $I_0=I_m$ and $n,c_i,b_i$ are coefficients that tune the decaying part of the waveform.

- The formula proposed by Andreotti in [16]

$$I_0(t) = \begin{cases} I_m \left(\frac{t}{\tau_1}\right)^n e^{n\left(1-\frac{t}{\tau_1}\right)} & 0 \le \frac{t}{\tau_1} \le 1+\frac{a}{n} \\ I_m \left(\frac{n+a}{n}\right)^n e^{-\frac{an}{a+n}\frac{t}{\tau_1}} & \frac{t}{\tau_1} > 1+\frac{a}{n} \end{cases} \tag{8}$$

where $\tau_1$ is the time to peak value, $a = \frac{\tau_1}{\tau_2}$ and $\tau_2$ is a parameter which tunes the decay time and $n$ is the steepness factor

- The formula proposed by Andreotti in [72]

$$I_0(t) = I_m(a+1)\left[1-e^{\beta\frac{(t_0-t)}{a\tau_1}}\right] e^{\beta\left(1-\frac{t}{\tau_1}\right)} u(t-t_0) \tag{9}$$

where $\tau_1$ is the time to peak value, $t_0$ is an offset time, $\beta = \frac{\tau_1}{\tau_2}$ and $a$ is evaluated solving the following equation:

$$\left(1+\frac{1}{a}\right)^{a} = e^{\beta\left(1-\frac{t_0}{\tau_1}\right)} \tag{10}$$

### 2.1.2 Typical validation of the engineering models

The validation of engineering models can be obtained following two different approaches[2]. Both are based on the comparison between the calculated and measured electromagnetic fields, but they differ for the input data necessary for the electromagnetic fields calculation. In the first approach, the electromagnetic fields computation is evaluated through the engineering model considered where the channel base current waveform and the propagation speed are measured, while the second approach assumes a typical channel base current waveform and a typical propagation speed. If, from one side, the first approach has a stronger validity, on the other hand, it is feasible only in case of triggered lightning events, where the channel base current can be measured.

As can be expected, the "typical" validation has been more widely employed, leading to the following conclusions. According to [73], four main characteristics can be seen in the lightning electromagnetic fields:

- a sharp initial peak that varies approximately as the inverse distance beyond a kilometre or so in both electric and magnetic fields
- a slow ramp following the initial peak lasting less than 100 μs for electric fields measured within a few tens of kilometres
- a hump following the initial peak in magnetic fields within a few tens of kilometres
- a zero crossing within tens of milliseconds of the initial peak in both electric and magnetic field at 50 to 200 km

If the first feature is reproduced by all the described models, the second one is not captured by the TL. The hump in the magnetic field is not represented adequately by the MTLE which, on the other hand, provides reasonable zero crossing time (which is not the case for the BG, the TL and the TCS models). Moreover, according to [69], the new functions MTLTSIN, MTLTCOS, MTLT and MTLTS are able to reproduce all the desired features.

### 2.1.3 Engineering models effects on the induced voltages

This section is aimed at showing the induced voltage on a distribution line, whose details are given in Table 1. The induced voltages have been calculated with the ten engineering models presented in the previous section, using the coupling code developed in [34]. The return stroke

speed and the current wave propagation speed are $v = v_f = 1 \cdot 10^8 ms^{-1}$ [62], the channel height is 8 km, the decay factor λ is 2000 and $\tau_d$ is 1μs.

**Table 1 – Distribution line details**

| | |
|---|---|
| Length | 1200m |
| Number of conductors | 1 |
| Conductor height | 10 m |
| Conductor diameter | 1 cm |

Four different configurations for the selected distribution line have been taken into account (see Table 2). They differ from each other for the line terminations and the ground conductivity. In particular, in the Tests 3 and 4 a lossy ground with conductivity σ=0.01 S/m and ground relative permittivity $\varepsilon_r$=10 has been considered. According to Figure 4 the lightning stroke location is at distance *d*=100 m from the central point of the line. The calculation point is located at the central point of the line (*0, d, h*). The matching resistors value is 498 Ω.

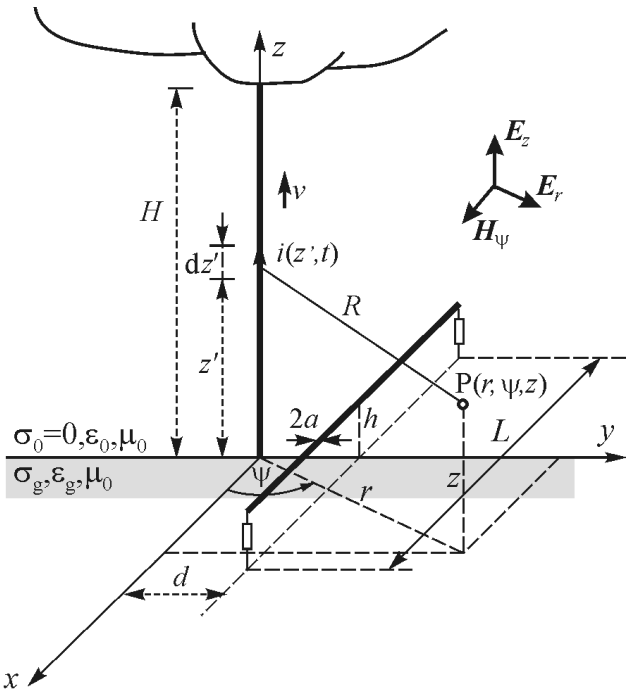


**Figure 4 Lightning return stroke channel nearby an overhead line**

**Table 2 – Test Details**

| Test | Ground | Terminations |
|---|---|---|
| 1 | Perfect | Matched/ Matched |
| 2 | Perfect | Matched/ Open |
| 3 | Lossy | Matched/ Matched |
| 4 | Lossy | Matched/ Open |

The induced voltages for cases 1-4 are presented in Figure 5-Figure 8.

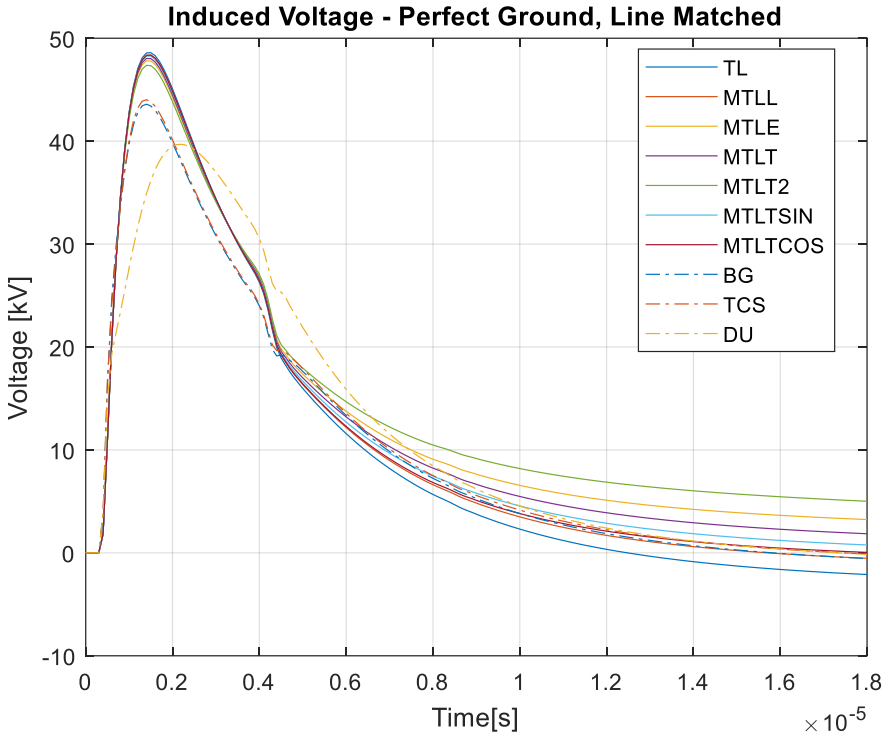


**Figure 5 Induced Voltages Test 1**

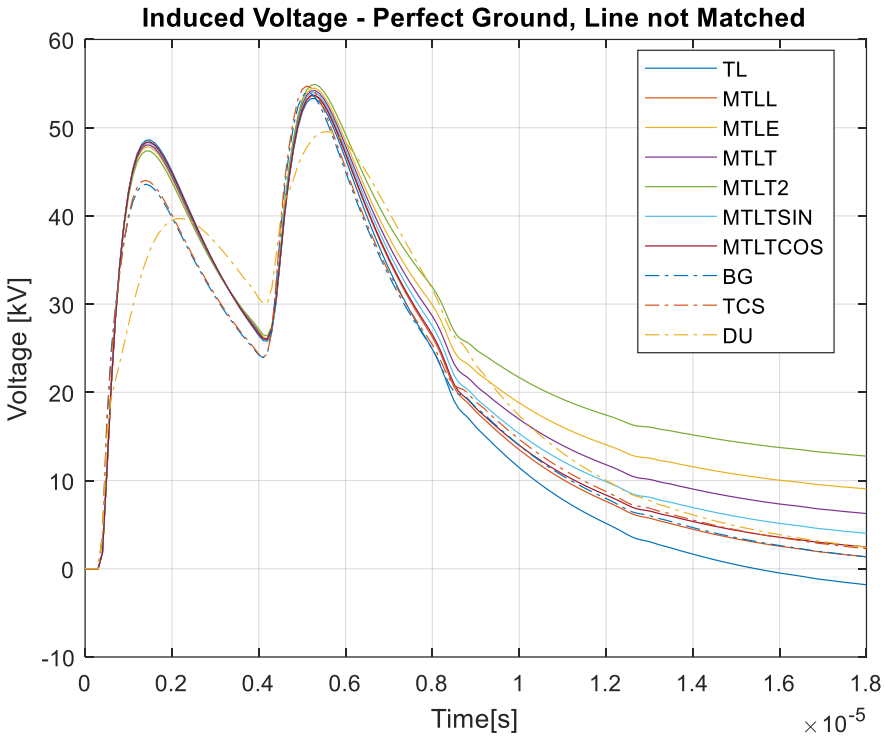


**Figure 6 Induced Voltages Test 2**

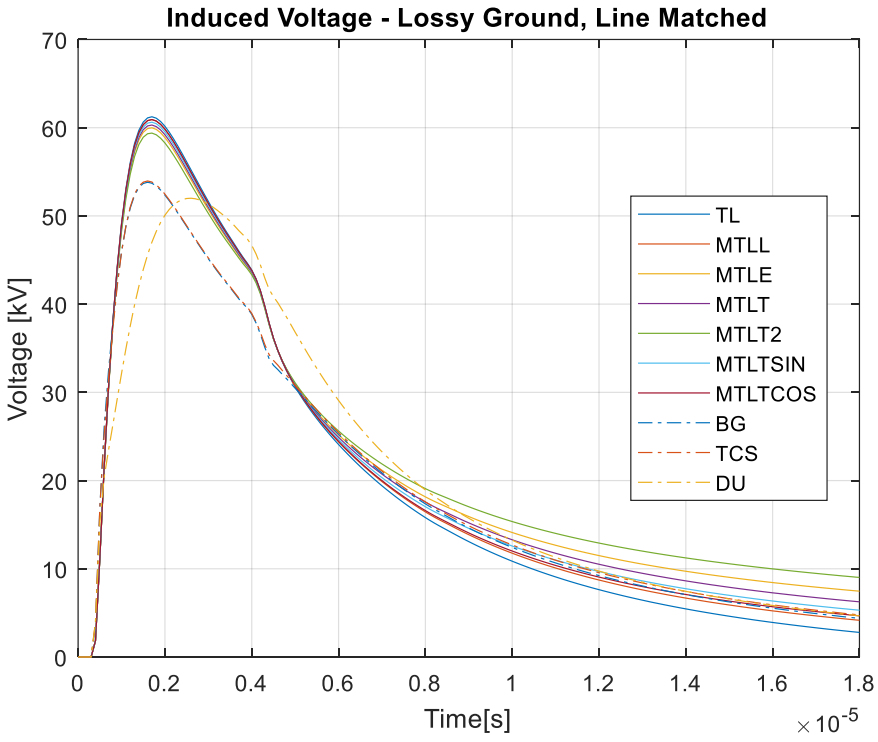


**Figure 7 Induced Voltages Test 3**

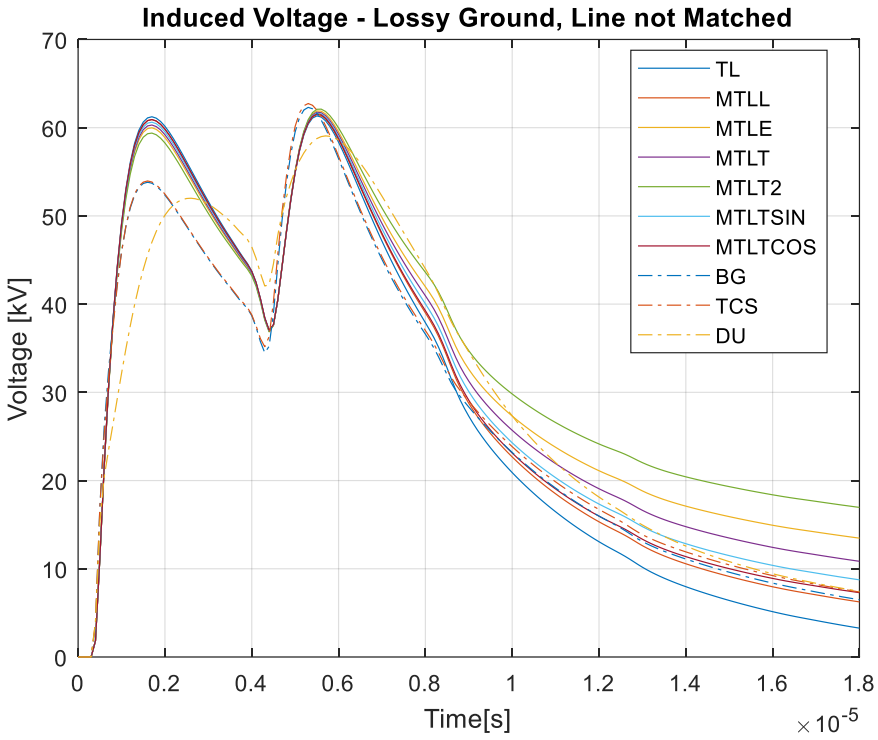


**Figure 8 Induced Voltages Test 4**

The comparison among the Transmission Line type models suggests that they all provide similar results for what concerns the rising part of the overvoltage and the peak value. Some differences appear in the tails and it can be observed that the higher the attenuation of the current (see Figure 1 and Figure 2) the slower the decrease of the overvoltage time profile.

Induced voltages predicted by the TCS and the DU models are characterized by faster rising and falling time than the Transmission Line type ones. A possible explanation is the following. While in the TL models the direction is upward and thus the current at a height $z'_1$ reaches its peak afterwards the peak occurrence at $z'_2 < z'_1$, in the TCS and DU models the direction is downward and thus the current at the height $z'_1$ reaches its peak before the one at $z'_2$. These considerations on the current propagation can be easily extended to the electric field because it is the result of the integration of all the fields produced by different current dipoles placed along the channel. Consequently, the TCS and DU models produce fields that have faster rise time and thus also the overvoltage waveform is faster than the other ones.

Tests 2 and 4 present the effect of the line termination opening. In each case, the waveform presents two voltage peaks according to the reflection phenomenon occurring at $t=1200/(3*10^8)=4$ μs after the starting of the overvoltage wave in the central point of the line.

The effect of the finite ground conductivity can be appreciated comparing Test 1 with 3 and Test 2 with 4. As outlined in [74] the lossy ground influences more the (radial) field calculation

than the coupling process, even though a term containing the finite ground conductivity appears both in the fields formulas and in the coupling equations. Anyway, the final result is an enhancement of the overvoltage peak in accordance to what concluded in [75] (see Figure 7 and Figure 8), where the voltage increases with respect to the perfectly conducting ground cases).

## 2.2 The electromagnetic fields

The aim of this chapter is to calculate the lightning electromagnetic fields starting from the return stroke current (Section 2.1).

In several studies the ground is assumed to be a perfect conductor, even if the ground conductivity is very important for both irradiated electromagnetic fields and determination of parameters. Unfortunately, the electromagnetic fields depend on the ground conductivity, but the exact evaluation of such field implies the evaluation of the slowly converging Sommerfeld integrals [76] that do not present an explicit expression in the time domain. In order to overcome this difficulty, simplified models are generally used [25, 26, 60, 76-78].

In this framework, the approach proposed in this chapter is to:

1) present the complete field problem
2) present and solve a simplified problem that will be useful to solve the original one
3) solve the problem for the case of perfectly conducting ground and present the most commonly used approximate expression to deal with ground finite conductivity (i.e. the Cooray-Rubinstein formula)

### 2.2.1 Formulation of the complete field problem

Let us consider the situation depicted in Figure 9, where a vertical dipole taking a current *I* lays at a height *z'* over a conducting ground.

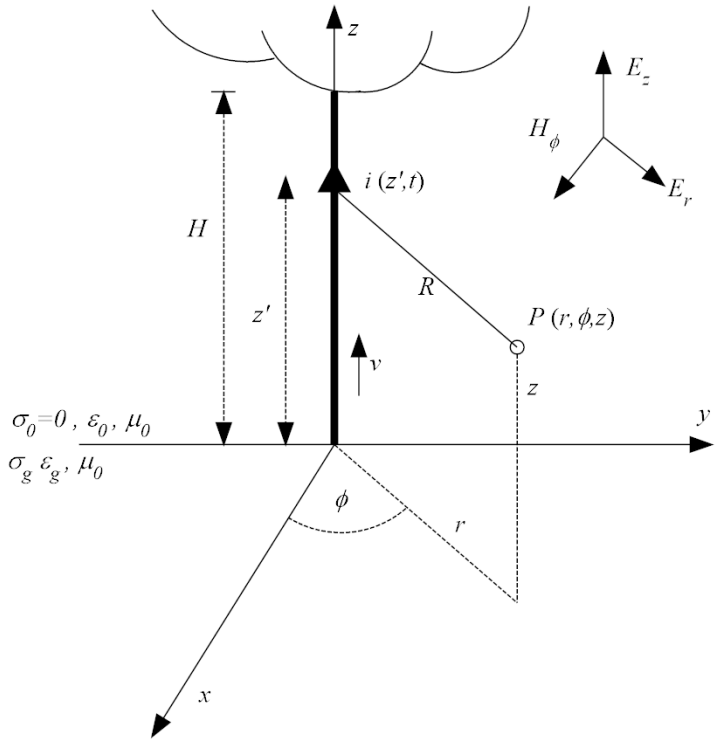


**Figure 9 Geometry of the problem**

The Maxwell's equations in the time domain can describe the electromagnetic fields at point *P* in an open space:

$$\nabla\times\vec{E}=-\frac{\partial\vec{B}}{\partial t};\quad \nabla\times\vec{H}=\vec{J}+\sigma\vec{E}+\varepsilon\frac{\partial\vec{E}}{\partial t};$$
$$\nabla\cdot\vec{D}=\rho;\qquad \nabla\cdot\vec{B}=0 \tag{11}$$

Where: $\vec{E}$ is the electric field, $\vec{D}$ the electric induction, $\vec{H}$ the magnetic field, $\vec{B}$ the magnetic induction, $\nabla\times\vec{F}$ the rotor of a generic field $\vec{F}$ , $\nabla\cdot\vec{F}$ its divergence , and $\nabla\vec{F}$ its gradient.

$\vec{E}$ and $\vec{D}$ , $\vec{B}$ and $\vec{H}$ are linked by the constitutive equations:

$$\vec{D}=\varepsilon\vec{E}$$
$$\vec{B}=\mu\vec{H} \tag{12}$$

$\mu$ being the magnetic permeability and $\varepsilon$ the electric permittivity.

In the vacuum, one has:

$$\mu = \mu_0 = 4\pi \times 10^{-7} \frac{H}{m}$$
$$\varepsilon = \varepsilon_0 = 8.852 \times 10^{-12} \frac{F}{m} \tag{13}$$

In the frequency domain, the expressions of fields have been derived assuming for all variables a time-harmonic dependence of the kind $e^{-j\omega t}$:

$$\nabla \times \vec{E} = j\omega \vec{B} = j\omega\mu \vec{H} \tag{14}$$

$$\nabla \times \vec{H} = \vec{J} + \sigma \vec{E} - \varepsilon\, j\omega \vec{E} \tag{15}$$

$$\nabla \cdot \vec{D} = \rho; \quad \nabla \cdot \vec{B} = 0 \tag{16}$$

$$\nabla \cdot \vec{E} = \frac{\rho}{\varepsilon}; \quad \nabla \cdot \vec{H} = 0 \tag{17}$$

As can be seen from (11) the main sources of $\vec{H}$ and $\vec{E}$ are respectively the density current $\vec{J}\left[\frac{A}{m^2}\right]$ and the charge density $\rho\left[\frac{C}{m^3}\right]$.

$\vec{J}$ and $\rho$ are related by the following formula, called continuity equation:

$$\nabla \cdot \vec{J} = -j\omega\rho \tag{18}$$

Introducing the potential vector $\vec{A}$ such that $\vec{H} = \frac{1}{\mu}\nabla \times \vec{A}$, (11) becomes:

$$\nabla \times \vec{E} - j\omega \nabla \times \vec{A} = 0 \rightarrow \quad \nabla \times \left(\vec{E} - j\omega \vec{A}\right) = 0 \tag{19}$$

As one can see, the field $\vec{E} - j\omega\vec{A}$ is irrotational and so the scalar potential $\phi$ can be defined as:

$$\vec{E} - j\omega\vec{A} = -\nabla\varphi \tag{20}$$

so, the fields can be expressed as a function of the scalar and vector potential, as follows:

$$\vec{E} = -\nabla\varphi + j\omega\vec{A}; \quad \vec{H} = \frac{1}{\mu}\nabla \times \vec{A} \tag{21}$$

So, the field problem is solved whenever one is able to determine $\phi$ and $\vec{A}$, which can be done as follows:

$$\nabla \times \vec{H} = \frac{1}{\mu}\nabla \times \left(\nabla \times \vec{A}\right) = \frac{1}{\mu}\left[\nabla\left(\nabla \cdot \vec{A}\right) - \Delta\vec{A}\right] \tag{22}$$

$$\nabla\left(\nabla\cdot\vec{A}\right)-\Delta\vec{A}=\mu\nabla\times\vec{H}=\mu\vec{J}+\mu\sigma\vec{E}-\mu\varepsilon\, j\omega\vec{E} \tag{23}$$

$$\nabla\left(\nabla\cdot\vec{A}\right)-\Delta\vec{A}=\mu\vec{J}+\mu\left(\sigma-j\omega\varepsilon\right)\vec{E}=\mu\vec{J}+\mu\left(\sigma-j\omega\varepsilon\right)\left(-\nabla\varphi+j\omega\vec{A}\right) \tag{24}$$

$$\nabla\left(\nabla\cdot\vec{A}\right)-\Delta\vec{A}-\mu\left(\sigma-j\omega\varepsilon\right)j\omega\vec{A}=\mu\vec{J}-\mu\left(\sigma-j\omega\varepsilon\right)\nabla\varphi \tag{25}$$

Imposing the Lorentz Gauge Condition stating that:

$$\nabla\cdot\vec{A}=-\mu\left(\sigma-j\omega\varepsilon\right)\varphi \tag{26}$$

one has that:

$$\Delta\vec{A}+\left(\omega^2\varepsilon\mu+j\omega\mu\sigma\right)\vec{A}=-\mu\vec{J} \tag{27}$$

Now, as the geometry depicted in Figure 9 presents two half spaces (air and ground), two cases have to be separately analyzed:

**1)** For the air,

$$\sigma=0\ ,\ \varepsilon=\varepsilon_0\ \text{and}\ \mu=\mu_0\ \text{and}\ \vec{J}=\delta\left(r-r'\right)\vec{e_3}$$

δ being the Dirac operator and $\rho$ ($\rho$') the spherical coordinates radius of the observation point (source point). Consequently, (27) becomes:

$$\Delta\vec{A}+\omega^2\varepsilon_0\mu_0\vec{A}=-\mu_0\vec{J}=-\mu_0\delta\left(\rho-\rho'\right)\vec{e_3} \tag{28}$$

As the definition of the wave number in air is:

$$k=\omega\sqrt{\varepsilon_0\mu_0}=\frac{\omega}{c} \tag{29}$$

equation (28) becomes

$$\Delta\vec{A}+k^2\vec{A}=-\mu_0\delta\left(\rho-\rho'\right)\vec{e_3} \tag{30}$$

Once the vector potential is at disposal, the electric field can be calculated as follows:

$$\vec{E}=-\nabla\varphi+j\omega\vec{A}=\frac{\nabla\left(\nabla\cdot\vec{A}\right)}{u(\sigma-j\omega\varepsilon)}+j\omega\vec{A}=\frac{\nabla\left(\nabla\cdot\vec{A}\right)}{-j\omega\varepsilon_0\mu_0}+j\omega\vec{A}=\frac{\nabla\left(\nabla\cdot\vec{A}\right)+k^2\vec{A}}{-j\omega\varepsilon_0\mu_0} \tag{31}$$

As can be seen from Figure 9, the cylindrical symmetry allows to state that $\vec{A}=A(r,z)\vec{e}_z$, for this reason:

$$\nabla\cdot\vec{A}=\frac{\partial A}{\partial z} \tag{32}$$

Consequently,

$$\nabla\left(\nabla\cdot\vec{A}\right)=\frac{\partial A}{\partial r\partial z}\vec{e}_r+\frac{\partial^2 A}{\partial z^2}\vec{e}_z \tag{33}$$

which allows to split the electric field in the two nonzero components $E_z$ and $E_r$:

$$E_z=\left(\frac{\partial^2 A}{\partial z^2}+k^2 A\right)\frac{1}{-j\omega\varepsilon_0\mu_0} \tag{34}$$

$$E_r=\frac{1}{-j\omega\varepsilon_0\mu_0}\frac{\partial^2 A}{\partial r\partial z}=\frac{j}{\omega\varepsilon_0\mu_0}\frac{\partial^2 A}{\partial r\partial z}=\frac{j\omega}{k^2}\frac{\partial^2 A}{\partial r\partial z}a \tag{35}$$

while the only component of magnetic field is:

$$H_\phi=\frac{1}{\mu_0}\nabla\times\vec{A}=\frac{1}{\mu_0}\left(-\frac{\partial A}{\partial r}\right) \tag{36}$$

**2)** For the ground,

$$\sigma\neq 0\ ,\ \varepsilon=\varepsilon_r\varepsilon_0\ ,\ \mu=\mu_0 \text{ and } \vec{J}=0$$

$A_E$ represents the potential vector of the ground and with the same previous assumptions, the equation becomes:

$$\Delta\vec{A}_E+\left[\omega^2\varepsilon\mu_0+j\omega\mu_0\sigma\right]\vec{A}_E=0 \tag{37}$$

As the definition of the wave number in the ground is:

$$k_E^2=\omega^2\varepsilon\mu_0+j\omega\mu_0\sigma \tag{38}$$

and

$$n^2=\frac{k_E^2}{k^2}=\frac{\varepsilon}{\varepsilon_0}+\frac{j\omega\mu_0\sigma}{\omega^2\varepsilon_0\mu_0}=\varepsilon_r+\frac{j\sigma}{\omega\varepsilon_0} \tag{39}$$

Consequently (37) becomes:

$$\Delta\vec{A}_E+k_E^2\vec{A}_E=0 \tag{40}$$

while the electrical field becomes

$$\vec{E}=-\nabla\varphi+j\omega\vec{A}_E=\frac{\nabla\left(\nabla\cdot\vec{A}_E\right)}{\mu_0\left(\sigma-j\omega\varepsilon\right)}+j\omega\vec{A}_E=\frac{\nabla\left(\nabla\cdot\vec{A}_E\right)+\left(j\omega\mu_0\sigma+\omega^2\mu_0\varepsilon\right)\vec{A}_E}{\mu_0\left(\sigma-j\omega\varepsilon\right)}=$$
$$=\frac{\nabla\left(\nabla\cdot\vec{A}_E\right)+k_E\vec{A}_E}{\mu_0\left(\sigma-j\omega\varepsilon\right)} \tag{41}$$

whose components are:

$$E_z = \left[ \frac{\partial^2 A_E}{\partial z^2} + k_E^2 A_E \right] \frac{1}{\mu_0 (\sigma - j\omega\varepsilon)} \tag{42}$$

$$E_r = \frac{1}{\mu_0 (\sigma - j\omega\varepsilon)} \frac{\partial^2 A_E}{\partial r \partial z} = \frac{j\omega}{j\omega\mu_0\sigma + \omega^2\varepsilon\mu_0} \frac{\partial^2 A_E}{\partial r \partial z} = \frac{j\omega}{k_E^2} \frac{\partial^2 A_E}{\partial r \partial z} \tag{43}$$

while the only component of magnetic field is:

$$H_\phi = -\frac{1}{\mu_0} \frac{\partial A_E}{\partial r} \tag{44}$$

#### *2.2.1.1 Boundary conditions*

The boundary condition that guarantees the uniqueness of the problem solution was firstly found by Sommerfeld and is known as the Radiation Condition.

$$\lim_{r\to\infty} \sqrt{r} \left( \frac{\partial \mathrm{A}}{\partial r} - \dot{j}kA \right) = 0 \tag{45}$$

The physical meaning of (45) is that the vector potential wave must propagate from the source (the dipole) outwards.

#### *2.2.1.2 Interface conditions*

It is known that at the interface between two different media the tangential component of the electric and magnetic fields is continuous, so:

- the continuity of the tangential component of the magnetic field reads $H_\varphi = H_{\varphi E}$ for $z=0$

where:

$$H_{\phi E} = -\frac{1}{\mu_0} \frac{\partial A_E}{\partial r} \tag{46}$$

and

$$H_\phi = -\frac{1}{\mu_0} \frac{\partial A}{\partial r} \tag{47}$$

That leads to

$$-\frac{1}{\mu_0} \frac{\partial A_E}{\partial r} = -\frac{1}{\mu_0} \frac{\partial A}{\partial r} \tag{48}$$

that implies that, at the ground level, $A=A_E$ as the fields and the potential are null for $r \to \infty$.

- The continuity of the tangential component of the electric field reads $E_{rE} = E_r$ for $z=0$

where:

$$E_{rE} = \frac{1}{k_E^2}\frac{\partial \mathrm{A}_E}{\partial r \partial z} \tag{49}$$

and

$$E_r = \frac{1}{k^2}\frac{\partial \mathrm{A}}{\partial r \partial z} \tag{50}$$

that produces

$$\frac{1}{k_E^2}\frac{\partial \mathrm{A}_E}{\partial r \partial z} = \frac{1}{k^2}\frac{\partial \mathrm{A}}{\partial r \partial z} \tag{51}$$

In view of limit for $r \to \infty$, the following equation is obtained:

$$\frac{1}{k_E^2}\frac{\partial \mathrm{A}_E}{\partial z} = \frac{1}{k^2}\frac{\partial \mathrm{A}}{\partial z} \Rightarrow n^2\frac{\partial A}{\partial z} = \frac{\partial A_E}{\partial z} \tag{52}$$

Summarizing, the problem of Figure 9 is described by the following equations:

$$\begin{cases} \dfrac{1}{k_E^2}\dfrac{\partial \mathrm{A}_E}{\partial z} = \dfrac{1}{k^2}\dfrac{\partial \mathrm{A}}{\partial z} \Rightarrow n^2\dfrac{\partial A}{\partial z} = \dfrac{\partial A_E}{\partial z} & \text{for } z > 0,\ P(x,y,z) = \text{generic point of observation},\ P'(0,0,z') = \text{source point},\ \delta = \text{Dirac pulse} \\ \Delta\vec{\mathrm{A}}_E + k_E^2\vec{\mathrm{A}}_E = 0 & \text{for } z < 0 \\ \lim_{r\to\infty}\sqrt{r}\left(\dfrac{\partial \mathrm{A}}{\partial r} - jkA\right) = 0 & \text{Radiation Condition} \\ n^2\dfrac{\partial \mathrm{A}}{\partial z} = \dfrac{\partial \mathrm{A}_E}{\partial z} & \text{for } z = 0\ ; \text{ interface condition} \\ A = A_E & \text{for } z = 0;\ \text{interface condition} \end{cases} \tag{53}$$

being: ω = angular frequency, $k = \omega/c$ wave number in air, $k_E$ = wave number in the ground, $n$= refractive index of the ground, $k_E^2 = \varepsilon\mu_0\omega^2 + j\,\mu_0\sigma\omega$, $n^2 = k_E^2 / k^2$, $\sigma$ = ground conductivity, $\mu_0$ = magnetic permeability in the vacuum, $\varepsilon_0$ = permittivity in the vacuum, $\varepsilon$ = permittivity in the ground ($\varepsilon \approx 10\varepsilon_0$).

### 2.2.2 Solution of the simplified problem

Sommerfeld has shown that the solution of problem (53) can be faced starting with the solution of the following simplified problem, in which a vertical dipole lays in the free space (the dipole is placed in the origin of a system of spherical coordinates (ρ,θ,ϕ))

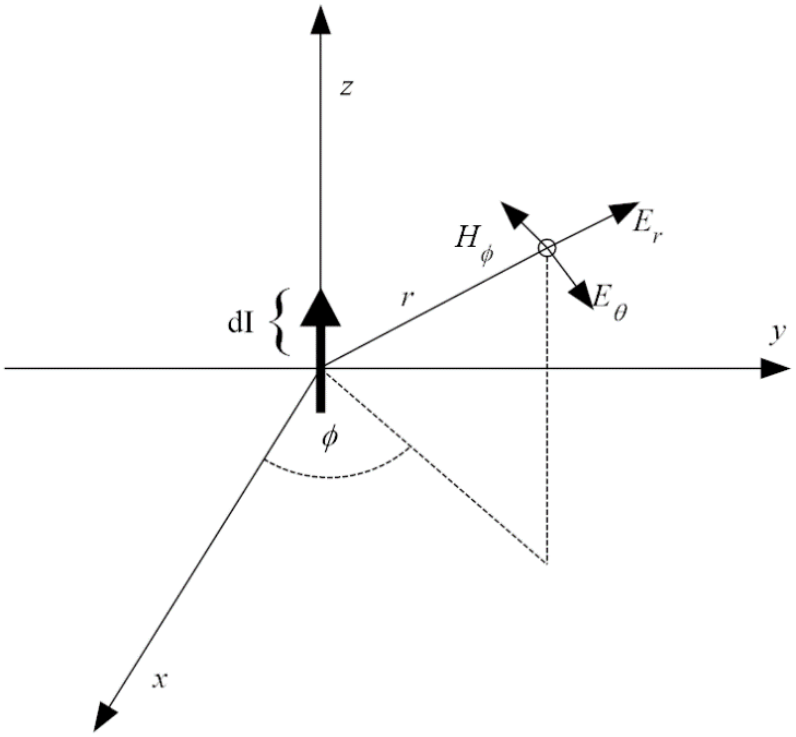


**Figure 10 Geometry of the simplified problem**

The equations that govern the problem are:

$$\begin{cases} \Delta^2 \mathrm{A} + k^2 A = -\mu_0 \delta(\rho) \\ \lim_{\rho \to \infty} \rho \cdot \left( \frac{\partial \mathrm{A}}{\partial \rho} - j\,kA \right) = 0 \end{cases} \tag{54}$$

It should be noted that the radiation condition assumes a different form, as it depends on the adopted coordinate system and that the relationship between spherical and cylindrical coordinates radii is given by $\rho = r^2 + (z - z')^2$.

For the symmetry of the problem, one can assume that the vector potential depends only on the radius, that is to say *A = A(ρ).* As a consequence, the first of (54) becomes:

$$\begin{aligned} &\frac{1}{\rho}\left( \frac{\partial^2 (A\rho)}{\partial \rho^2} \right) + k^2 A = 0 \\ &\rho \neq 0 \end{aligned} \tag{55}$$

The solution of (54) is:

$$A = \frac{C_1 e^{-jk\rho} + C_2 e^{jk\rho}}{\rho} \tag{56}$$

Imposing the radiation condition, one has that:

$$\lim_{\rho\to+\infty}\rho\cdot\left(\frac{\partial\left(\frac{1}{\rho}C_1e^{-jk\rho}+\frac{1}{\rho}C_2e^{jk\rho}\right)}{\partial\rho}-jk\left(\frac{1}{\rho}C_1e^{-jk\rho}+\frac{1}{\rho}C_2e^{jk\rho}\right)\right)=0$$

$$\lim_{\rho\to+\infty}\rho\cdot\left(-\frac{1}{\rho}C_1e^{-jk\rho}-\frac{1}{\rho}jkC_1e^{-jk\rho}-\frac{1}{\rho^2}C_2e^{jk\rho}+\frac{1}{\rho}jkC_2e^{jk\rho}-\frac{1}{\rho}jkC_1e^{-jk\rho}-\frac{1}{\rho}jkC_2e^{jk\rho}\right)=0$$

$$\lim_{\rho\to+\infty}\rho\cdot\left(-\frac{1}{\rho}C_1e^{-jk\rho}-\frac{2}{\rho}jkC_1e^{-jk\rho}-\frac{1}{\rho^2}C_2e^{jk\rho}\right)=0 \qquad (57)$$

That is satisfied if $C_1 = 0$. Then:

$$A=\frac{C_2}{\rho}e^{jk\rho} \qquad (58)$$

which claims for the evaluation of $C_2$. Integrating the first of (54) on a sphere with radius $a\to 0$ and centered in the origin, the right hand side is:

$$\int_s -\mu_0\delta(\rho)dV=-\mu_0 \qquad (59)$$

On the other hand, integrating the left-hand side, one has:

$$\int_s\left(\Delta A+k^2A\right)dV=\int_s\Delta AdV+\int_s k^2AdV \qquad (60)$$

Recalling (58), the second term in (60) becomes:

$$\int_s\left(k^2AdV=\int_s k^2\frac{C_2}{\rho}e^{jk\rho}\right)=\int_0^a\left(\int_0^{2\pi}\left(\int_0^{\pi}k^2\frac{C_2}{\rho}e^{jk\rho}\rho^2\sin\varphi d\varphi\right)d\vartheta\right)d\rho \qquad (61)$$

which approaches zero as a → 0.

As far as the first letter in (60) is considered, the following holds true:

$$\int_s (\Delta A_\rho) dV = \int_\vartheta \vec{\nabla} A_\rho \cdot \vec{n} d\vartheta = \int_0^{2\pi} \left( \int_0^{\pi} \frac{\partial A_\rho}{\partial \rho} a^2 \sin\varphi d\varphi \right) d\vartheta =$$

$$= \int_0^{2\pi} \left( \int_0^{\pi} \frac{\partial \left( \frac{C_2}{\rho} e^{jk\rho} \right)}{\partial \rho} a^2 \sin\varphi d\varphi \right) d\vartheta =$$

$$= C_2 \int_0^{2\pi} \left( \int_0^{\pi} \left( -\frac{e^{jka}}{a^2} + \frac{jk}{a} e^{jk\rho} \right) a^2 \sin\varphi d\varphi \right) d\vartheta =$$

$$= C_2 \left( \int_0^{2\pi} \left( \int_0^{\pi} -e^{jka} \sin\varphi d\varphi \right) d\vartheta \right) = \quad (62)$$

$$= C_2 \left( \int_0^{2\pi} -e^{jka} (\cos 0 - \cos\pi) d\vartheta \right) =$$

$$= C_2 \left( \int_0^{2\pi} -2e^{jka} d\vartheta \right) =$$

$$= -C_2 \left( 2\pi \cdot 2e^{jka} \right)$$

that allows to state:

$$4\pi C_2 e^{jka} = \mu_0 \quad (63)$$

Now, taking the limit for $a \to 0$ one has that $C_2 = \frac{\mu_0}{4\pi}$.

As a consequence, the final solution is:

$$A = \frac{\mu_0}{4\pi\rho} e^{jk\rho} \quad (64)$$

Sommerfeld showed that both (64) and the complete field problem solution can be written as a superposition of the eigenfunctions of the homogeneous Helmholtz problem; the only difference lays in the values of the linear combination coefficients. This is beyond the scope of this thesis; anyway, the solution of the simplified problem has been found because it can be easily used for the solution of the original field problem in the case of ideal ground. As well-known, when the ground is perfectly conducting, all the fields must be zero in the lower half space. Consequently, the interface conditions state that the tangential components of both electric and magnetic fields at ground level must be zero even in the upper half space. This suggests the possibility of adopting the image method and to replace the ground with another vertical dipole placed at a height *-z'* and taking the same current at the original one (Figure 11).

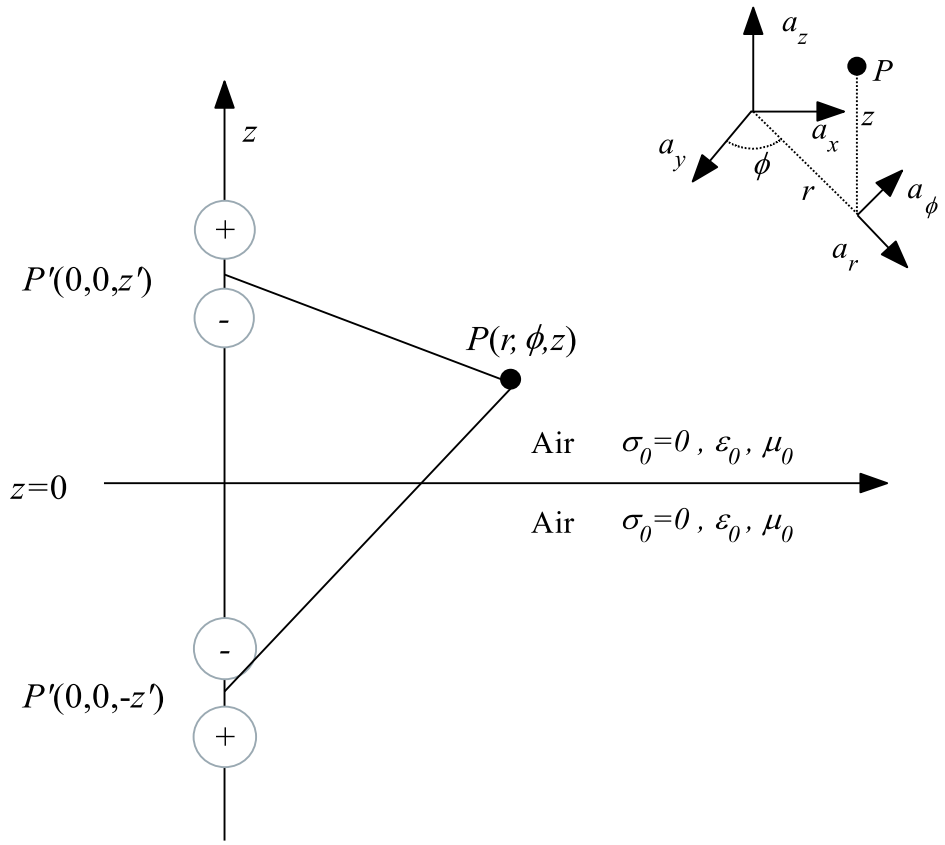


**Figure 11**

So, the solution of the complete problem for the case of ideal ground is given by:

$$A(r,z,z') = \frac{\mu_0}{4\pi}\left[\frac{e^{jk\sqrt{r^2+(z-z')^2}}}{\sqrt{r^2+(z-z')^2}} - \frac{e^{jk\sqrt{r^2+(z+z')^2}}}{\sqrt{r^2+(z+z')^2}}\right] \tag{65}$$

in which cylindrical coordinates have been adopted due to the different symmetry of the system.

### 2.2.3 The electromagnetic fields radiated by the lightning current in presence of an ideal ground

Since in all the typical return stroke models the lightning discharge channel is considered as a vertical antenna, it can be modeled as the sum of infinitesimal dipoles as illustrated in Figure 11, where the air is the half-space $z > 0$ and is characterized by $\varepsilon_0$, $\mu_0$, $\sigma = 0$ and the perfectly conducting ground is the other half-space, described by $\varepsilon_0$, and $\mu_0$.

Introducing a system of cylindrical coordinates ($r$, $\varphi$, $z$), the vector potential can be expressed integrating (65) along the channel, that is to say:

$$A(r,z)=\frac{\mu_0}{4\pi}\int_0^H\left[\frac{e^{jk\sqrt{r^2+(z-z')^2}}}{\sqrt{r^2+(z-z')^2}}-\frac{e^{jk\sqrt{r^2+(z+z')^2}}}{\sqrt{r^2+(z+z')^2}}\right]I\left(z',\omega\right)dz'=$$
$$=\frac{\mu_0}{4\pi}\int_{-H}^{H}\frac{e^{jk\sqrt{r^2+(z-z')^2}}}{\sqrt{r^2+(z-z')^2}}I\left(\left|z'\right|,\omega\right)dz' \tag{66}$$

and the current flowing in the lightning channel (and in its image), in the frequency domain, is given by the Fourier transform of (1), that is to say:

$$I\left(\left|z'\right|,\omega\right)=I\left(0,\omega\right)P\left(\left|z'\right|\right)e^{j\omega\frac{|z'|}{v}} \tag{67}$$

recalling now (34)-(36), one can finally evaluate the lightning electromagnetic fields, as follows:

$$\begin{cases}E_z=\dfrac{j\omega}{k^2}\left(\dfrac{\partial^2A}{\partial z^2}+k^2A\right)\\[2ex] E_r=\dfrac{j\omega}{k^2}\dfrac{\partial^2A}{\partial r\partial z}\\[2ex] H_\phi=-\dfrac{1}{\mu_0}\dfrac{\partial A}{\partial r}\end{cases} \tag{68}$$

Inserting (66) into (68), one has:

$$\begin{cases}\mathrm{E_z}=\dfrac{\mathrm{I}(0,\omega)}{4\pi\varepsilon_0}\displaystyle\int_{-\mathrm{H}}^{\mathrm{H}}\left[\frac{2(\mathrm{z}-\mathrm{z}')^2-\mathrm{r}^2}{\mathrm{cR}^4}+\frac{2(\mathrm{z}-\mathrm{z}')^2-\mathrm{r}^2}{-\mathrm{j}\omega\mathrm{R}^5}+\mathrm{j}\omega\frac{\mathrm{r}^2}{\mathrm{c}^2\mathrm{R}^3}\right]\cdot\mathrm{e}^{\mathrm{j}\omega\left(\frac{\mathrm{R}}{\mathrm{c}}+\frac{|\mathrm{z}'|}{\mathrm{v}}\right)}\mathrm{P}(\mathrm{z}')\mathrm{dz}'\\[2ex] \mathrm{E_r}=\dfrac{\mathrm{I}(0,\omega)}{4\pi\varepsilon_0}\displaystyle\int_{-\mathrm{H}}^{\mathrm{H}}\left[\frac{3\mathrm{r}(\mathrm{z}-\mathrm{z}')}{\mathrm{cR}^4}+\frac{3\mathrm{r}(\mathrm{z}-\mathrm{z}')}{-\mathrm{j}\omega\mathrm{R}^5}+\mathrm{j}\omega\frac{\mathrm{r}(\mathrm{z}-\mathrm{z}')}{\mathrm{cR}^3}\right]\cdot\mathrm{e}^{\mathrm{j}\omega\left(\frac{\mathrm{R}}{\mathrm{c}}+\frac{|\mathrm{z}'|}{\mathrm{v}}\right)}\mathrm{P}(\mathrm{z}')\mathrm{dz}'\\[2ex] \mathrm{H_\phi}=\dfrac{\mathrm{I}(0,\omega)}{4\pi}\displaystyle\int_{-\mathrm{H}}^{\mathrm{H}}\left[\frac{\mathrm{r}}{\mathrm{R}^3}-\mathrm{j}\omega\frac{\mathrm{r}}{\mathrm{cR}^2}\right]\mathrm{e}^{\mathrm{j}\omega\left(\frac{\mathrm{R}}{\mathrm{c}}+\frac{|\mathrm{z}'|}{\mathrm{v}}\right)}\mathrm{P}(\mathrm{z}')\mathrm{dz}'\end{cases}$$

(69)

The inverse Fourier transform of (69) can be performed analytically. The range of integration is (*–vt*, *vt*) instead of (*–H*, *H*), since the current *I*(z',*t*) is identically zero for *z'>vt*, thus obtaining:

$$E_z(t)=\frac{1}{4\pi\varepsilon_0}\int_{-vt}^{vt}\left[\frac{2(z-z')^2-r^2}{cR^4}I\left(0,t-\frac{R}{c}-\frac{|z'|}{v}\right)+\right.$$
$$\left.+\frac{2(z-z')^2-r^2}{R^5}\int_0^t I\left(0,s-\frac{R}{c}-\frac{|z'|}{v}\right)ds-\frac{r^2}{c^2R^3}\frac{\partial I\left(0,t-\frac{R}{c}-\frac{|z'|}{v}\right)}{\partial t}\right]P(z')dz' \quad (70)$$

$$E_r(t)=\frac{1}{4\pi\varepsilon_0}\int_{-vt}^{vt}\left[\frac{3r(z-z')}{cR^4}I\left(0,t-\frac{R}{c}-\frac{|z'|}{v}\right)+\frac{3r(z-z')}{R^5}\int_0^t I\left(0,s-\frac{R}{c}-\frac{|z'|}{v}\right)ds+\right.$$
$$\left.+\frac{r(z-z')}{c^2R^3}\frac{\partial I\left(0,t-\frac{R}{c}-\frac{|z'|}{v}\right)}{\partial t}\right]P(z')dz' \quad (71)$$

$$H_\phi(t)=\frac{1}{4\pi}\int_{-vt}^{vt}\left[\frac{r}{cR^2}\frac{\partial I\left(0,t-\frac{R}{c}-\frac{|z'|}{v}\right)}{\partial t}+\frac{r}{R^3}I\left(0,t-\frac{R}{c}-\frac{|z'|}{v}\right)\right]P(z')dz' \quad (72)$$

### *2.2.3.1 The lossy ground case*

In case of a lossy ground, $E_z$ and $H_\phi$ are not so much affected by the finite ground conductivity and so they can be well approximated by its ideal expressions (70) and (72). Unfortunately, $E_r$ can strongly depend on the ground conductivity, but the exact evaluation of such field implies the evaluation of the slowly converging Sommerfeld integrals that do not present an explicit expression in the time domain. In order to overcome this problem, some approximate approaches have been developed; among them the most effective one is the so-called Cooray-Rubinstein correction that has been proposed in the time domain. The time domain expression is represented below:

$$E_{rL}(z,r,t)=\int_0^t H_\phi\left(0,r,\frac{|z'|}{v}\right)\left[K\left(t-\frac{|z'|}{v}\right)-\sqrt{\frac{\mu_0}{\varepsilon}}\delta\left(t-\frac{|z'|}{v}\right)\right]dz'+E_r(z,r,t) \quad (73)$$

The first member of the R.H.S. is an empirical correction factor, where the integral kernel K is defined as:

$$K(t)=\frac{\sigma_g}{2\varepsilon_g}e^{\frac{\sigma_g}{2\varepsilon_g}t}\left[I_0\left(\frac{\sigma_g}{2\varepsilon_g}t\right)-I_1\left(\frac{\sigma_g}{2\varepsilon_g}t\right)\right] \tag{74}$$

$I_n$ being the modified Bessel function of first type and order $n$.

## 2.3 The field-to-line coupling problem

The aim of this chapter is i) to derive the exact equations that describe the problem of the field to line coupling starting from the Maxwell equations and ii) to introduce the approximations to this exact formulation that allow to obtain the classical TL approach. Such approach is used to describe the interaction between lightning electromagnetic fields and power transmission lines.

For the sake of simplicity, the equations will be derived for a case of a single conductor over a perfectly conducting ground. The case of a Multi-Conductor Transmission Line (MTL) system over a finitely conducting ground will be just indicated as a straightforward generalization of the first simple case.

Let us consider a finite line of length $2L$ and radius $a$ laying at a height $h$ over a perfectly conducting ground. The line is considered as a perfect conductor, while the upper half space (air) presents electrical conductivity equal to zero.

As shown in Section 2.2, the vector potential to the problem source (i.e. the current density can be evaluated from the solution of the following differential equation:

$$\left(\Delta\mathbf{A}+k^2\mathbf{A}\right)=-\mu_0\mathbf{J} \tag{75}$$

i.e.

$$\mathbf{A}=\frac{\mu_0}{4\pi}\iiint_V\frac{e^{jkR}}{R}\mathbf{J}dV \tag{76}$$

where the integration is carried out along the object carrying the current that generates the electromagnetic fields and is $R$ the distance between the generic point $P'$ belonging to $V$ and the observation point $P$.

The problem can be solved using the image method. The situation is equivalent to another one in which the ground is removed and another line is placed at a height equal to $-h$ parallel to the original one and taking a current opposite to the one flowing in the source.

As a consequence, indicating with $I$(x') the current flowing in the source at the point x', (76) becomes:

$$\mathbf{A}(x,y,z)=A(x,y,z)\mathbf{e}_x=\frac{\mu_0}{4\pi}\int_{-L}^{L}g(x-x',y,z)I(x')dx'\mathbf{e}_x \tag{77}$$

*g* having the following expression:

$$g\left(x-x',y,z\right)=\frac{e^{j\sqrt{\left(x-x'\right)^2+y^2+\left(z-h\right)^2}}}{\sqrt{\left(x-x'\right)^2+y^2+\left(z-h\right)^2}}-\frac{e^{j\sqrt{\left(x-x'\right)^2+y^2+\left(z+h\right)^2}}}{\sqrt{\left(x-x'\right)^2+y^2+\left(z+h\right)^2}} \tag{78}$$

When the line is illuminated by an incident electric field $\mathbf{E_{inc}}$, the induced currents and charges produce a scattered field $\mathbf{E_{sca}}$ so that the total tangential component of the electric field on the surface of the wire is zero, that is to say:

$$\left(\mathbf{E}_{inc}+\mathbf{E}_{sca}\right)_x=0 \tag{79}$$

Now recalling (31) one has that

$$\left(\mathbf{E}_{sca}\right)_x=\frac{-1}{j\omega\mu_0\varepsilon_0}\frac{\partial^2 A}{\partial x^2}+j\omega A \tag{80}$$

$A$ being:

$$A(x)=\frac{\mu_0}{4\pi}\int_{-L}^{L} g\left(x-x'\right)I\left(x'\right)dx' \tag{81}$$

With *g* expressed as:

$$g\left(x-x'\right)=\frac{e^{j\sqrt{\left(x-x'\right)^2+a^2}}}{\sqrt{\left(x-x'\right)^2+a^2}}-\frac{e^{j\sqrt{\left(x-x'\right)^2+\left(2h\right)^2}}}{\sqrt{\left(x-x'\right)^2+\left(2h\right)^2}} \tag{82}$$

It should be noted that, in order to avoid singularities in the Green function *g*, the so-called thin wire approximation has been done, which assumes the following. In the evaluation of the source contribution to the scattered electric field, the source point is assumed to be placed in the line axis, while the observation one is placed on the line surface so that the distance between them can never be zero.

As a consequence, (79) becomes:

$$\frac{\partial^2 A}{\partial x^2}+k^2A=\frac{jk^2}{\omega}\left(\mathbf{E}_{inc}\right)_x \tag{83}$$

that, combined with (81), gives origin to the integer-differential equation that links the incident field to the induced current.

$$\left(\frac{\partial^2}{\partial x^2}+k^2\right)\left(\int_{-L}^{L} g\left(x-x'\right)I\left(x'\right)dx'\right)=\frac{-jk^2 4\pi}{\mu_0\omega}\left(\mathbf{E}_{inc}\right)_x \tag{84}$$

A few comments on equation (81): the physical meaning of the formula implies that the vector potential at a certain point x depends not only on the current in the same point but also on the

current in any other point of the line. However, observing that the Green function is decreasing in amplitude, one can do the following two approximations [79, 80]:

1. the Green function becomes sufficiently small if its argument becomes greater than $2h$
2. the current does not vary significantly in the range $(0,2h)$, which is true if the line height $h$ is small with respect to the wavelength associated to the frequency of the incident field

such approximations allow to rewrite (81) as follows:

$$A(x)=\frac{\mu_0}{4\pi}\int_{-L}^{L} g(x-x')I(x')dx' \approx \frac{\mu_0}{4\pi}\int_{0}^{2h} g(x-x')I(x')dx' \approx \frac{\mu_0 I(x)}{4\pi}\int_{-\infty}^{\infty} g(x-x')dx' \tag{85}$$

The physical meaning of the approximation (85) is that the vector potential at the generic abscissa $x$ depends only on the current at the same abscissa and not on the whole distribution of the current in the line. The last integral in (85) can be solved analytically (at least for k=0) leading to the following approximate expression:

$$A(x) \approx LI(x) \tag{86}$$

Being:

$$L=\frac{\mu_0}{2\pi}\ln\left(\frac{2h}{a}\right) \tag{87}$$

Now, in the antenna theory, it is common to introduce the concept of the scattered voltage defined as:

$$V_s(x)=\phi(x,z=h) \tag{88}$$

So, the $x$-component of (20) becomes:

$$\frac{dV_s(x)}{dx}-j\omega LI(x)=\left(\mathbf{E}_{inc}\right)_x \tag{89}$$

while (26) reads:

$$L\frac{dI}{dx}-j\omega\mu_0\varepsilon_0 V_s(x)=0 \tag{90}$$

that can be rearranged as follows:

$$\frac{dI(x)}{dx}-j\omega CV_s(x)=0 \tag{91}$$

having posed

$$C = \frac{2\pi\varepsilon_0}{\ln\left(\frac{2h}{a}\right)} \tag{92}$$

The system (89)-(91) can be written also in time domain apply the inverse Fourier transform to all quantities, thus leading to:

$$\frac{\partial V_s(x,t)}{\partial x} + L\frac{\partial I(x,t)}{\partial t} = \left(\mathbf{E}_{inc}(x,t)\right)_x \tag{93}$$

and

$$\frac{\partial I(x,t)}{\partial x} + C\frac{\partial V_s(x,t)}{\partial t} = 0 \tag{94}$$

where, for the sake of simplicity, the time dependence has been explicitly indicated but no new symbols have been introduced to indicate time domain variables.

Equations (89) and (91) (and its time domain counterpart (93)-(94)) represent the classical Agrawal formulation of the transmission line theory for illuminated lines in the case of a single conductor [31]. Such formulation involves the scattered voltage and the line tangential component of the electric field.

Equivalent approaches have been developed that use the total voltage $V$, related to the scattered one by means of the following expression (here reported in the frequency domain, but easily extended to the time domain):

$$V(x) = V_s(x) + V_{inc}(x) = V_s(x) - \int_0^h E_{z,inc}(x,z)dz \tag{95}$$

having indicated with $E_{z,inc}$ the vertical component of the incident electric field.

In order to solve (89)-(91), it is necessary to introduce suitable boundary conditions expressing the link between voltage and current at the line extremities. If, for example, two linear networks (Thevenin equivalents $V_A$,$Z_A$ and $V_B$, $Z_B$) are connected at the line extremities, one has to pose:

$$\begin{cases} V(-L) = V_A - Z_A I(-L) \\ V(L) = V_B + Z_B I(L) \end{cases} \tag{96}$$

### 2.3.1 The Multi-Conductor Transmission Line (MTL) Case

Let us consider the situation depicted in Figure 12, in which an MTL is illuminated by an external field

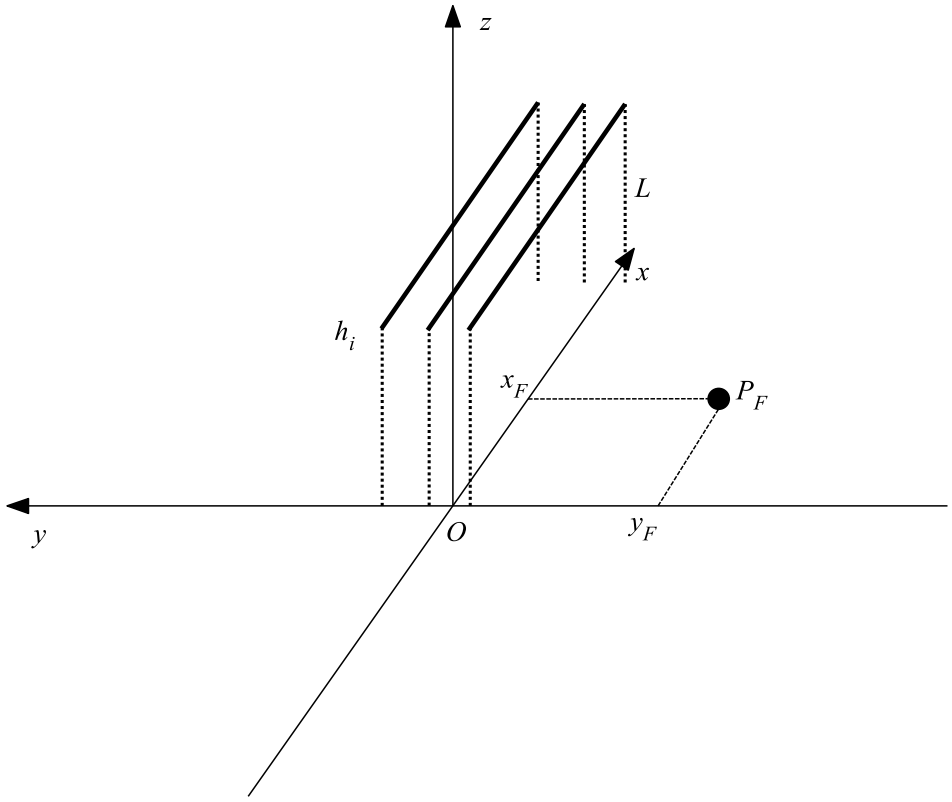


**Figure 12 MTL Geometry**

One can calculate the induced voltages and currents thanks to the well-known Agrawal model that is here written only in the time domain and suitably extended to take into account the presence of a finite conducting ground, that, in the time domain, basically consists of adding a current dependent voltage source $V_g$ in the first equation;

$$\begin{cases} \dfrac{\partial V_i^s}{\partial x}(x,t)+\sum_{j=1}^{M} L_{ij}\dfrac{\partial I_j}{\partial t}(x,t)+V_i^g(x,t)=E_{inc,x,i}(x,t) \\ \dfrac{\partial I_i}{\partial x}(x,t)+\sum_{j=1}^{M} C_{ij}\dfrac{\partial V_j^s}{\partial t}(x,t)=0 \end{cases} \tag{97}$$

where

$$V_i^g(x,t)=\int_0^t \xi_g^i(t-s)\frac{\partial I_i}{\partial s}(x,s)\,ds \tag{98}$$

Here $V_i^s(x,t)$ , $I_i(x,t)$ and $E_{inc,x,i}(x,t)$ denote the scattered voltage, the current and the tangential component of the exciting electric field on the $i^{th}$ conductor at distance $x$ from its left terminal and at time $t$, respectively. Moreover, $L_{ij}$ and $C_{ij}$ are the entries of the inductance and capacitance matrices [8] and $\xi_i^g$ is the time domain expression of the ground impedance [81]

$$\xi_i^g(t) = \frac{1}{4\pi}\min\left\{\sqrt{\frac{4\mu_0}{h_i^2\varepsilon_g}}, \frac{\mu_0}{\tau_i}\left[\sqrt{\frac{4\tau_{gi}}{\pi t}} + \mathrm{Erfcx}\left(\sqrt{\frac{\tau_{gi}}{t}}\right) - 1\right]\right\} \tag{99}$$

in which $\tau_i = \mu_0\sigma_g h_i^2$ and Erfcx is the scaled complementary error function. Finally, the total voltage $V_i$ can be obtained starting from the scattered one as follows:

$$V_i(x,t) = V_i^s(x,t) + V_{inc,i}(x,t) = V_i^s(x,t) - \int_0^{h_i} E_{inc,z,i}(x,z,t)dz \tag{100}$$

where $E_{inc,z,i}(x,z,t)$ is the vertical component of the exciting electric field calculated at time $t$, height $z$ from the ground and abscissa $x$. The vertical component of the exciting electric field being nearly invariant as a function of height above ground, it is useful consider the following acceptable approximation:

$$V_i(x,t) \approx V_i^s(x,t) - h_i E_{inc,z,i}(r_i(x),0,t) \tag{101}$$

### 2.3.2 The FDTD Code

The solution of (97) is typically achieved by mean of the finite-difference-time-domain (FDTD) technique [31]. In this chapter, a second-order scheme (the most used) is implemented following the results derived in [46] and [34]. To do this, (97) has to be discretized defining suitable samples both for time and space.

Once that the time step $\Delta t$ is chosen, one can define the following discrete sequence:

$$t_n = n\Delta t \tag{102}$$

The spatial step $\Delta x$ has to be chosen according to the well-known Courant stability condition, i.e.

$$c_0\Delta t \le C\Delta x \tag{103}$$

where $C$<1 being a suitable constant depending on the adopted discretization scheme. For the first-order FDTD scheme, $C$=1 and the choice of the equality in (103) originates the so-called magic step that produces no discretization error. In the following, a second order scheme will be chosen with $C$=0.3 In this way, one has that:

$$\Delta x = \frac{L}{K_m - 1}, \qquad K_m = \left[ \frac{LC}{c_0 \Delta t} \right] \tag{104}$$

[•] being the floor function. As a consequence, each line of the MTL will be sampled according to the following rule:

$$x_k = (k-1)\Delta x, \qquad k = 1...K_m \tag{105}$$

According to this discretization scheme and to the second order FDTD defined in [46] and [34], if one defines $V_{i,k}^{s,n} = V_i^s(x_k, t_n)$, $V_{i,k}^{g,n} = V_i^g(x_k, t_n)$, $I_{i,k}^n = I_i(x_k, t_n)$ and $E_{i,k}^{e,n} = E_{x,i}^e(x_k, t_n)$, the finite-difference solutions of (97) become

$$\begin{aligned}
V_{i,k}^{s,n+1} &= V_{i,k}^{s,n} - c_0^2 \sum_{j=1}^{M} L_{i,j} \frac{I_{j,k+1}^n - I_{j,k-1}^n}{2\Delta x} \Delta t + \\
&+ c_0^2 \left( \frac{V_{i,k+1}^{s,n} - 2V_{i,k}^{s,n} + V_{i,k-1}^{s,n}}{\Delta x^2} + \frac{V_{i,k+1}^{g,n} - V_{i,k-1}^{g,n}}{2\Delta x} - \frac{E_{i,k+1}^{e,n} - E_{i,k-1}^{e,n}}{2\Delta x} \right) \frac{\Delta t^2}{2} \\
I_{i,k}^{n+1} &= I_{i,k}^{s,n} - c_0^2 \sum_{j=1}^{M} C_{i,j} \left( \frac{V_{j,k+1}^{s,n} - V_{j,k-1}^{s,n}}{2\Delta x} + V_{i,k}^{g,n} - E_{j,k}^{h,n} + \right. \\
&\left. + \frac{V_{j,k}^{g,n} - V_{i,k}^{g,n-1}}{2} - \frac{E_{j,k}^{e,n} - E_{j,k}^{e,n-1}}{2x} \right) \Delta t + \\
&+ c_0^2 \left( \frac{I_{i,k+1}^n - 2I_{i,k}^n + I_{i,k-1}^n}{\Delta x^2} \right) \frac{\Delta t^2}{2}
\end{aligned} \tag{106}$$

Equation (106) allows us to evaluate the scattered voltage and current at the point $x_k$ and at the time step $t_{n+1}$ as a function of the same quantities at points $x_{k-1}$, $x_k$ and $x_{k+1}$ at time step $t_n$. Moreover, one has to know the tangential component of the electric field $E_x^e$ and the function $V_i^g$ at time steps $t_n$ and $t_{n-1}$ in the points $x_{k-1}$, $x_k$ and $x_{k+1}$.

It is apparent that (106) cannot be used for the two ends of each conductor, as one of the neighbor points does not exist; moreover, such points are not governed by the original differential equations as they are the ones in which the boundary conditions should be imposed. To cope with this, the currents in the first and in the last point can be updated by means of a linear extrapolation, as follows:

$$\begin{cases} I_{i,1}^{n+1} = 2I_{i,2}^{n+1} - I_{i,3}^{n+1} \\ I_{i,K_m}^{n+1} = 2I_{i,K_m-1}^{n+1} - I_{i,K_m-2}^{n+1} \end{cases} \tag{107}$$

Such currents represent the output of the FDTD scheme that are passed to the external circuit (it can be modelled in different software such as PSCAD, EMTP, Simulink) that models the

boundary conditions and produces the update of the voltages $V_{i,\mathrm{k}}^{ext,n+1}$ , according to the specific lumped parameters network that represents the power system one wants to analyze. In formulas, $\forall k \in \{1, K_m\}$

$$V_{i,k}^{s,n+1} = V_{i,k}^{\mathrm{ext},n+1} - V_{i,k}^{\mathrm{inc},n+1} \tag{108}$$

Moreover, each line can present many different points at which it is connected to the ground by means of suitable devices (e.g. arresters). In order to avoid to define one FDTD scheme for each portion, one can treat each of these discontinuity points in the same way as for the termination. In other words, if for any *d=1…D* one gives the abscissas $x_d$ of the *D* discontinuity points and defines the corresponding index $k_d = \left[\frac{x_d}{\Delta x}\right] + 1$ , it is possible to evaluate the left and right limits of the currents *x* approaching $x_d$ by means of a linear extrapolation. Then, the KCL allows us to find out the update of the current flowing in the devices connected to the line in the point $x_d$ that is to say

$$\begin{cases} I_{i,\mathrm{k}_d}^{d+,n+1} = 2I_{i,\mathrm{k}_{d+1}}^{n+1} - I_{i,\mathrm{k}_{d+2}}^{n+1} \\ I_{i,\mathrm{k}_d}^{d-,n+1} = 2I_{i,\mathrm{k}_{d+1}}^{n+1} - I_{i,\mathrm{k}_{d+2}}^{n+1} \\ I_{i,\mathrm{k}_d}^{d,n+1} = I_{i,\mathrm{k}_d}^{d-,n+1} - I_{i,\mathrm{k}_d}^{d+,n+1} \end{cases} \tag{109}$$

# 3 A new function for the channel base current

The aim of this chapter is to propose a new channel base current for lightning studies, able to represent the characteristics of the measured lightning strokes.

In literature, many models have been proposed that can be divided in two main categories:

1. Channel-base-current (CBC) functions made by a unique algebraic expression. Among them, the most well-known are the double-exponential (DEXP)[82], the Heidler function, [15] the pulse function [83] and a recent one proposed in [16].
2. CBC piecewise functions made by two or more parts. Among them the most popular ones are the functions proposed by Javor in [17] and Andreotti in [72].

The DEXP [82], the oldest one, presents a discontinuous time derivative at *t=0* and its tuning parameters are not decoupled, i.e. both of them act on the rising part and decay portion of the curve. Recently, the function proposed in [16] introduces a new CBC model, which better decouples the parameters affecting the rising part and the decay portion; however, this model shows three main drawbacks: *i*) the first-order derivative is still discontinuous in the origin, *ii*) some parameters have to be evaluated in a numerical way, *iii*) a procedure for the setting of the maximum steepness is not shown and *iv*) the peak value is slightly higher than the desired value.

Among the first group, the most-used and famous model is no-doubt the Heidler's function [15]. It can meet a high number of the aforementioned requirements and has a continuous first-order derivative, but, as pointed out in [17] and [72], it includes the calculation of the peak-correction factor from the expression involving other three parameters. Moreover, *i)* the parameters'choice (described in [84]) is not trivial as based on the solution of a numerical system and *ii)* the time integral solution requires the use of special functions [85].

The pulse function [83] has the same pros and cons of the Heidler's function, except for the possibility of calculating the time integral with an analytical formula. However, the parameters identification proposed in [83] is based on the minimization of a functional through the least squares fitting method. This aspect reduces the appeal of the approach especially when statistical studies require to change the current parameters at each lightning event simulation (see e.g. [1, 32, 34, 35]).

The CBC functions of the second group show an easier setting of the parameters and a continuous first-order derivative in the entire domain. In [17], Javor et al. represented the current with two functions: one before the time-to-peak and one after. With this approach, the authors proposed a detailed procedure to evaluate the functions parameters to reproduce the measured properties.

Even if each of these model has many advantages, there are some drawbacks. In the following the main drawbacks of each model are described in order to try to find a new model that overcome them.

The same approach has been faced by the authors of [72], using a piecewise function that changes its expression slightly later its time-to-peak value.

Unlike [83] the procedures to set the function parameters in [15, 17] and [72] do not need any optimization algorithm. Among the measured characteristics, one of the crucial properties is the maximum steepness. The authors of [86] show that the model proposed in [17] (and consequently also in [72]) cannot represent waveforms whose ratio between the maximum steepness and the mean steepness is lower than 1.7. According to Fig. 4 of [84], the limit value of the same quantity for the Heidler's formula is higher than 2.5.

A detailed comparison among the aforementioned models can be found in Table 3, focusing on the possibility of setting the measurements properties in analytical or numerical way as well as on the closed forms of the specific energy, time integral and Fourier Transform.

**Table 3 Comparison among the existing CBC functions (X-Opt: parameters obtained through optimization program)**

| Function | Continuous Derivative | Measurements that can be set | | | | | Specific Energy | Fourier Transform | Time Integral |
|---|---|---|---|---|---|---|---|---|---|
| | | Peak value | Time-to-peak | Maximum Steepness / Front duration | Time-to-half value | Total Charge | | | |
| DEXP [82] | | X | | | | | X | X | X |
| Heidler [15] | X | X | X - Numerical | X - Numerical with limit | | X - Numerical | | X | |
| Feizhou [83] | X | X – Opt. | X – Opt. | X – Opt. | | X – Opt. | | X | X |
| Andreotti [16] | | Slightly overestimated | X | | | X – Numerical | | X | X |
| Javor [17] | X | X | X | X – with limit | X | | | X – with the use of Gamma functions | X |
| Andreotti [72] | X | X | X | X – with limit | X | X – Numerical (alternative to time-to-half value) . | X | X | X |

This chapter aims at overcoming the actual limits of the proposed CBC functions, introducing a piecewise function made by three expressions. In particular, the new approach is able to: 1) reproduce analytically all the measured properties, 2) enlarge the range the ratio between the maximum steepness and the mean steepness can belong to ,3) provide closed-form expressions for the Fourier transform, time integral and specific energy, 4) have the continuity of the first-order time derivative in all its domain.

The chapter is organized as follows: Section 3.1 introduces the proposed function and provides the procedure for the analytical computation of the parameters, while Section 3.2 derives expressions for Fourier Transform, time integral and specific energy. Comparison of the proposed model with functions of Table 3 is shown in Section 3.3, while in Section 3.4 the parameters of the proposed function are given for different measured datasets.

## 3.1 Model definition

Let us consider the model proposed in the following equation

$$I_0(t) = \begin{cases} 0 & t < 0 \\ f_1(t) := k_1^n t^n & 0 \le t < t_1 \\ f_2(t) := k_2 e^{-a^2 (t_M - t)^2} + k_4 & t_1 \le t < t_M \\ f_3(t) := k_3 e^{-b^2 (t - t_M)^2} + k_5 & t \ge t_M \end{cases} \tag{110}$$

where, $t_M$ is the time-to-peak[1], $t_1$ is a time instant lower than $t_M$, $a, b > 0$, $k_1, k_2, k_3, k_4, k_5 \in \mathbb{R}$ and $n \in \mathbb{N}$. Let us now introduce $t_{50}$ as the time-to-half value and $\lambda$ as the maximum steepness. All the parameters involved in (110) are computed taking into account the following constraints:

1. $I_0$ is a continuous and differentiable function in $\mathbb{R}$
2. $I_0$ assumes the current-peak value $I_M$ at time $t_M$
3. $I_0$ assumes the maximum steepness $\lambda$ at time $t^* \in (t_1, t_M)$.
4. $\lim_{t \to +\infty} I_0(t) = I_{ref}$, where $I_{ref}$ is the steady-state value of the current (usually zero).
5. one of the following two conditions is satisfied
   i. $I_0(t_{50}) = \dfrac{I_M + I_{ref}}{2}$
   ii. $\int_0^{+\infty} I_0(t)\, dt = Q$, being $Q$ the total charge.

[1] Please note that $t_M$ can be usually obtained from the equivalent linear front duration ( $t_{d10/90}$ ) as proposed in [1]

To satisfy constraint 1 let us compute the derivative of $f_1$, $f_2$, $f_3$ as:

$$f_1'(t) = nk_1^n t^{n-1} \tag{111}$$

$$f_2'(t) = 2k_2 a^2 (t_M - t) e^{-a^2 (t_M - t)^2} \tag{112}$$

$$f_3'(t) = -2k_3 b^2 (t - t_M) e^{-b^2 (t - t_M)^2} \tag{113}$$

Proof of the continuity and derivability in $t = 0$ as well as the derivability in $t = t_M$ is trivial. The continuity and derivability in $t = t_1$ and the continuity in $t = t_M$ together with condition 2 lead to equations (114)-(116).

$$k_1^n t_1^n = k_2 e^{-a^2 (t_M - t_1)^2} + k_4 \tag{114}$$

$$nk_1^n t_1^{n-1} = 2k_2 a^2 (t_M - t_1) e^{-a^2 (t_M - t_1)^2} \tag{115}$$

$$k_2 + k_4 = k_3 + k_5 = I_M \tag{116}$$

In order to impose the maximum steepness, the maximum value of $f_2'$ is obtained studying the sign of $f_2''$:

$$f_2''(t) = 2k_2 a^2 \left[ -1 + 2a^2 (t_M - t)^2 \right] e^{-a^2 (t_M - t)^2} \tag{117}$$

It is possible to notice that $f_2''(t) > 0$ if and only if $-1 + 2a^2 (t_M - t)^2 \geq 0$, and consequently the maximum value of $f_2'$ is reached at time

$$t^* = t_M - \frac{1}{a\sqrt{2}} \tag{118}$$

The condition that $t^* > t_1$ implies that

$$a(t_M - t_1) > \frac{1}{\sqrt{2}} \tag{119}$$

and the constraint $I_0'(t^*) = \lambda$ becomes:

$$\sqrt{2} k_2 a e^{-1/2} = \lambda \tag{120}$$

Moreover, it is easy to observe that $\forall t \in [0, t_1]$

$$f_1'(t) \leq nk_1^n t_1^{n-1} = f_2'(t_1) \Rightarrow f_1'(t_1) < \lambda \tag{121}$$

Constraint 4 is satisfied if:

$$k_5 = I_{ref} \tag{122}$$

For what concerns the 5th condition, one can choose to give priority to the time-to-half value (5a) or to the total charge (5b)[2]. Condition 5a implies:

$$\left(I_M - I_{ref}\right)e^{-b^2(t_{50}-t_M)^2} + I_{ref} = \frac{I_M + I_{ref}}{2} \tag{123}$$

which can be analytically solved for the parameter *b*:

$$b = \frac{\sqrt{\ln 2}}{t_{50} - t_M} \tag{124}$$

while condition 5b can be solved analytically only if $I_{ref} = 0$ and implies:

$$\begin{aligned} Q &= \int_0^{t_1} f_1(t)dt + \int_{t_1}^{t_M} f_2(t)dt + \int_{t_M}^{+\infty} f_3(t)dt = \\ &= \frac{k_1^2 t_1^3}{3} + \frac{\sqrt{\pi}}{2a}\mathrm{Erf}(a(t_M - t_1)) + \frac{\sqrt{\pi}}{2b} \end{aligned} \tag{125}$$

where Erf is the usual Error Function. Eq. (125) can be analytically solved in *b*:

$$b = \frac{\sqrt{\pi}}{2}\left[Q - \frac{k_1^2 t_1^3}{3} - \frac{\sqrt{\pi}}{2a}\mathrm{Erf}(a(t_M - t_1))\right]^{-1} \tag{126}$$

Once $k_3$, $k_5$ and *b* are known, Equations (114)-(116) represent a linear system in the unknown parameters $k_1^n$, $k_2$ and $k_4$, whose solution is

$$\begin{aligned} k_2 &= \frac{nI_M}{(2a^2 t_1(t_M - t_1) - n)e^{-a^2(t_M - t_1)^2} + n} \\ k_4 &= I_M - k_2 \\ k_1^n &= k_2 \frac{a^2(t_M - t_1)e^{-a^2(t_M - t_1)^2}}{n t_1^{n-1}} \end{aligned} \tag{127}$$

It is important to notice that the third relation of (127) is solvable if the right hand side is positive; so $k_2$ must be positive, hence from the first of (127):

$$a^2 t_1\left(t_M - t_1\right) > \frac{n}{2}\left(1 - e^{a^2(t_M - t_1)^2}\right) \tag{128}$$

Eq. (128) is always verified because the left-hand side is always positive, while the right-hand one is always negative. Consequently, equations (127) lead always to acceptable values for any choice of the involved parameters. At this point, if one knows the values of *a* and $t_1$, (127)

[2] Both conditions cannot be satisfied contemporarily as, after having determined $k_3$ and $k_5$ only parameter *b* is actually available

allows to find the values of $k_1^n, k_2$ and $k_4$ to obtain the complete set of parameters in (110). Guidelines on the choice of *a* are provided in what follows.

Introducing

$$x := a\left(t_M - t_1\right) \tag{129}$$

one easily gets by (119) that $x > 1/\sqrt{2}$; then, substituting the first of (127) in (120), one has:

$$\frac{xe^{-1/2}\sqrt{2}}{t_1(ne^{-x^2} - n + 2x^2e^{-x^2}) - nt_M(e^{-x^2} - 1)} = \frac{\lambda}{nI_M} \tag{130}$$

Hence, for any assigned value $x_* > 1/\sqrt{2}$ equation (130) can be analytically solved with respect to $t_1$:

$$t_1 = \frac{\frac{nI_M}{\lambda}x_*\alpha + nt_M(e^{-x_*^2} - 1)}{ne^{-x_*^2} - n + 2x_*^2e^{-x_*^2}} \tag{131}$$

where $\alpha = e^{-1/2}\sqrt{2}$ . Then *a* can be found thanks to (129).

According to (110) it must be verified that $0 < t_1 < t_M$, which leads to the following condition on the ratio $K = \dfrac{\lambda}{I_M / t_M}$ between the maximum and the mean derivative:

$$f\left(x^*\right) := \frac{\alpha x_*}{1 - e^{-x_*^2}} < K < \frac{n\alpha}{2x_*e^{-x_*^2}} =: g\left(x^*\right) \tag{132}$$

Figure 13 shows the graph of *f* and g with *n=2.* A numerical approach permits to find that the minimum value assumed by *f* is 1.344 at $x_*^{\min} \approx 1.121$, while *g* is unbounded. Consequently, whatever value of the maximum steepness $\lambda$ greater than $1.344\dfrac{I_M}{t_M}$ verifies (132). Please note that 1.344 is lower than the boundary conditions obtained in [17, 84].

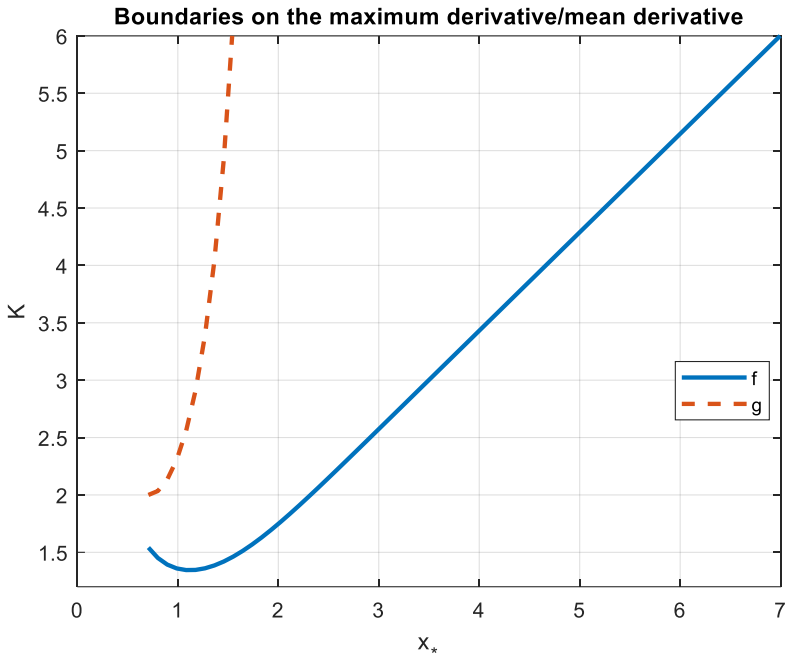


**Figure 13 Limits of the ratio between the maximum derivative and the mean derivative as a function of x**

In principle, there are infinite possibilities for the choice of $x_*$ here it will be chosen by solving

$$f\left(x_*\right)=K \tag{133}$$

Unfortunately (133) does not have analytical solution; so $f$ is here approximated with a piecewise linear function defined $\bar{f}$ as follows[3]:

$$\bar{f}\left(x\right)=\begin{cases} p_1 x+d_1 & x_*^{\min}<x\le\bar{x}_1 \\ p_2 x+d_2 & x_*^{\min}<x\le\bar{x}_2 \\ p_3 x+d_3 & x\ge\bar{x}_2 \end{cases} \tag{134}$$

where $\bar{x}_1$ solves $f\left(\bar{x}\right)=1.5$ while $\bar{x}_2$ solves $f\left(\bar{x}\right)=2$ and the parameters, obtained with a interpolation procedure, appear in Table 4. It is important to highlight that, as $f$ is only function of $x_*$, the interpolation procedure can be performed only once. Please note that due to the concavity of $f$ the interpolated curve $\bar{f}$ is always above $f$.

[3] The interpolated curve can be obtained as a generic piecewise linear function defined in $N$ parts. In this work $N$=3 is assumed, which leads to a very good approximation of $f$

**Table 4 Interpolation parameters of *f***

| Parameter | Value |
|---|---|
| $p_1$ | 0.2860 |
| $p_2$ | 0.7167 |
| $p_3$ | 0.8558 |
| $d_1$ | 1.0356 |
| $d_2$ | 0.3365 |
| $d_3$ | 0.0137 |
| $\bar{x}_1$ | 1.6233 |
| $\bar{x}_2$ | 2.3210 |

Consequently, $x_*$ can be evaluated as follows:

$$x^* = \begin{cases} \dfrac{K - d_1}{p_1} & 1.344 \le K < 1.5 \\ \dfrac{K - d_2}{p_2} & 1.5 \le K < 2 \\ \dfrac{K - d_3}{p_3} & K \ge 2 \end{cases} \tag{135}$$

As a conclusion of this section, let us summarize the steps that one has to follow in order to obtain the function parameters (supposing $K$>1.344)

1. Evaluate $x_*$ according to (135)
2. Choose $n$. Typical value can be $n=2$, but in principle any value of $n$ satisfies the requirements.
3. Evaluate $t_1$ according to (131)
4. Evaluate $a$ according to (129)
5. Evaluate $k_2$ according to the first of (127)
6. Evaluate $k_4$ according to the second of (127)
7. Evaluate $k_1^n$ according to the third of (127).
8. Evaluate $k_5$ according to (122)
9. Evaluate $k_3$ according to (116)
10. Evaluate $b$ according to
    a. (124), if the time-to-half value is considered
    b. (126),if the priority is given to the total charge

## 3.2 Time integral, Fourier transform and specific energy

### 3.2.1 Time Integral

The time-integral of the new function is trivial and involves the Erf function.

$$\int_0^t I_0(\tau)\,d\tau = \begin{cases} \phi_1(t) & 0 \le t \le t_1 \\ \phi_2(t) & t_1 < t \le t_M \\ \phi_3(t) & t > t_M \end{cases} \tag{136}$$

where

$$\begin{aligned} \phi_1(t) &= \frac{k_1^n t^{n+1}}{n+1} \\ \phi_2(t) &= \frac{k_1^n t_1^{n+1}}{n+1} + k_2 \frac{\sqrt{\pi}}{2a}\mathrm{Erf}\left(a(t_M - t_1)\right) - \\ &\quad + k_2 \frac{\sqrt{\pi}}{2a}\mathrm{Erf}\left(a(t_M - t)\right)t_1 + k_4(t - t_1) \\ \phi_3(t) &= \frac{k_1^n t_1^{n+1}}{n+1} + \frac{\sqrt{\pi}}{2a}k_2\mathrm{Erf}\left(a(t_M - t_1)\right) + k_4(t_M - t_1) \\ &\quad + \frac{\sqrt{\pi}}{2b}k_3\mathrm{Erf}\left(b(t - t_M)\right) + k_5(t - t_M) \end{aligned} \tag{137}$$

### 3.2.2 Fourier Transform

Similarly to the computation of the time integral, it is possible to obtain the Fourier Transform $\hat{I}_0(\omega)$, supposing $k_5$=0. More precisely if the functions $f_1$, $f_2$, $f_3$ introduced in Eq. (110) are extended to $\mathbb{R}$ as null function value, then:

$$\hat{I}_0(\omega) = \hat{f}_1(\omega) + \hat{f}_2(\omega) + \hat{f}_3(\omega) \tag{138}$$

$$\begin{aligned} \hat{f}_1(\omega) &= \frac{k_1^n e^{-\mathrm{j}\omega t}}{(-\mathrm{j}\omega)^{n+1}}\left(n!(-1)^n + \sum_{k=1}^{n}\frac{n!(-1)^{n-k}}{k!}(-\mathrm{j}\omega t)^k\right) + \\ &\quad - \frac{k_1^n e^{-\mathrm{j}\omega t}}{(-\mathrm{j}\omega)^{n+1}}n!(-1)^n \\ \hat{f}_2(\omega) &= \frac{k_2\sqrt{\pi}}{2b}e^{-\left(\frac{\omega^2}{4b^2} + j\omega t_M\right)}\left[1 - \mathrm{Erf}\left(\frac{j\omega}{2b}\right)\right] + \frac{k_4 j e^{-j\omega t_M}}{\omega} \\ \hat{f}_3(\omega) &= k_3\frac{\sqrt{\pi}}{2b}e^{-\left(\frac{\omega^2}{4b^2} + j\omega t_M\right)}\left[1 - \mathrm{Erf}\left(\frac{j\omega}{2b}\right)\right] \end{aligned} \tag{139}$$

### 3.2.3 Specific energy

The specific energy W/R represents the Joule losses per unit resistivity. It can be calculated as follows, where $k_5 = 0$, in order to have a convergence of the integral.

$$\frac{W}{R} = \int_0^{+\infty} I_0^2(t)\,dt = \int_0^{t_1} f_1^2(t)\,dt + \int_{t_1}^{t_M} f_2^2(t)\,dt + \int_{t_M}^{+\infty} f_3^2(t)\,dt \tag{140}$$

where

$$\begin{aligned}
&\int_0^{t_1} f_1^2(t)\,dt = \frac{k_1^{2n} t_1^{2n+1}}{2n+1} \\
&\int_{t_1}^{t_M} f_2^2(t)\,dt = \frac{k_4 k_2 \sqrt{\pi}}{a} \operatorname{Erf}\left(a\left(t_M - t_1\right)\right) + \\
&\qquad + \frac{\sqrt{2} k_2^2 \sqrt{\pi}}{4a} \operatorname{Erf}\left(\sqrt{2} a\left(t_M - t_1\right)\right) + k_4^2\left(t_M - t_1\right) \\
&\int_{t_M}^{+\infty} f_3^2(t)\,dt = \frac{k_3^2 \sqrt{2\pi}}{4b}
\end{aligned} \tag{141}$$

## 3.3 Comparison with the existing Channel-base functions

This section shows the comparison of the proposed model with other CBC functions. According to the considerations provided previously, the comparison will be made among the functions that are able to provide a continuous first-order derivative and whose parameters computation are not obtained through an optimization algorithm (as in [83]), i.e. the Heidler's function [15] and the functions proposed by Javor and Andreotti in [17, 72]. The comparison is obtained using the lightning parameters of the IEEE Standard [1], here provided in Table 5.

**Table 5 Median values of IEEE standard data**

| Parameter | Negative first | Negative subsequent |
|---|---|---|
| $I_M$ [kA] | 31.1 | 12.3 |
| $t_{d10/90}$ [μs] | 5.63 | 0.75 |
| $I'_{max}$ [kA/ μs] | 24.4 | 39.9 |
| $t_{50}$ [μs] | 77.5 | 30.2 |
| $Q$ [C] | 4.65 | 0.938 |

The new function is implemented following the approach provided in Section 3.1, using the time-to-half value criterion for tuning the decaying part and with $n=2$.

Figure 14-Figure 16 show the comparison of the negative first stroke in the rising part, decaying part and derivative. As can be noticed, Javor and Andreotti functions are similar in the rising part, while they have a different behavior in the decaying part. In this framework, as shown in Figure 16, each model is able to reproduce the maximum derivative provided in [1].

On the other hand, Figure 17-Figure 19 show the comparison of the negative subsequent stroke. In this case, the Heidler's function is not able to reproduce the maximum derivative as the numerical system of [84] has no solution . This behavior is due to the low ratio between the maximum derivative and the mean derivative: according to [1], such ratio is 2.43.

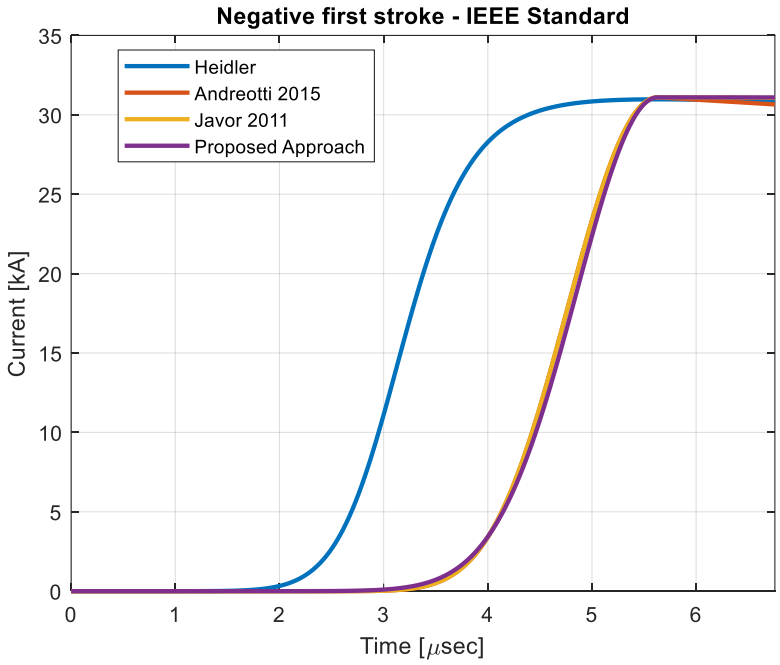


**Figure 14 Rising part of negative first stroke**

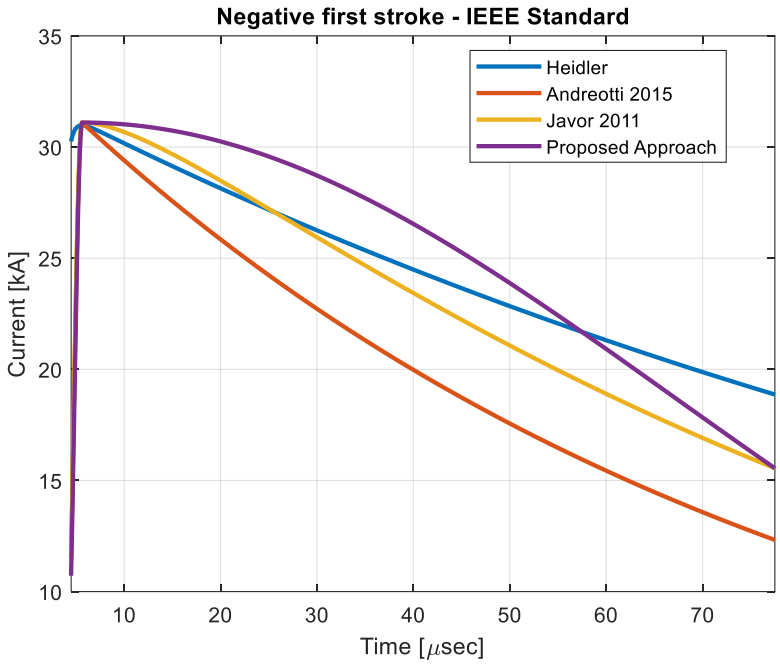


**Figure 15 Decaying part of negative first stroke**

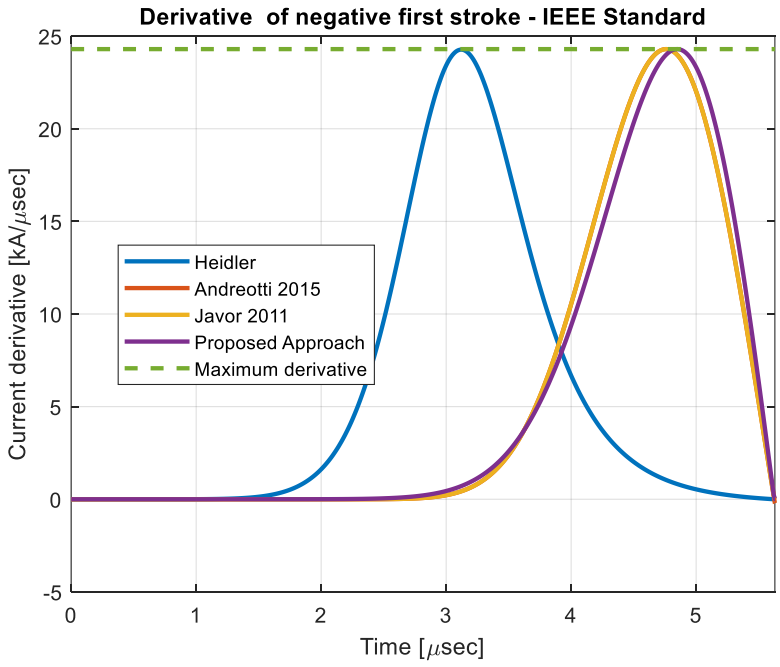


**Figure 16 Negative first stroke derivative**

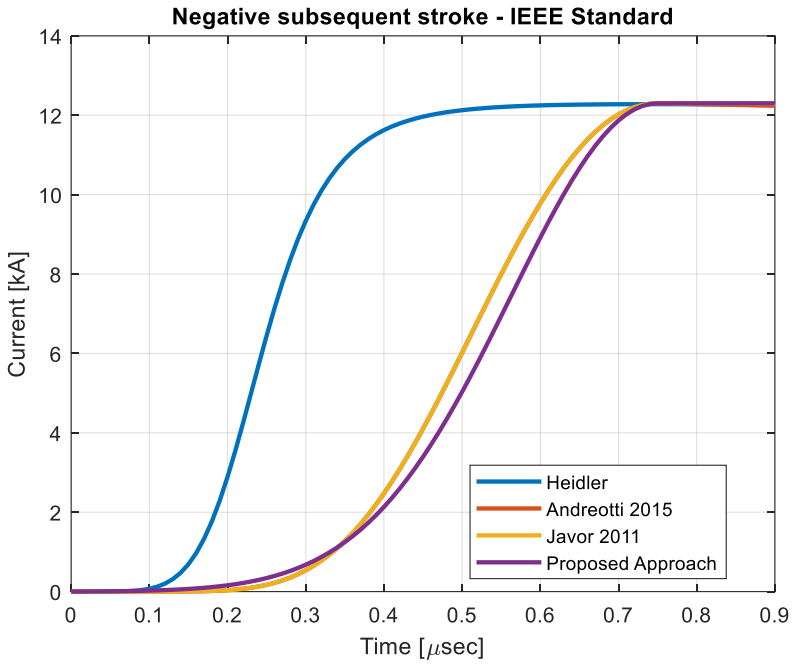


**Figure 17 Rising part of negative subsequent stroke**

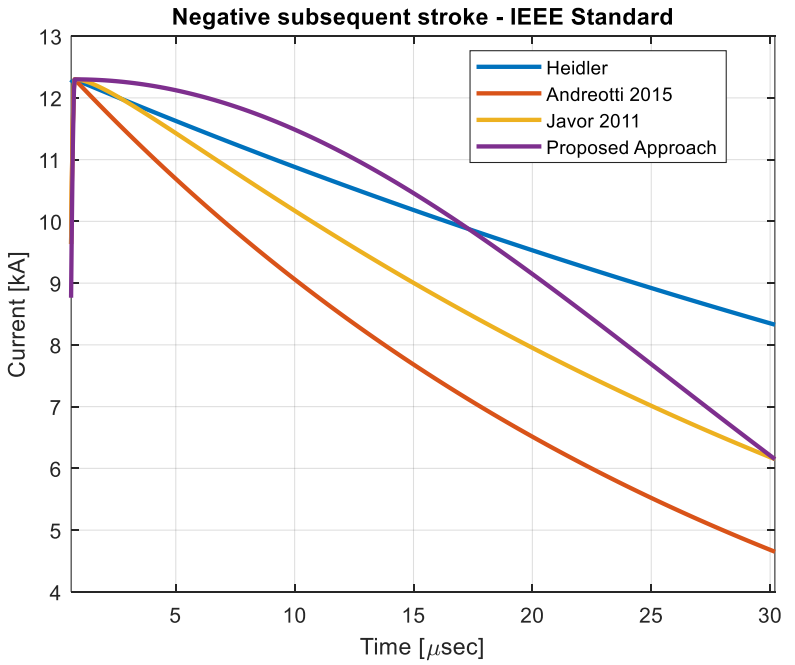


**Figure 18 Decaying part of negative subsequent stroke**

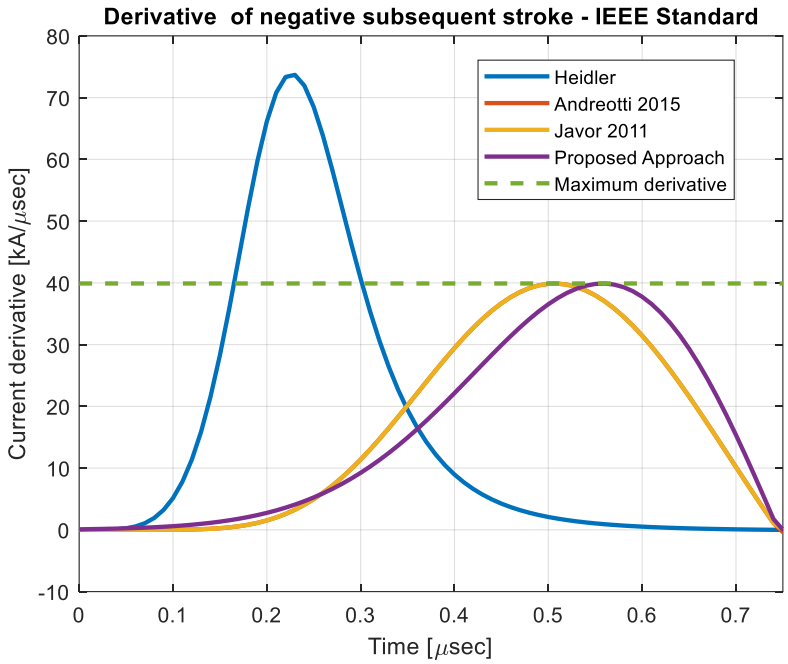


**Figure 19 Negative subsequent stroke derivative**

As mentioned before, one of the main advantages of the proposed CBC function is the possibility of representing waveforms characterized by a low value of the ratio between the maximum derivative and the mean derivative. Table 7 and Table 8 show the minimum value of $\lambda$ that can be reached according to different cases characterized by different values of front duration and peak current. In particular, the values corresponding to the $30^{th}$ , $50^{th}$ and $70^{th}$ percentile of the cumulative distribution of the front duration and peak current (provided in [1]) have been used and are here reported in Table 6.

**Table 6 Percentiles of the distributions of front duration and peak**

| | 30th percentile | 50th percentile | 70th percentile |
|---|---|---|---|
| Front duration – first stroke | 4.16 µs | 5.63 µs | 7.61 µs |
| Front duration – subsequent stroke | 0.46 µs | 0.75 µs | 1.21 µs |
| Peak current – first stroke | 24.12 kA | 31.1 kA | 40.08 kA |
| Peak current- subsequent stroke | 9.32 kA | 12.3 kA | 16.24 kA |

Table 7 and Table 8 show that the proposed model can reach lower values with respect to the ones proposed in [15] ,[17] and [72]. In particular, the proposed function can reach lower percentiles of the probabilistic function of the maximum derivative according to the distribution proposed in [1].

**Table 7 Comparison of the minimum values of the maximum derivative that can be described by different models – First strokes**

| | | Minimum value of the maximum derivative [kA/ µs] and corresponding minimum percentile | | | | | |
|---|---|---|---|---|---|---|---|
| Peak current [kA] | Front duration [µs] | Heidler[15] | | Andreotti [72]and Javor [17] | | Proposed function | |
| 24.12 | 4.16 | 15.07 | 21th | 9.91 | 7th | 7.77 | 3rd |
| 24.12 | 5.63 | 11.14 | 10th | 7.33 | 3th | 5.74 | 1st |
| 24.12 | 7.61 | 8.23 | 4th | 5.41 | 1st | 4.25 | 1st |
| 31.1 | 4.16 | 19.42 | 36th | 12.77 | 14th | 10.01 | 7th |
| 31.1 | 5.63 | 14.36 | 19th | 9.44 | 6th | 7.40 | 2nd |
| 31.1 | 7.61 | 10.62 | 9th | 6.98 | 2nd | 5.47 | 1st |
| 40.08 | 4.16 | 25.04 | 52th | 16.47 | 26th | 12.90 | 14th |
| 40.08 | 5.63 | 18.51 | 33th | 12.17 | 13th | 9.54 | 5th |
| 40.08 | 7.61 | 13.68 | 17th | 9.00 | 5th | 7.05 | 2th |

**Table 8 Comparison of the minimum values of the maximum derivative that can be described by different models – Subsequent strokes**

| | | Minimum value of the maximum derivative [kA/ μs] and corresponding minimum percentile | | | | | |
|---|---|---|---|---|---|---|---|
| Peak current [kA] | Front duration [μs] | Heidler[15] | | Andreotti [72]and Javor [17] | | Proposed function | |
| 9.32 | 0.46 | 52.34 | 63$^{th}$ | 34.43 | 44$^{th}$ | 26.98 | 32$^{nd}$ |
| 9.32 | 0.75 | 32.29 | 41$^{th}$ | 21.24 | 23$^{th}$ | 16.64 | 15$^{th}$ |
| 9.32 | 1.21 | 19.92 | 21$^{th}$ | 13.10 | 10$^{th}$ | 10.27 | 5$^{th}$ |
| 12.3 | 0.46 | 69.11 | 74$^{th}$ | 45.45 | 57$^{th}$ | 35.62 | 44$^{th}$ |
| 12.3 | 0.75 | 42.64 | 53$^{th}$ | 28.04 | 34$^{th}$ | 21.98 | 24$^{th}$ |
| 12.3 | 1.21 | 26.30 | 32$^{th}$ | 17.30 | 17$^{th}$ | 13.56 | 10$^{th}$ |
| 16.24 | 0.46 | 91.25 | 84$^{th}$ | 60.02 | 69$^{th}$ | 47.03 | 57$^{th}$ |
| 16.24 | 0.75 | 56.30 | 67$^{th}$ | 37.03 | 47$^{th}$ | 29.01 | 35$^{th}$ |
| 16.24 | 1.21 | 34.74 | 44$^{th}$ | 22.84 | 26$^{th}$ | 17.90 | 17$^{th}$ |

## 3.4 Standard parameters of the proposed CBC function

This section aims at providing the parameters of the proposed CBC function in accordance to different standards or measurements.

### 3.4.1 Berger's data

The data are taken from the median values of negative and positive strokes described in [9] in terms of peak current, front duration, maximum derivative, time-to-half value and total charge (Table 9).

**Table 9 Berger's median values**

| Parameter | Negative first | Negative subsequent | Positive |
|---|---|---|---|
| $I_M$ [kA] | 30 | 12 | 35 |
| Front duration [μs] | 5.5 | 1.1 | 22 |
| λ [kA/ μs] | 12 | 40 | 2.4 |
| $t_{50}$ [μs] | 75 | 32 | 230 |
| $Q$ [C] | 5.2 | 1.4 | 80 |

The parameter of the function are provided in Table 10:

**Table 10 Proposed function parameters with Berger's data**

| Parameter | | Negative first | Negative subsequent | Positive |
|---|---|---|---|---|
| $k_1^2$ [kA/μs$^2$] | | 1.204 | 8.55 $10^{-7}$ | 0.757 |
| $k_2$ [kA] | | 30.0162 | 12 | 36.570 |
| $a$ [1/ μs] | | 0.466 | 3.886 | 0.765 |
| $k_3$ [kA] | | 30 | 12 | 35 |
| $k_4$ [kA] | | -0.0162 | 0 | -1.570 |
| $k_5$ [kA] | | 0 | 0 | 0 |
| $b$ [1/ μs] | $t_{50}$ *priority* | 0.0012 | 0.027 | 0.004 |
| | $Q$ *priority* | 0.005 | 0.007 | 0.0004 |
| $t_1$ [μs] | | 0.0176 | 0.001 | 0.291 |
| $t_M$ [μs] | | 5.89 | 1.32 | 23.33 |
| $n$ | | 2 | 2 | 2 |

### 3.4.2 IEEE Standard [1]

In this section the parameters of the channel-base current are given for first and subsequent negative strokes according to the data provided in [1] and presented also in Table 5.

**Table 11 Proposed function parameters with IEEE standard data**

| Parameter | | Negative first | Negative subsequent |
|---|---|---|---|
| $k_1^2$ [kA/μs$^2$] | | $1.23\ 10^{-7}$ | 19.649 |
| $k_2$ [kA] | | 31.1 | 12.304 |
| $a$ [1/ μs] | | 0.911 | 3.78 |
| $k_3$ [kA] | | 31.1 | 12.3 |
| $k_4$ [kA] | | 0 | -0.004 |
| $k_5$ [kA] | | 0 | 0 |
| $b$ [1/ μs] | $t_{50}$ *priority* | 0.011 | 0.028 |
| | $Q$ *priority* | 0.0059 | 0.011 |
| $t_1$ [μs] | | 0.0047 | 0.0022 |
| $t_M$ [μs] | | 5.63 | 0.75 |
| $n$ | | 2 | 2 |

### 3.4.3 Society of Automotive Engineers (SAE) standard

In this section the parameters of the new CBC function are proposed in order to reproduce the CBC provided in the standard used in the lightning protection of aircraft vehicles, commonly known as ABCD current, whose properties can be found in Table 12 [87].

**Table 12 ABCD parameters [87]**

| Standard component | Peak [kA] | Charge [C] | Action Integral [$A^2s$] | Duration |
|---|---|---|---|---|
| A | 200 | N/A | $2\ 10^6$ | < 500 μs |
| B | 2 (average) | 10 | N/A | < 5 ms |
| C | 0.2-0.8 | 200 | N/A | 0.25 -1s |
| D | 100 | N/A | $0.25\ 10^6$ | < 500 μs |

The ABCD current refers to two strokes in a flash: the components ABC refer to the first stroke while the component D refers to the subsequent stroke.

Since our CBC function represents the channel-base current of a single stroke, in the following, only ABC components are accounted.

In this case the CBC is not expressed in terms of the values shown in the other standards (front duration, maximum steepness,…) but as the peak current, total charge, action integral and total duration of each component (Table 12). Consequently the procedure proposed in Section II for the computation of the CBC parameters cannot be adopted. In the following, the parameters of the proposed function are evaluated through an optimization procedure which receives as input the lightning data of Table 12. Results appear in Table 13.

**Table 13 Proposed function parameters with SAE standard data**

| Parameter | Value |
|---|---|
| $k_1^2$ [kA/μs$^2$] | $5.33\ 10^{-7}$ |
| $k_2$ [kA] | 199.99 |
| $a$ [1/ μs] | 0.025 |
| $k_3$ [kA] | 198 |
| $k_4$ [kA] | 0.01 |
| $k_5$ [kA] | 2 |
| $b$ [1/ μs] | 0.025 |
| $t_1$ [μs] | 146 |
| $t_M$ [μs] | 285 |

# 4 Analytical expressions for the lightning electromagnetic fields

In some applications, such as the lightning performance, a huge number of field calculations is required, which makes the computational performances of such calculation a crucial aspect for this kind of application. Two main solutions have been adopted in literature: i) analytical formulas for the electromagnetic fields over a perfectly conducting ground have been derived in [36] assuming that the channel base current is a trapezoidal; ii) a field database is constructed in [35] where electromagnetic fields generated by a current with a specified time domain waveform with unitary peak at different distances are computed. The fields necessary to input the coupling equations are then calculated interpolating the database elements. According to [37], the first approach can fail when the presence of arresters and flashovers is accounted. On the other hand, the database approach exploits the linear relationship between current peak and electromagnetic fields; but, when one aims at accounting for the front time effect, the computational convenience of the method falls because one database should be constructed for any considered value of the front time.

This chapter proposes analytical formulas for lightning electromagnetic fields generated by an arbitrary shaped channel base current over perfectly conducting or lossy ground. The idea of the method consists of dividing the channel into intervals in which the distance between the source and the observation field points can be approximated with a linear function of the time and of their spatial coordinates. Sections 4.1, 4.2 and 4.3 present the theory of the proposed formulation, while 4.4 and 4.5 show the validation and the computational performances.

## 4.1 Lightning electromagnetic fields over an ideal ground

The present section derives the analytical expressions for lightning electromagnetic fields over an ideal ground, starting with the magnetic field (subsection 4.1.1) necessary to evaluate the electric one (subsection 4.1.2).

### 4.1.1 Magnetic field

Let us consider the situation depicted in Figure 20 representing the lightning channel (*H* being its height).

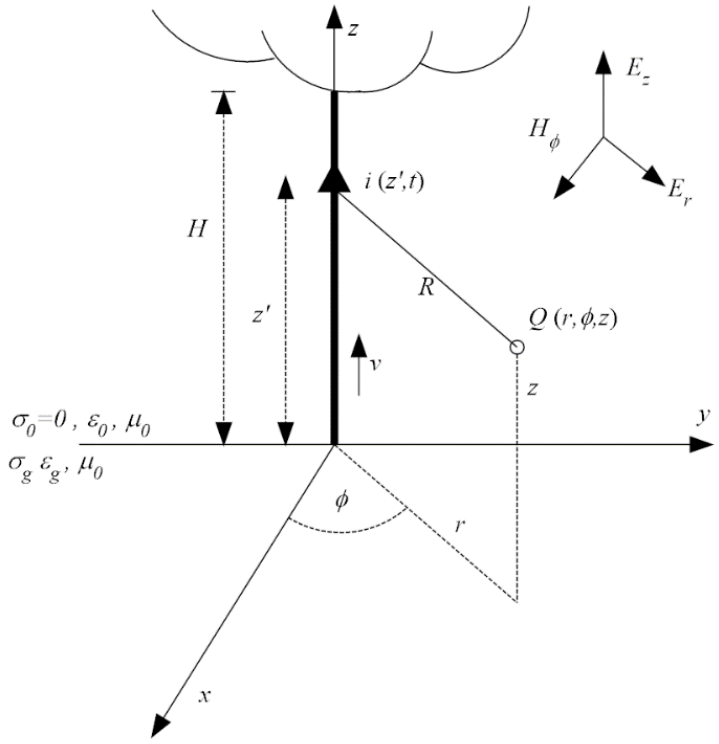


**Figure 20 Geometry of the problem**

Assuming a perfect ground conductivity and supposing that the lightning current starts propagating from the channel base (z'=0) at t=0 and applying the method of images, the azimuthal component of the magnetic field produced in the observation point $Q(r,\phi,z)$ is given by [20]:

$$H_\phi^{id}(r,z,t)=\frac{r}{4\pi}\int_{-H}^{H}\left[\frac{1}{R^3(z')}i_0\left(\xi(z')\right)+\right.$$
$$\left.+\frac{1}{c_0R^2(z')}i'_0\left(\xi(z')\right)\right]\cdot P(|z'|)1\left(\xi(z')\right)dz' \qquad (142)$$

where $\xi(z',t)=t-\frac{R(z')}{c_0}-\frac{|z'|}{v}$; $c_0$ and $v$ are the speed of light in vacuum and the return stroke speed; $P$ is the attenuation function [2]; $1(t)$ is the Heaviside function, $i_0(t)$ is the channel base current(supposed to be zero for negative time) and $i_0'$ its first derivative; $R$ is the distance between the source and the observation point, defined as

$$R(z')=\sqrt{r^2+(z-z')^2} \qquad (143)$$

It can be shown that, after some algebraic manipulations and assuming $P(z')=1$, the magnetic field can be written as :

$$H_{\phi}^{id}(r,z,t)=\frac{c_0}{2\pi rv}i_0\left(t-\frac{R(0)}{c_0}\right)+\frac{c_0}{4\pi r}\left(\frac{1}{c_0^2}-\frac{1}{v^2}\right)\cdot \cdot\int_{-H}^{H}i_0'\left(\xi(z',t)\right)1\left(\xi(z',t)\right)dz' \tag{144}$$

Introducing

$$x=\frac{z'-z}{r}\quad\text{and}\quad f\left(x\right)=\sqrt{1+x^2} \tag{145}$$

(144) becomes

$$H_{\phi}^{id}(r,z,t)=\frac{c_0}{2\pi rv}i_0\left(t-\frac{R(0)}{c_0}\right)+ +\frac{c_0}{4\pi r}\left(\frac{1}{c_0^2}-\frac{1}{v^2}\right)\left[I_{image}+I_{source}\right] \tag{146}$$

where

$$I_{image}=r\int_{-\frac{H+z}{r}}^{-\frac{z}{r}}i_0'\ \left(\xi_{r,z,t}^{i,0}(x,t)\right)\cdot 1\left(\xi_{r,z,t}^{i,0}(x,t)\right)dx \tag{147}$$

having posed

$$\xi_{r,z,t}^{i,0}(x,t)=t-\frac{r}{c_0}f(x)+\frac{z+rx}{v} \tag{148}$$

and

$$I_{source}=r\int_{-\frac{z}{r}}^{0}i_0'\left(\xi_{r,z,t}^{s,0}(x,t)\right)\cdot 1\left(\xi_{r,z,t}^{s,0}(x,t)\right)dx+ +r\int_{0}^{\frac{H-z}{r}}i_0'\left(\xi_{r,z,t}^{s,0}(x,t)\right)\cdot 1\left(\xi_{r,z,t}^{s,0}(x,t)\right)dx \tag{149}$$

having posed

$$\xi_{r,z,t}^{s,0}(x,t)=t-\frac{r}{c_0}f(x)-\frac{z+rx}{v} \tag{150}$$

Relation (149) is separated in two parts, corresponding to positive and negative values of the integration variable; this will be useful in the following description of the procedure.

The main problem in analytically solving integrals in (147) and (149) is that *f* is a nonlinear function of *x*. If this was not the case, one could *i*) analytically solve the inequalities expressing the condition for the Heaviside function not to be zero and *ii*) perform a linear change of variable in the argument of $i_0'$ for the calculation of the integral. So, the main idea of the method is to divide the channel and its image into *N*+1 intervals; in each of them *f* can be approximated by

the secant passing through its extremes. This introduces a piecewise linear function *g*, defined as

$$g(x)=\begin{cases} a_1|x|+b_1 & \alpha_0 \le |x| \le \alpha_1 \\ \vdots & \\ a_N|x|+b_N & \alpha_{N-1} \le |x| \le \alpha_N \\ a_{N+1}|x|+b_{N+1} & \alpha_N \le |x| \le \alpha_{N+1} \end{cases} \tag{151}$$

where $\alpha_0 = 0$ and $\alpha_{N+1} = A$[4]. Imposing that $f(\alpha_j) = g(\alpha_j)$ for any $j = 1,\ldots,N+1$ one has

$$a_j = \frac{f(\alpha_j) - f(\alpha_{j-1})}{\alpha_j - \alpha_{j-1}} \quad \text{and} \quad b_j = f(\alpha_j) - a_j\alpha_j \tag{152}$$

From here on we will use the approximate formulas $\xi^i_{r,z,t}$ for $\xi^{i,0}_{r,z,t}$ and $\xi^s_{r,z,t}$ for $\xi^{s,0}_{r,z,t}$ obtained inserting *g* defined in (151) instead of *f* into (148) and (150). Please note that (145) has the advantage that the piecewise linear approximation *g* of the function *f* has to be done just once no matter the coordinates of the observation point. Details on the approximation and on the choice of the intervals are provided in Section 4.3, while a graphical sketch of the whole procedure can be found in Figure 21.

[4] A should be chosen such that *g* approximates *f* along all the portion of the channel that contributes to the field in the desired time window. Details on the choice of *A* will be provided in the following sections.

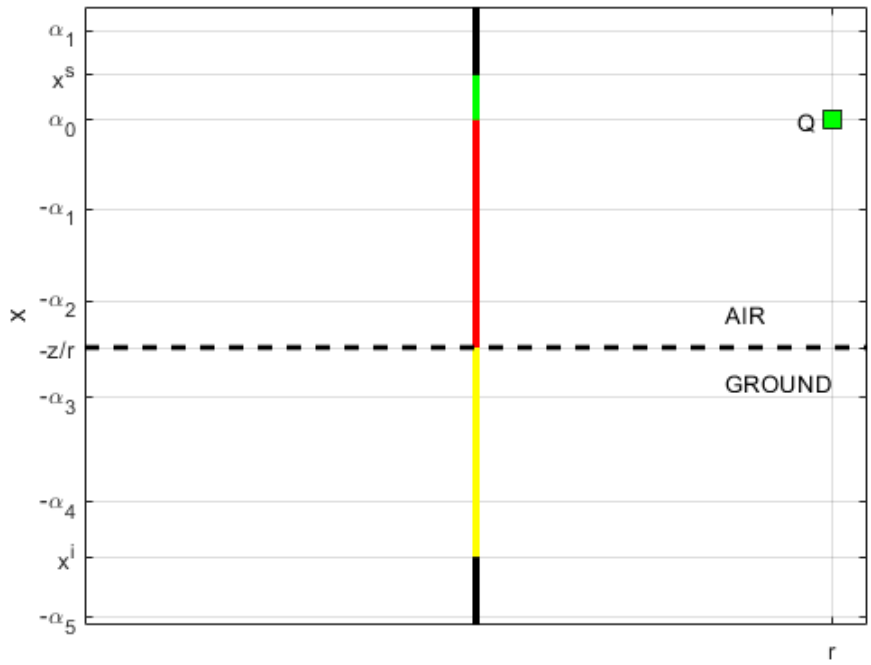


**Figure 21 Definition of the intervals in which the channel is divided**

Let's start with the calculation of the image channel contribution to the magnetic field (Eq.(147) ). Due to the Heaviside function, (147) is not trivial if $\xi^i_{r,z,t}(x) > 0$, which, at fixed $r$ and $z$, defines the region depicted in Figure 22.

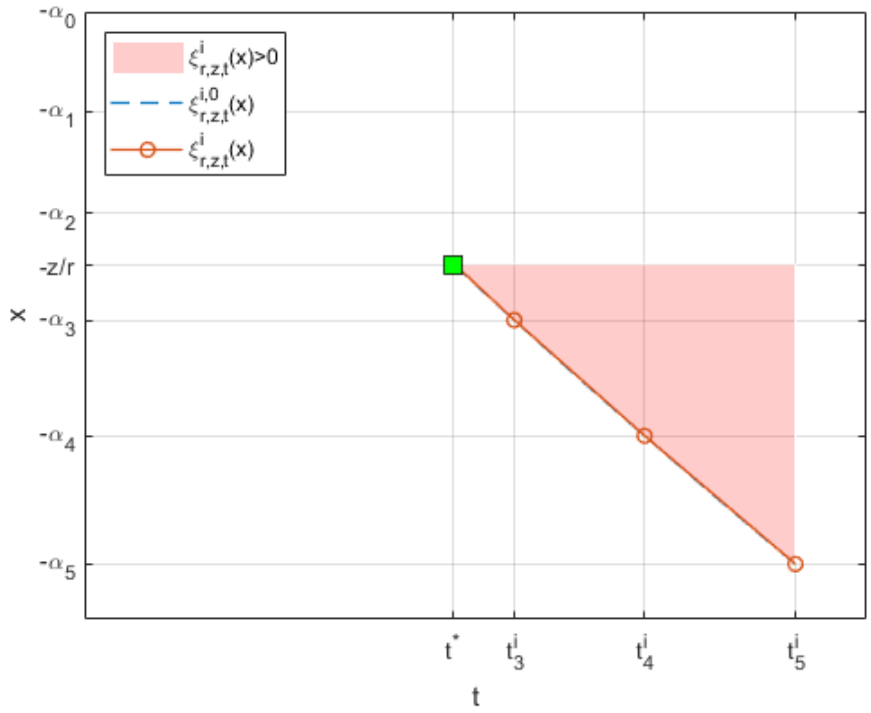


**Figure 22 Graphical view of the region $\xi^i_{r,z,t}(x)>0$ for fixed *r* and *z* when j*=3**

First of all, one has to find the interval in which $x=-z/r$ lays, i.e. find $j^*\in\{1,\ldots,N\}$ such that $-\alpha_{j^*}\le -z/r\le -\alpha_{j^*-1}$ (in Figure 22, $j^*$=3). Then the time instant $t_*$ before which the fields in Q are zero can be found as follows:

$$\xi^i_{r,z,t_*}\left(-\frac{z}{r}\right)=0\Rightarrow t_*=\frac{b_{j^*}}{c_0}r+\frac{a_{j^*}}{c_0}z \tag{153}$$

Moreover, the time instants $t^i_j$ for which the dipole at point $-\alpha_j$ contributes to the fields in *Q* are given by:

$$\xi^i_{r,z,t^i_j}\left(-\alpha_j\right)=0\Rightarrow t^i_j=\left(\frac{a_i\alpha_j+b_j}{c_0}+\frac{\alpha_j}{v}\right)r-\frac{1}{v}z \tag{154}$$

This defines the following sequence of time instants $t^i_N>\ldots>t^i_{j^*}\ge t_*$

Finally, for a fixed time $t\ge t_*$ the portion of the image that contributes to the fields in *Q* is given by solving the following inequality:

$$\xi^i_{r,z,t^i_j}\left(x\right)\ge 0\Rightarrow -\frac{A^i_j}{r}\left(t-\frac{rb_j}{c_0}+\frac{z}{v}\right)=x^i\le x\le -\frac{z}{r} \tag{155}$$

where $A_j^i = \left( \frac{a_j}{c_0} + \frac{1}{v} \right)^{-1}$,

At this point, (147) can be separated in all the intervals that provide a contribute, partly or totally, to the fields. The linearity of $\xi_{r,z,t}^i$ permits to analytically solve the integral in (147) as

$$I_{image} = \begin{cases} 0 & t < t_* \\ I_{j^*}^i \left( x^i, -\frac{z}{r} \right) & t_* \le t \le t_{j^*}^i \\ I_{j^*}^i \left( -\alpha_{j^*}, -\frac{z}{r} \right) + & \\ \quad + \sum_{h=j^*+1}^{j-1} I_h^i \left( -\alpha_h, -\alpha_{h-1} \right) + I_j^i \left( x^i, -\alpha_{j-1} \right) & t_{j-1}^i \le t \le t_j^i \end{cases} \tag{156}$$

in which one has defined for any $y_1 < y_2 < 0$:

$$I_j^i(y_1, y_2) = r \int_{y_1}^{y_2} i_0' \left( t - \frac{r}{c_0} \left( -a_j x + b_j \right) + \frac{z + rx}{v} \right) dx \tag{157}$$

which is analytically solvable. More precisely, quantities in (156) can be calculated as:

$$\begin{aligned} I_{j^*}^i \left( x^i, -\frac{z}{r} \right) &= A_{j^*}^i i_0 (t - t_*) \\ I_{j^*}^i \left( -\alpha_{j^*}, -\frac{z}{r} \right) &= -A_{j^*}^i \left[ i_0 (t - t_{j^*}^i) - i_0 (t - t_*) \right] \\ I_h^i \left( \alpha_h, -\alpha_{h-1} \right) &= -A_h^i \left[ i_0 (t - t_h^i) - i_0 (t - t_{h-1}^i) \right] \\ I_j^i \left( x^i, -\alpha_{j-1} \right) &= A_j^i i_0 (t - t_{j-1}^i) \end{aligned} \tag{158}$$

(156) can be rewritten in a more compact form recalling that $i_0(t) = 0$ for $t < 0$, as follows:

$$I_{image} = A_{j^*}^i i_0 \left( t - t_* \right) + \sum_{h=j^*}^{N-1} \left( A_{h+1}^i - A_h^i \right) i_0 \left( t - t_h^i \right) \tag{159}$$

Physical interpretation of formula (156) is the following. If $t < t_*$ the propagation of the current along the channel and of the fields along the air is not sufficient to produce a nonzero magnetic field in point *Q*; if $t_* \le t < t_{j^*}^i$ only part of the first interval $\left[ -\alpha_{j^*}, -\alpha_{j^*-1} \right]$ belonging to the image channel contributes to it; if $t_{j-1}^i \le t \le t_j^i$ all the intervals $\left[ -\alpha_h, -\alpha_{h-1} \right]$ with $h \in \left\{ j^*, ..., j-1 \right\}$ and part of the interval $\left[ -\alpha_j, -\alpha_{j-1} \right]$ produce field in point *Q*.

Now, let's move to the source contribution in (149) which is not trivial if $\xi^{s}_{r,z,t}(x) > 0$, So, at fixed *r* and *z*, this condition defines the region depicted in Figure 23 (in this case $j^{*} = 3$).

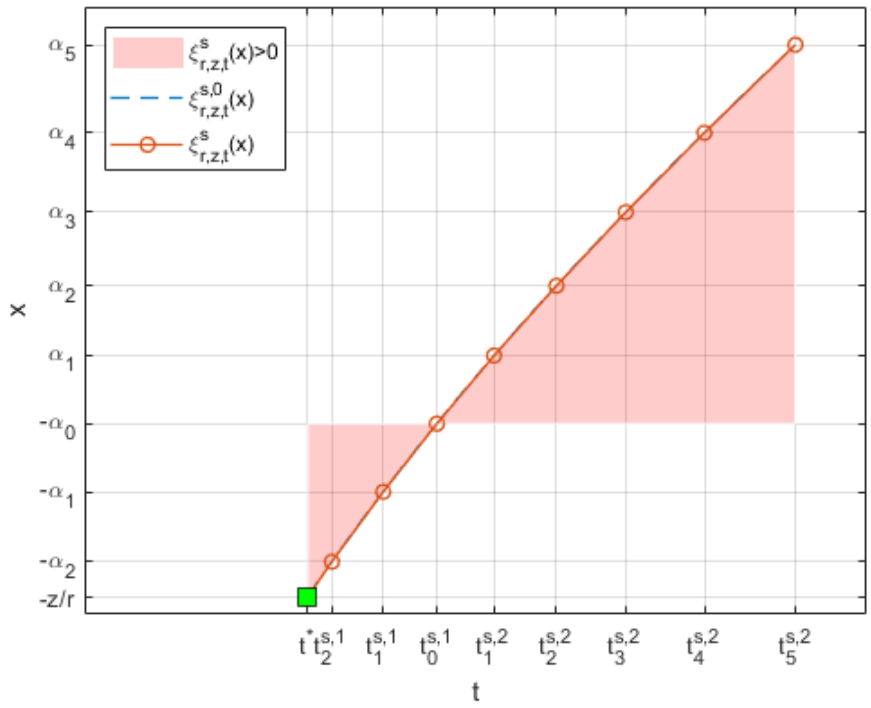


**Figure 23 Graphical view of the region $\xi^{s}_{r,z,t}(x) > 0$ for fixed r and z when j*=3**

As before, the following time sequence can be defined $t^{s,2}_{N} > \ldots > t^{s,2}_{0} = t^{s,1}_{0} > \ldots > t^{s,1}_{j^{*}-1} \geq t_{*}$ where $t^{s,2}_{0} = t^{s,1}_{0}$ is the time at which the dipole placed at $x = 0$ starts giving contribution to the field and can be obtained solving:

$$\xi^{s}_{r,z,t^{s,1}_{0}}(0) = 0 \Rightarrow t^{s,1}_{0} = \frac{1}{c_0} r + \frac{1}{v} z \tag{160}$$

Similarly, the time instants $t^{s,1}_{j}$ (for $j = 1, \ldots, j^{*} - 1$ and $j^{*} > 1$) and $t^{s,2}_{j}$ (for $j = 1, \ldots, N$) necessary for the fields generated at points $-\alpha_j$ and $\alpha_j$ to reach point *Q* are obtained respectively solving:

$$\xi^{s}_{r,z,t^{s,1}_{j}}(-\alpha_j) = 0 \Rightarrow t^{s,1}_{j} = \left( \frac{a_j \alpha_j + b_j}{c_0} - \frac{\alpha_j}{v} \right) r + \frac{1}{v} z \tag{161}$$

$$\xi^{s}_{r,z,t^{s,2}_{j}}(\alpha_j) = 0 \Rightarrow t^{s,2}_{j} = \left( \frac{a_j \alpha_j + b_j}{c_0} + \frac{\alpha_j}{v} \right) r + \frac{1}{v} z \tag{162}$$

Hence, for $t_* \le t \le t_0^{s,1}$, only part of the source channel with $x<0$ contributes to the field in point *Q*, more precisely it is given by solving the following inequality:

$$\xi_{r,z,t}^{s}(x) \ge 0 \Rightarrow -z/r \le x \le x^s = -\frac{A_j^{s,1}}{r}\left(t - \frac{rb_j}{c_0} - \frac{z}{v}\right) \tag{163}$$

where $j = \max\{h \in \{0,...,j^*-1\} : t \le t_k^{s,1} \ \forall k = 0,...,h\}$ and $A_j^{s,1} = \left(\frac{a_j}{c_0} - \frac{1}{v}\right)^{-1}$

Otherwise, if $t > t_0^{s,1} = t_0^{s,2}$ all the source channel with $x<0$ and part of the source channel with $x>0$ contribute to the field in point *Q*. So, there exists $j \in \{1,...,N\}$ such that $t_{j-1}^{s,2} \le t \le t_j^{s,2}$ and portion of the source channel with $x>0$ that produces non zero field in *Q* is given by solving the following inequality:

$$\xi_{r,z,t}^{s}(x) \ge 0 \Rightarrow 0 \le x \le x^s = \frac{A_j^{s,2}}{r}\left(t - \frac{rb_j}{c_0} - \frac{z}{v}\right) \tag{164}$$

where $A_j^{s,2} = \left(\frac{a_j}{c_0} + \frac{1}{v}\right)^{-1}$.

As in the case of the image contribution, the first integral in (149), (from now on $I_{source,1}$), can be analytically solved as follows

$$I_{source,1} = \begin{cases} 0 & t < t_* \\ I_{j^*}^{s,1}\left(-\frac{z}{r}, x^s\right) & t_* \le t \le t_{j^*-1}^{s,1} \\ I_{j^*}^{s,1}\left(-\frac{z}{r}, -\alpha_{j^*-1}\right) + & \\ + \sum_{h=j+1}^{j^*-1} I_h^{s,1}\left(-\alpha_h, -\alpha_{h-1}\right) + I_j^{s,1}\left(-\alpha_j, x^s\right) & t_j^{s,1} < t \le t_{j-1}^{s,1} \\ I_{j^*}^{s,1}\left(-\frac{z}{r}, -\alpha_{j^*-1}\right) + \sum_{h=1}^{j^*-1} I_h^{s,1}\left(-\alpha_h, -\alpha_{h-1}\right) & t > t_0^{s,1} \end{cases} \tag{165}$$

in which one has defined:

$$I_j^{s,1}(y_1, y_2) = r\int_{y_1}^{y_2} i_0'\left(t - \frac{r}{c_0}(-a_j x + b_j) - \frac{z + rx}{v}\right)dx \tag{166}$$

that is analytically solvable. Quantities in (165) can be explicitly calculated as:

$$
\begin{aligned}
I_{j^*}^{s,1}\left(-\frac{z}{r},x^s\right) &= -A_{j^*}^{s,1} i_0\left(t-t_*\right) \\
I_{j^*}^{s,1}\left(-\frac{z}{r},-\alpha_{j^*-1}\right) &= A_{j^*}^{s,1}\left[i_0\left(t-t_{j^*-1}^{s,1}\right)-i_0\left(t-t_*\right)\right] \\
I_h^{s,1}\left(-\alpha_h,-\alpha_{h-1}\right) &= A_h^{s,1}\left[i_0\left(t-t_{h-1}^{s,1}\right)-i_0\left(t-t_h^{s,1}\right)\right] \\
I_j^{s,1}\left(-\alpha_j,x^s\right) &= -A_j^{s,1} i_0\left(t-t_j^{s,1}\right)
\end{aligned}
\tag{167}
$$

Exploiting again that $i_0(t)=0$ for $t<0$, one gets the following expression for (165) :

$$
\begin{aligned}
I_{source,1} = {} & A_{j^*}^{s,1} i_0\left(t-t_*\right)+ \\
& +\sum_{h=1}^{j^*-1}\left(A_{h+1}^{s,1}-A_h^{s,1}\right) i_0\left(t-t_h^{s,1}\right)+A_1^{s,1} i_0\left(t-t_0^{s,1}\right)
\end{aligned}
\tag{168}
$$

Physical interpretation of formula (165) is the following: if $t<t_*$, the propagation of the current along the channel and of the fields along the air is not sufficient to produce a nonzero magnetic field in point *Q*; if $t_* \le t \le t_{j^*-1}^{s,1}$, only part of the interval between ground and the first point in which *g* is sampled contributes to the field in point *Q*; if $t_j^{s,1} < t \le t_{j-1}^{s,1}$, with $j=1,...,j^*-1$ all the intervals $\left[-\alpha_h,-\alpha_{h-1}\right]$ with $h\in\left\{2,...,j^*-1\right\}$ and part of the interval $\left[-\alpha_1,0\right]$ produce fields in point *Q*, finally if $t>t_0^{s,1}$ all the source channel $\left[-z/r,0\right]$ gives a contribution to the magnetic field.

The second term in (149) (from now on $I_{source,2}$) is much easier to evaluate because this part of the channel is all in the air and all characterized by positive value of the integral variable *x*. As a consequence, as before, one has that:

$$
I_{source,2} = \begin{cases} 0 & t<t_0^{s,2} \\ \sum_{h=1}^{j-1} I_h^{s,2}\left(\alpha_{h-1},\alpha_h\right)+I_j^{s,2}\left(\alpha_{j-1},x^s\right) & t\ge t_0^{s,2} \end{cases}
\tag{169}
$$

where

$$
I_j^{s,2}(y_1,y_2) = r\int_{y_1}^{y_2} i_0'\left(t-\frac{r}{c_0}(a_j x+b_j)-\frac{z+rx}{v}\right)dx
\tag{170}
$$

that is analytically solvable, as

$$
\begin{aligned}
I_h^{s,2}\left(\alpha_{h-1},\alpha_h\right) &= -A_h^{s,2}\left[i_0\left(t-t_h^{s,2}\right)-i_0\left(t-t_{h-1}^{s,2}\right)\right] \\
I_j^{s,2}\left(\alpha_{j-1},x^s\right) &= A_j^{s,2} i_0\left(t-t_{j-1}^{s,2}\right)
\end{aligned}
\tag{171}
$$

Finally, recalling again that $i_0(t)=0$ for $t<0$, one gets that (169) becomes:

$$I_{source,2}=A_1^{s,2}i_0\left(t-t_0^{s,2}\right)+\sum_{h=1}^{N}\left(A_{h+1}^{s,2}-A_h^{s,2}\right)i_0\left(t-t_h^{s,2}\right) \tag{172}$$

and its physical interpretation is the same as before.

In spite of the cumbersome derivation of such formulas, its application is very easy and can be summarized in the following steps:

- divide the channel according to the method proposed in 4.3 and evaluate points $\alpha_j$ and coefficients $a_j, b_j$
- calculate $t_*$ with (153), $t_j^i$ with (154), $t_0^{s,1}=t_0^{s,2}$ with (160), $t_j^{s,1}$ with (161) and $t_j^{s,2}$ with (162)
- apply (159) to evaluate the integral in (147) and (168)-(172) to evaluate the two integrals in (149).

### 4.1.2 Electric field

Maxwell equations applied to the geometry of Figure 20 allow to state that the vertical and radial components of the electric fields can be calculated as [8]

$$\begin{aligned}E_r^{id}(t)&=-\mu_0c_0^2\int_0^t\frac{\partial H_\phi^{id}}{\partial z}d\tau\\ E_z^{id}(t)&=\mu_0c_0^2\int_0^t\frac{1}{r}\frac{\partial(rH_\phi^{id})}{\partial r}d\tau\end{aligned} \tag{173}$$

It is sufficient to derive the magnetic field with respect to either *r* and *z* and to integrate along the time. The dependence on the spatial variables *r* and *z*, contained in the definition of the time instants (153)-(154), (160)-(161) and (162), is linear; this allows to apply the derivation and integration rules for constant functions and solve analytically (173) integrals as follows:

$$\begin{aligned}\int_0^t\frac{\partial H_\phi^{id}}{\partial z}d\tau=&\frac{-z}{2\pi rvR(0)}i_0\left(t-\frac{R(0)}{c_0}\right)+\\ &+\frac{c_0}{4\pi r}\left(\frac{1}{c_0^2}-\frac{1}{v^2}\right)\left[\int_0^t\frac{\partial I_{image}}{\partial z}d\tau+\int_0^t\frac{\partial I_{source}}{\partial z}d\tau\right]\end{aligned} \tag{174}$$

and

$$\begin{aligned}\int_0^t\frac{1}{r}\frac{\partial(rH_\phi^{id})}{\partial r}d\tau=&\frac{-1}{2\pi vR(0)}i_0\left(t-\frac{R(0)}{c_0}\right)+\\ &+\frac{c_0}{4\pi r}\left(\frac{1}{c_0^2}-\frac{1}{v^2}\right)\left[\int_0^t\frac{\partial I_{image}}{\partial r}d\tau+\int_0^t\frac{\partial I_{source}}{\partial r}d\tau\right]\end{aligned} \tag{175}$$

Indicating with $\zeta$ the spatial variable ($\zeta \equiv r$ or $\zeta \equiv z$)

$$\int_0^t \frac{\partial I_{image}}{\partial \zeta} d\tau = -A^i_{j^*} \frac{\partial t_*}{\partial \zeta} i_0(t-t_*) - \sum_{h=j^*}^{N-1} (A^i_{h+1} - A^i_h) \frac{\partial t^i_h}{\partial \zeta} i_0(t-t^i_h) \tag{176}$$

$$\begin{aligned} \int_0^t \frac{\partial I_{source,1}(r,z,\tau)}{\partial \zeta} d\tau = & -A^{s,1}_{j^*} \frac{\partial t_*}{\partial \zeta} i_0(t-t_*) + \\ & + \sum_{h=1}^{j^*-1} (A^{s,1}_{h+1} - A^{s,1}_h) \frac{\partial t^{s,1}_h}{\partial \zeta} i_0(t-t^{s,1}_h) + A^{s,1}_1 \frac{\partial t^{s,1}_0}{\partial \zeta} i_0(t-t^{s,1}_0) \end{aligned} \tag{177}$$

$$\begin{aligned} \int_0^t \frac{\partial I_{source,2}(r,z,\tau)}{\partial \zeta} d\tau = & -A^{s,2}_1 \frac{\partial t^{s,2}_0}{\partial \zeta} i_0(t-t^{s,2}_0) + \\ & - \sum_{h=1}^{N-1} (A^{s,2}_{h+1} - A^{s,2}_h) \frac{\partial t^{s,2}_h}{\partial \zeta} i_0(t-t^{s,2}_h) \end{aligned} \tag{178}$$

Derivatives contained in the above formulas are all constants and can be easily calculated by (153)-(154), (160)-(161) and (162).

## 4.2 Cooray-Rubinstein Formula

In [27], it was shown that the ground finite conductivity can be accounted if the ideal horizontal electric field is added to the term:

$$E_{CR}(r,z,t) = -\eta H^{id}_\phi(r,0,t) - \eta \sum_{k=1}^{N_{RA}} r_k \ \chi_k(t) \tag{179}$$

where $\chi_k$ is the solution of the linear differential equation:

$$\begin{cases} \dfrac{d\chi_k}{dt} = \dfrac{c_k}{\tau_G} \ \chi_k + \dfrac{1}{\tau_G} H^{id}_\phi(r,0,t) \\ \chi_k(0) = 0 \end{cases} \tag{180}$$

Coefficients $c_k$ and $r_k$ appear in Tab.1 of [27], $N_{RA}$=12 and $\tau_G = \varepsilon / \sigma$. So, the time domain analytical expression for the Cooray-Rubinstein formula can be obtained if one solves (180).

Adopting the previously developed formulas to calculate the magnetic field at the ground level, it readily follows that $I_{image}(r,0,t) = I_{source,2}(r,0,t)$ and $I_{source,1}(r,0,t) = 0$, thus:

$$H^{id}_\phi(r,0,t) = \begin{cases} 0 & t \le \dfrac{r}{c_0} \\ \displaystyle\sum_{j=0}^{N-1} B_j i_0\left(t - t^{s,2}_{j|z=0}\right) & t > \dfrac{r}{c_0} \end{cases} \tag{181}$$

where for sake of simplicity we define

$$B_0 = \frac{c_0}{2\pi r v} + \frac{c_0}{2\pi r}\left(\frac{1}{c_0^2} - \frac{1}{v^2}\right) A_1^{s,2}$$
$$B_j = \frac{c_0}{2\pi r}\left(\frac{1}{c_0^2} - \frac{1}{v^2}\right)(A_{j+1}^{s,2} - A_j^{s,2}) \qquad j = 1,\ldots,N-1 \tag{182}$$

and $t_{j|z=0}^{s,2}$ is obtained by (160) and (162) evaluated for $z=0$, i.e.

$$t_{j|z=0}^{s,2} = \left(\frac{a_j\alpha_j + b_j}{c_0} + \frac{\alpha_j}{v}\right) r \quad \text{and} \quad t_{0|z=0}^{s,2} = \frac{r}{c_0} \tag{183}$$

Analytical solution of (180) reads:

$$\mathcal{X}_k(t) = \frac{1}{\tau_G} \mathrm{e}^{\frac{c_k}{\tau_G}t} \int_{\tau=0}^{t} \mathrm{e}^{-\frac{c_k}{\tau_G}\tau} H_\phi^{id}(r,0,\tau)\, d\tau \tag{184}$$

Assuming now that the channel base current can be expressed as the sum of $N_G$ exponential terms of the kind:

$$i_0(t) = \sum_{h=1}^{N_G} q_h \, \mathrm{e}^{s_h t} \, 1(t) \tag{185}$$

and inserting (185) into (184), integral in (181) can be analytically solved, so one gets:

$$\mathcal{X}_k(t) = \frac{1}{\tau_G} \mathrm{e}^{\frac{c_k}{\tau_G}t} \sum_{j=0}^{N-1} \sum_{h=1}^{N_G} D_{hj} G_{jhk}(t) \tag{186}$$

where

$$D_{hj} = q_h B_j \exp\left(-s_h t_{j|z=0}^{s,2}\right) \tag{187}$$

and

$$G_{jhk}(t) = \begin{cases} 0 & t \le t_{j|z=0}^{s,2} \\ \dfrac{1}{F_{hk}}\left[\mathrm{e}^{F_{hk}t} - \mathrm{e}^{F_{hk}t_{j|z=0}^{s,2}}\right] & t > t_{j|z=0}^{s,2} \end{cases} \tag{188}$$

with

$$F_{kh} = -\frac{c_k}{\tau_G} + s_h \tag{189}$$

Please note that (185) is reasonable for the most widely adopted expressions for the channel base current. It obviously holds true if one uses the Double EXPonential (DEXP [18]) and only

9 terms are required to properly represent the Heidler's current, by using the Prony's expansion ( see [88] for details).

## 4.3 Piecewise linear approximation of the distance between source and observation points

If $A>0$ and $f:[0,A]\ni x\mapsto\sqrt{1+x^2}\in[0,+\infty)$, let $g$ be a piecewise linear approximation as in (151), with $N$ a suitable positive integer, $\alpha_0=0$, $\alpha_{N+1}=A$ and $a_j$, $b_j$ as in (152) for any $j=1,...,N+1$. Since $f$ is a convex function, for any $j=1,...,N+1$ it follows that $f(x)\le g(x)$ for $x\in[\alpha_{j-1},\alpha_j]$. Then one can prove the following two properties:

1. For any $j=1,...,N+1$

$$0<a_j<1 \tag{190}$$

and

$$\frac{a_j}{c_0}-\frac{1}{v}<0 \quad \text{and} \quad \frac{a_j}{c_0}+\frac{1}{v}>0 \tag{191}$$

*Proof.* Since $f$ is increasing, the first inequality is obvious. As far as the second is concerned, using the definition in (152) one has $\sqrt{1+\alpha_j^2}-\sqrt{1+\alpha_{j-1}^2}<\alpha_j-\alpha_{j-1}$. So taking the square of both (positive) members, one gets $1+\alpha_{j-1}\alpha_j<\sqrt{1+\alpha_j^2}\sqrt{1+\alpha_{j-1}^2}$ and taking again the square one obtains $\left(\alpha_{j-1}-\alpha_j\right)^2>0$, which holds true as $\alpha_{j-1}\neq\alpha_j$ Moreover recalling that $v\le c_0$, inequalities (191)immediately follow

2. For any $j=1,...,N+1$ the function $H_j(x)=\left(a_jx+b_j\right)-f(x)$ reaches its maximum value in $[\alpha_{j-1},\alpha_j]$ in

$$x_j=\frac{a_j}{\sqrt{1-a_j^2}} \tag{192}$$

*Proof.* Note that $H_j(\alpha_j)=H_j(\alpha_{j-1})=0$ and $H_j\in C^1([\alpha_{j-1},\alpha_j])$. So the Weierstrass [89] and Rolle [90] theorems ensure that the maximum exists and corresponds to the point $x_j$ for which the first derivative of $H_j$ is zero.

The problem one has to face at this point is the following: given a number of points $N$ define a criterion on how to choose them to guarantee the best approximation of function $f$. For each

interval $[\alpha_{j-1}, \alpha_j]$, a way to obtain the best approximation is to minimize the maximum value of function $H_j$ (that is to say, to minimize the maximum difference between function *f* and its linear approximation). So, the following constrained optimization problem can be set up. Find $(\alpha_1, \alpha_2, \ldots, \alpha_N)$ that minimize

$$\sum_{j=1}^{N+1} H_j \left( \frac{a_j}{\sqrt{1-a_j^2}} \right) \tag{193}$$

s.t.

$$0 < \alpha_1 < \alpha_2 < \ldots < \alpha_N < A \tag{194}$$

and

$$a_j = \frac{\sqrt{1+\alpha_j^{\,2}} - \sqrt{1+\alpha_{j-1}^{\,2}}}{\alpha_j - \alpha_{j-1}} \tag{195}$$

## 4.4 Validation

The proposed method, from here onward called "analytical method" will be compared with the results of the so-called "numerical method", i.e. with that the numerical integration of i) the classic formulas for the ideal fields [20, 21] and ii) the time domain expression for the Cooray-Rubinstein formula. In the following, the comparison will take into account different ground conductivities and different expressions for the channel base current (Figure 24). For each of the proposed configuration, the electromagnetic fields will be evaluated at three different distances, i.e. 50 m, 200 m and 2000 m and at a height of 10 m. The details of each test are proposed in Table 14. The height of the return stroke channel is supposed to be 8 km, while the return stroke propagation velocity is $c_0/2$.

**Table 14 Details of the comparison tests. Heidler First (Subsequent) indicates the Heidler's formula with parameters typical of first (subsequent) stroke currents. Measured current is taken from a set of Lightning Measurements taken at Mount Säntis Station in Switzerland**

| **Test Details** | | | |
|---|---|---|---|
| **Test** | ***r* [m]** | **Channel base current** | **Ground Conductivity [mS/m]** |
| T1-A | 50 | Heidler First [15] | Perfect conductor |
| T1-B | 200 | Heidler First | Perfect conductor |
| T1-C | 2000 | Heidler First | Perfect conductor |
| T2-A | 50 | Heidler Subsequent [15, 84] | Perfect conductor |
| T2-B | 200 | Heidler Subsequent | Perfect conductor |
| T2-C | 2000 | Heidler Subsequent | Perfect conductor |
| T3-A | 50 | Measured subsequent stroket [88] | Perfect conductor |
| T3-B | 200 | Measured subsequent stroke | Perfect conductor |
| T3-C | 2000 | Measured subsequent stroke | Perfect conductor |
| T4-A | 50 | Heidler First | 1 |
| T4-B | 200 | Heidler First | 1 |
| T4-C | 2000 | Heidler First | 1 |
| T5-A | 50 | Heidler First | 10 |
| T5-B | 200 | Heidler First | 10 |
| T5-C | 2000 | Heidler First | 10 |

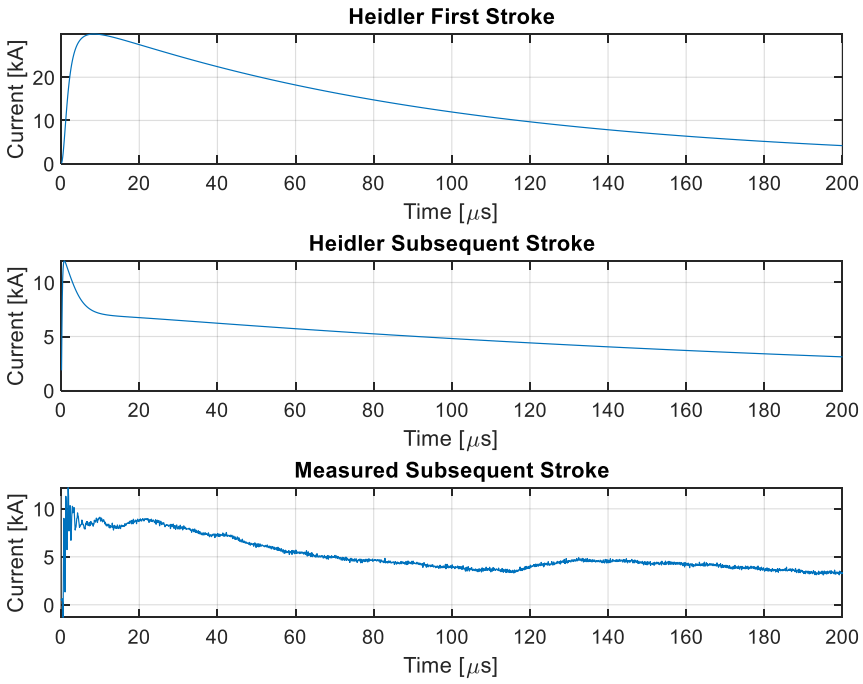


**Figure 24 Considered current waveforms**

Tests T1, T2 and T3 aim at validating the developed analytical formulas for ideal fields with different channel base currents, while tests T4 and T5 are performed to show the accuracy of the proposed expression of the Cooray Rubinstein formula.

Since the aim of this section is to validate the method without optimizing the computational effort, in this framework $N=50$ and

$$x_{\max} = \frac{H-z}{r} = \frac{8000-10}{r} = \begin{cases} 159.80 & r = 50m \\ 39.95 & r = 200m \\ 3.99 & r = 2000m \end{cases} \tag{196}$$

are chosen.

According to the procedure described in Section 4.3, the discretizing points $\alpha_j$ (with $j=1...N+1$) are plotted in Figure 25 with the three different values of $r$ (50, 200 and 2000 m).

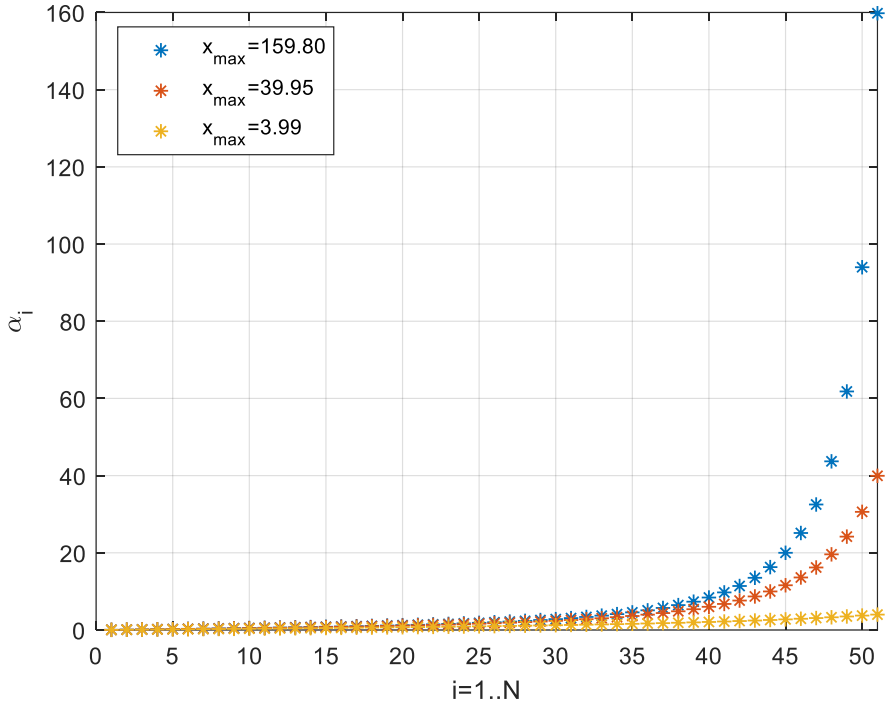


**Figure 25** **Discretizing points of *f***

As shown in the following figures, there is an excellent agreement between the proposed approach and the numerical calculation in all cases, with some slight deviations in case of a measured current [88]. Please note that the proposed approach does not need the knowledge of the time derivative of the current, which, especially with measured data, is noisy and not so easy to sense.

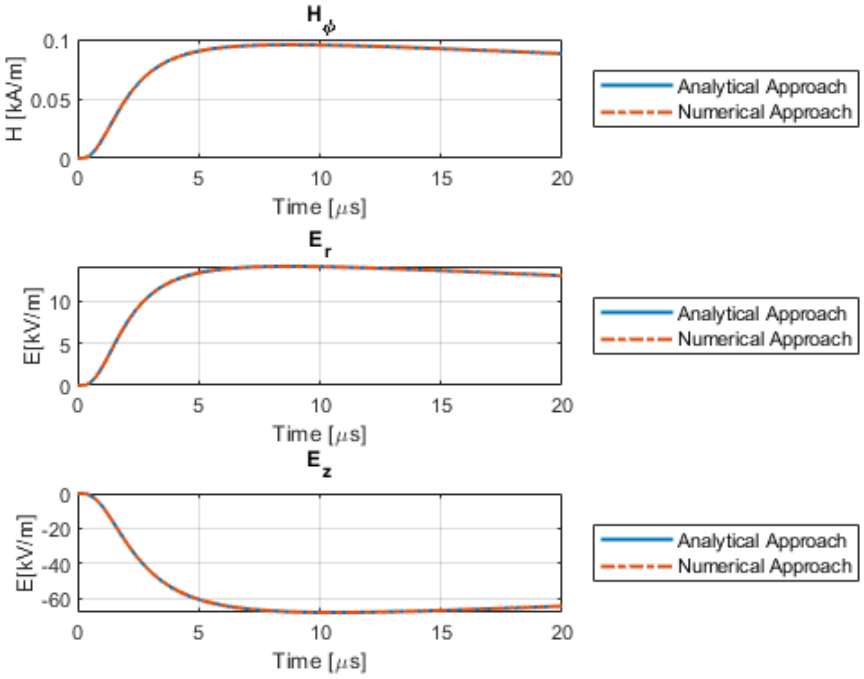


**Figure 26 Test T1-A**

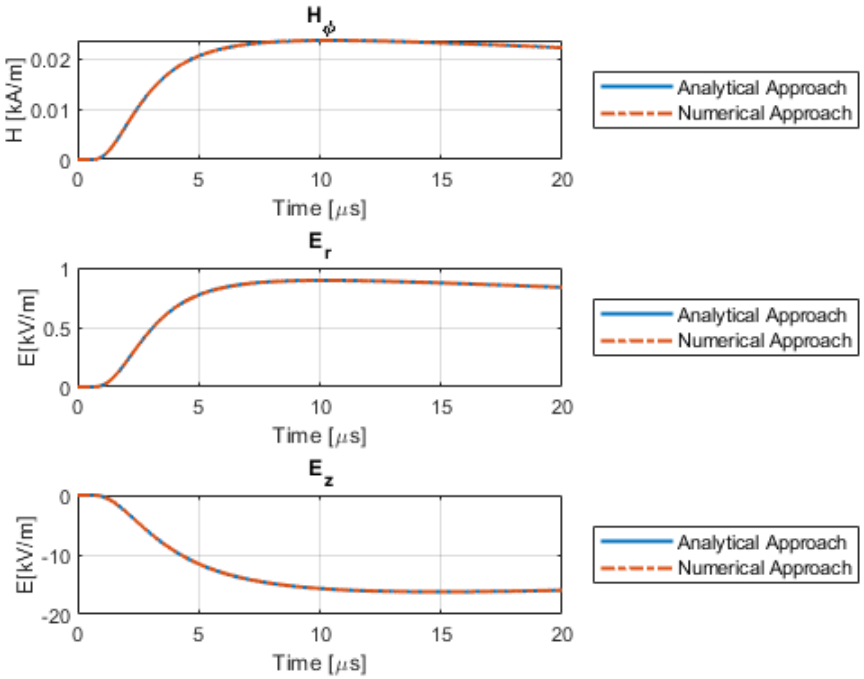


**Figure 27 Test T1-B**

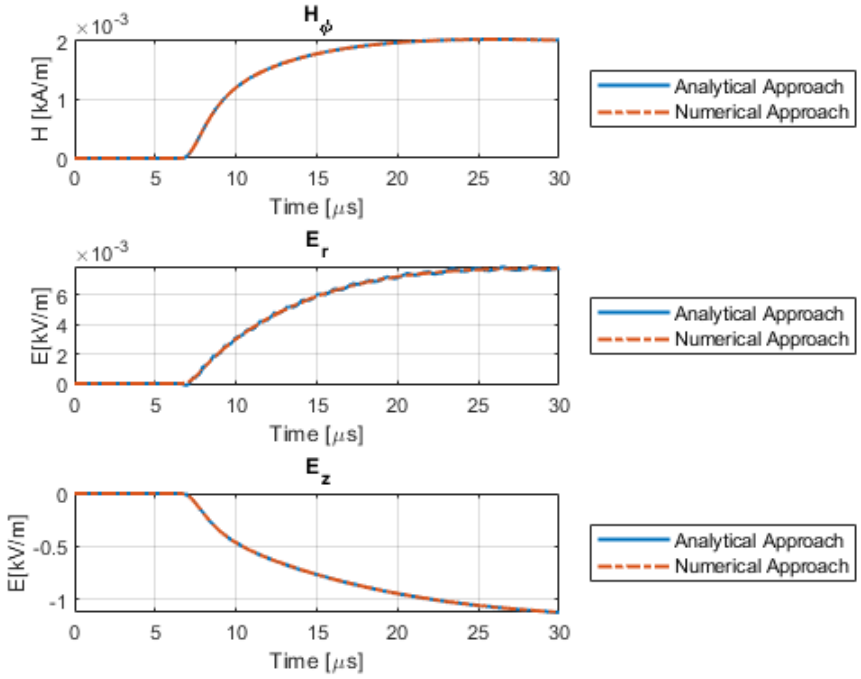


**Figure 28 Test T1-C**

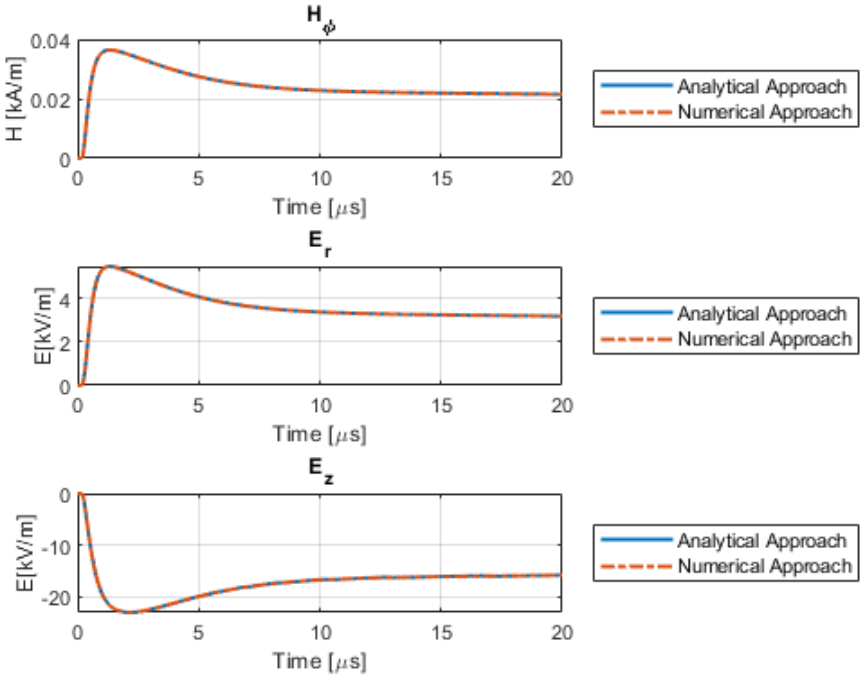


**Figure 29 Test T2-A**

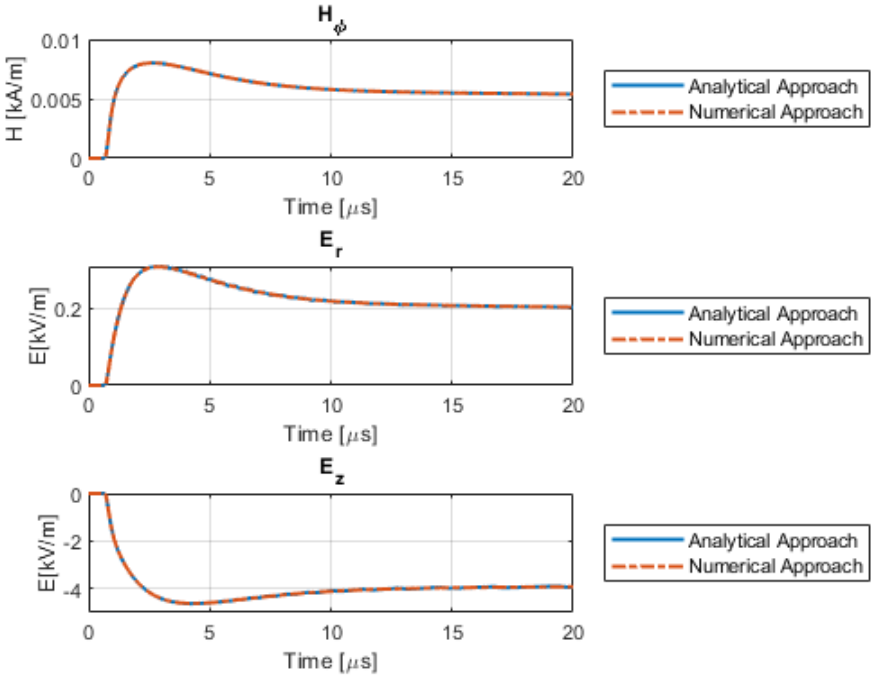


**Figure 30 Test T2-B**

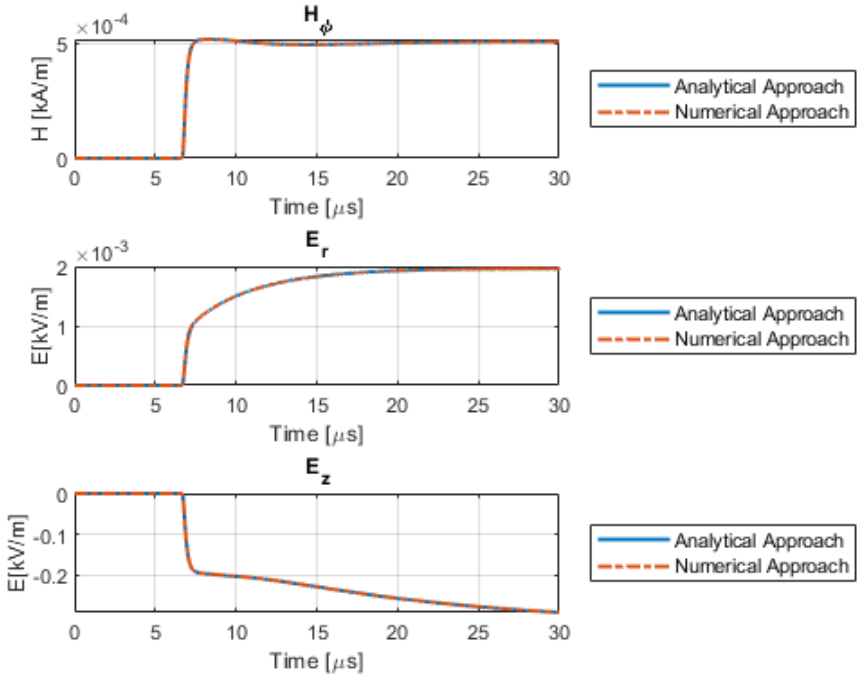


**Figure 31 Test T2-C**

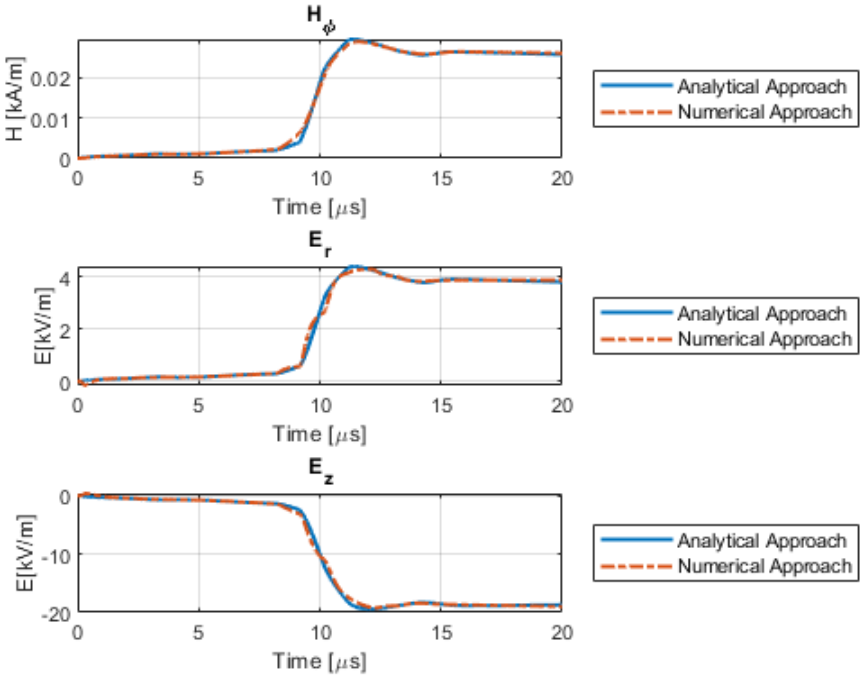


**Figure 32 Test T3-A**

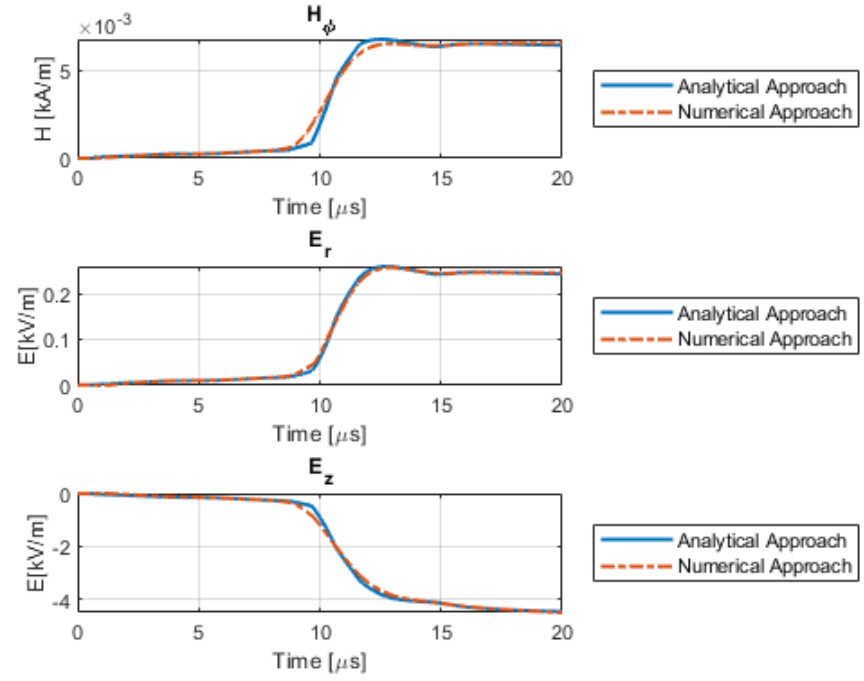


**Figure 33 Test T3-B**

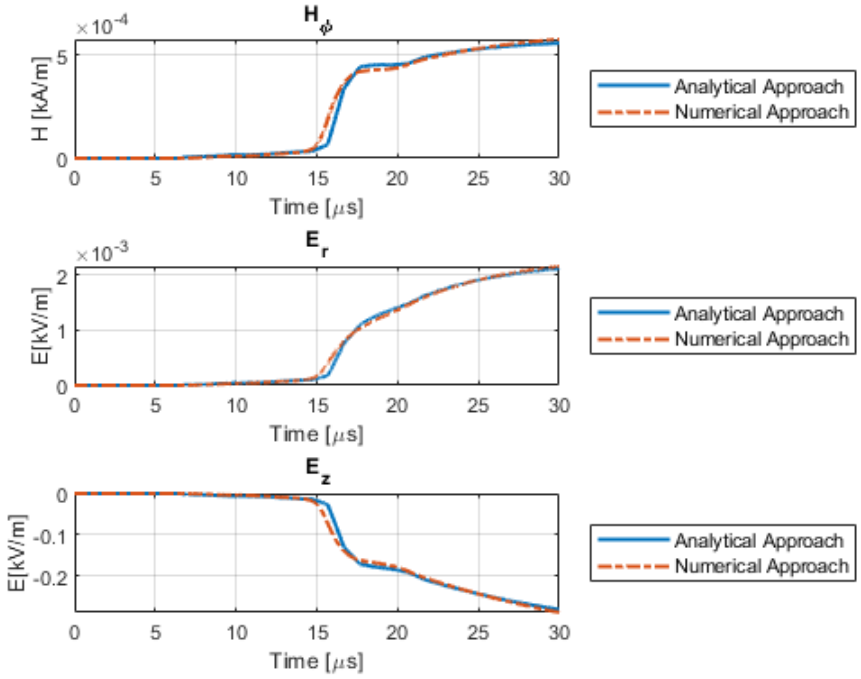


**Figure 34 Test T3-C**

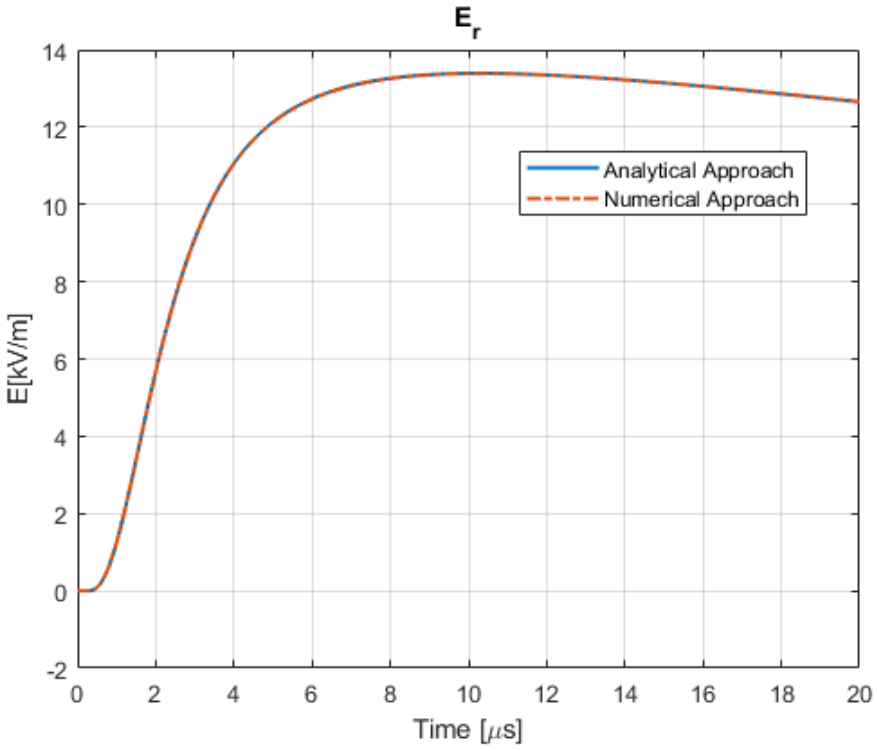


**Figure 35 Test T4-A**

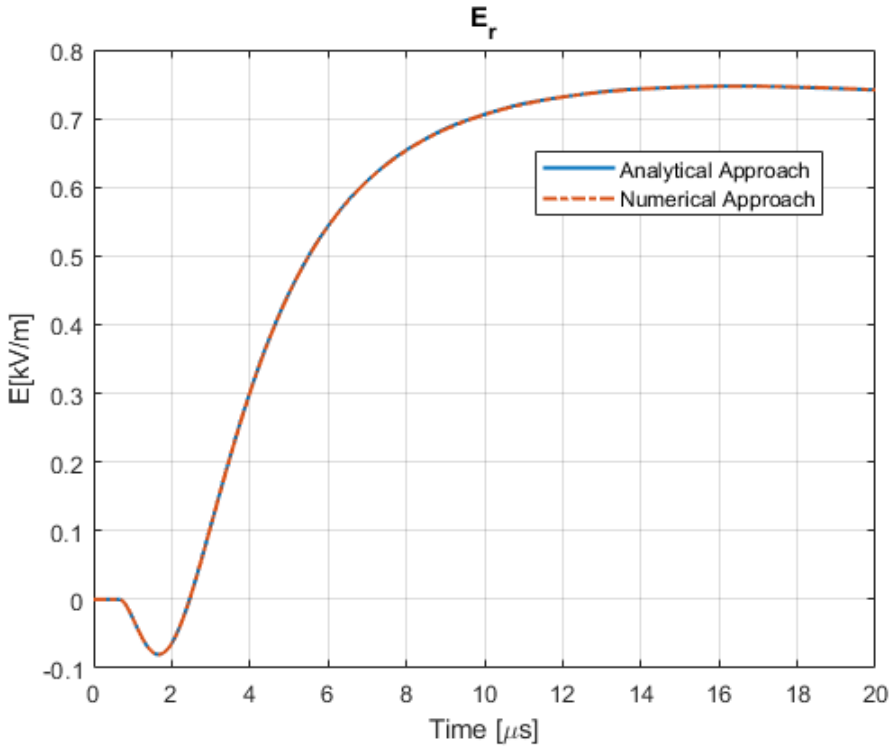


**Figure 36 Test T4-B**

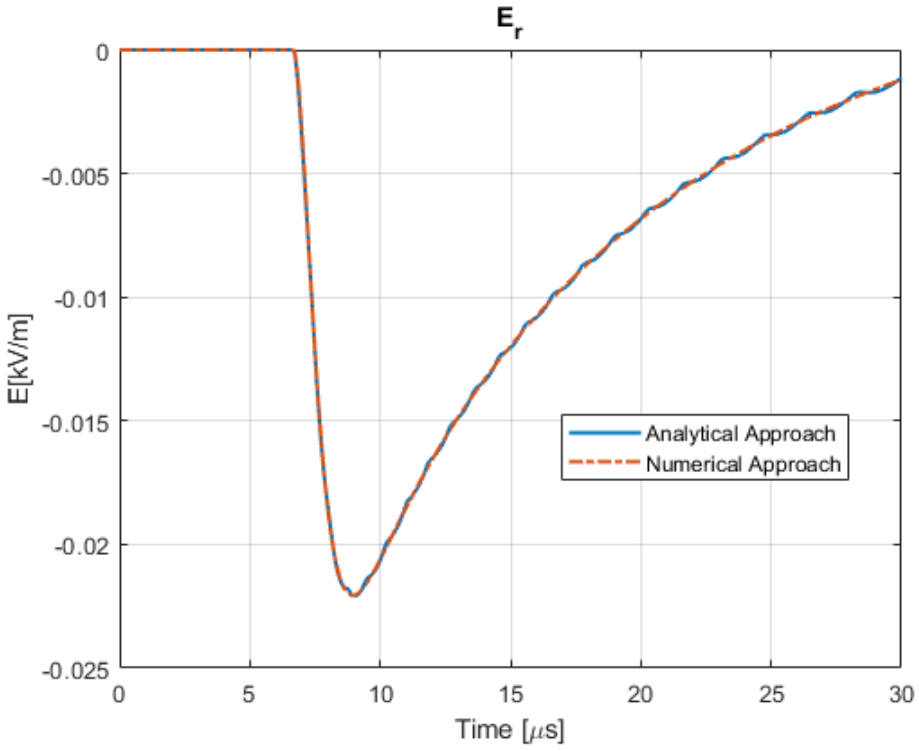


**Figure 37 Test T4-C**

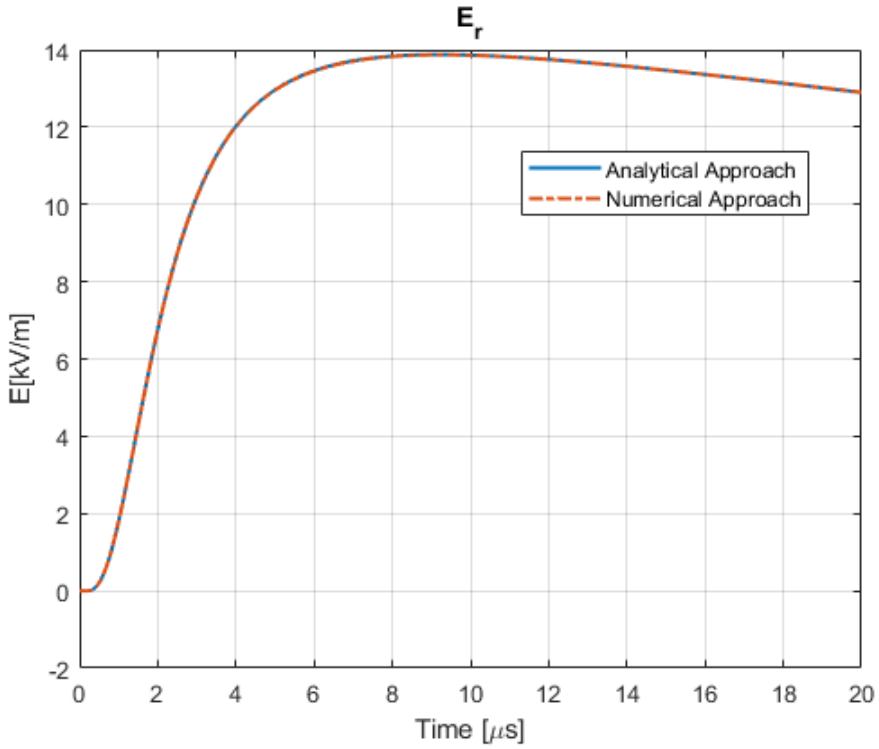


**Figure 38 Test T5-A**

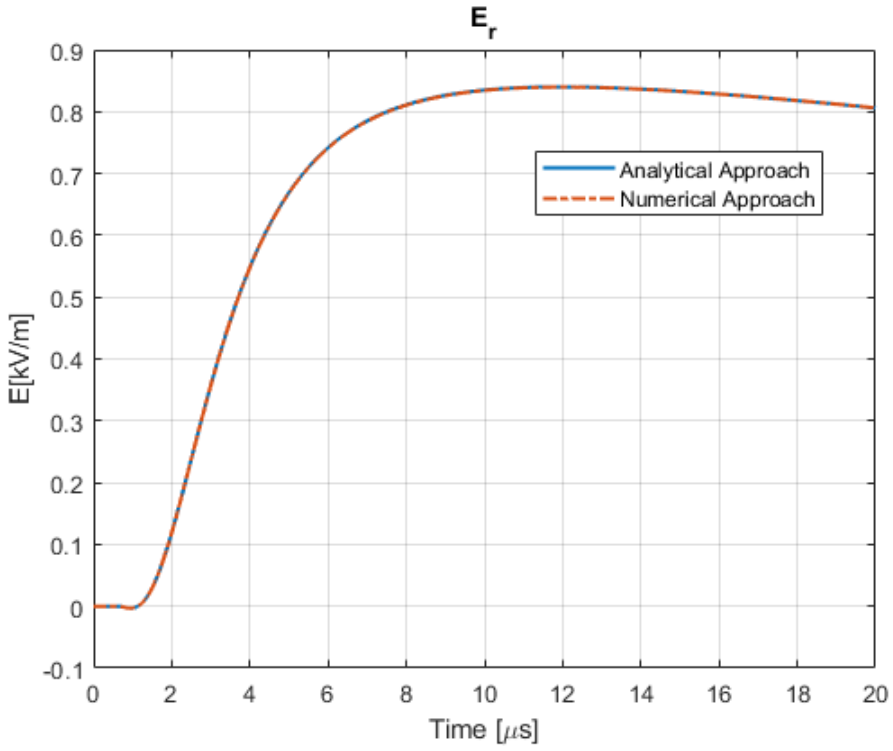


**Figure 39 Test T5-B**

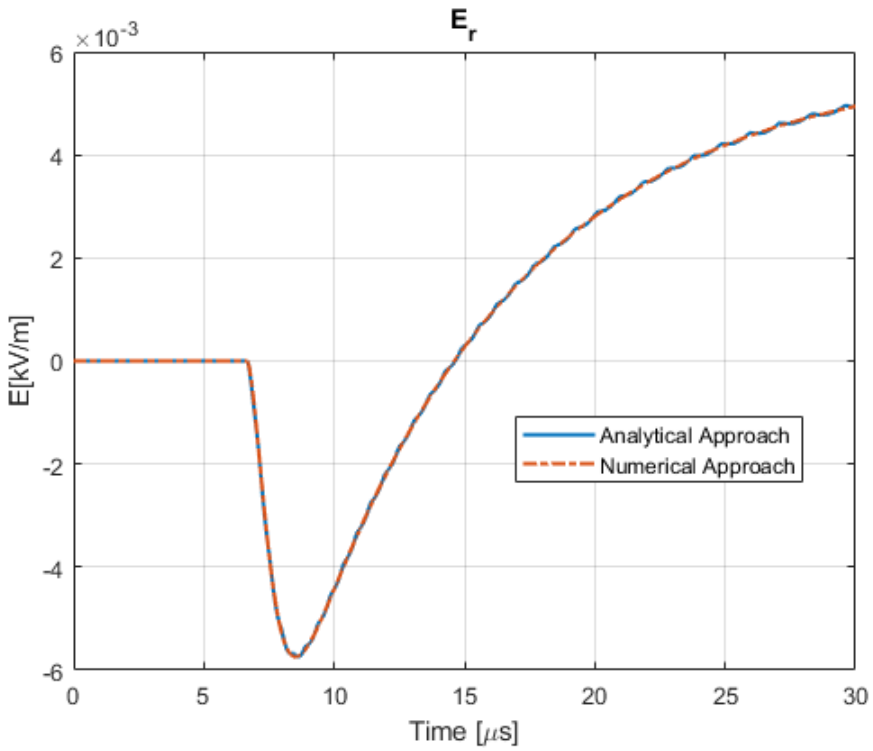


**Figure 40 Test T5-C**

## 4.5 Computational Performances

In this section, some considerations on the computational effort of the proposed method are proposed. It is important to notice that the computational effort is strictly related to the discretization of the function *f*. As highlighted in Section 4.4, two main factors can affect it: the choice of the maximum value $x_{max}$ and the number $N$ of intervals in which the function is discretized.

In the first part (sub-section 4.5.1) the focus will be on the choice of $x_{max}$, while in the second one (sub-section 4.5.2) the results of the proposed method for different values of $N$ will be analysed and discussed, showing the strength of the proposed method in terms of reduction of the computational time.

### *4.5.1* The choice of $x_{max}$

Please note that, as highlighted in Section 4.4, the value of $x_{max}$ changes according to the coordinates of point Q. This means that, in principle, the discretization of *f* changes according to *r* and *z*. This represents a big issue especially when dealing with multiple fields calculation (e.g. in any field-to-line coupling problem) because it would imply solving an optimization problem for each horizontal distance and height.

This problem can be overcome setting $x_{max}$ to the maximum value it can assume in the domain of interest of the observation point $Q$. From (196) it is easy to notice that, for an assigned return stroke channel height $H$, it corresponds to the minimum horizontal distance $r_{min}$ and to the minimum height $z_{min}$. In case of induced effects of lightning on power lines, usually a distance from the striking point closer than $r_{min}$=20 m is never considered because this would lead to a direct event and the height of a power line is never lower than $z_{min}$ =5 m. With this choice, for all the other observation points $x_{max}$ corresponds to a point outside the channel which is of no useful for the fields calculation. This means that, in principle, for all the other observation points, the points $\alpha_j$ do not optimize the objective function defined in the previous sub-sections. However, in what follows, it is shown that such error has a negligible impact on the final result.

Let us reconsider Figure 25. Despite the different values of $x_{max}$ (i.e. 159.80, 39.95 and 3.99), it can be noticed that in each case the optimization procedure sets the majority of the discretizing points close to $x$=0. This can be well explained by the graph of $f$ (Figure 41), which exhibits the maximum rate of change of its first derivative in the neighbourhood of the origin, requiring there a higher number of secants to obtain a proper fitting with linear functions.

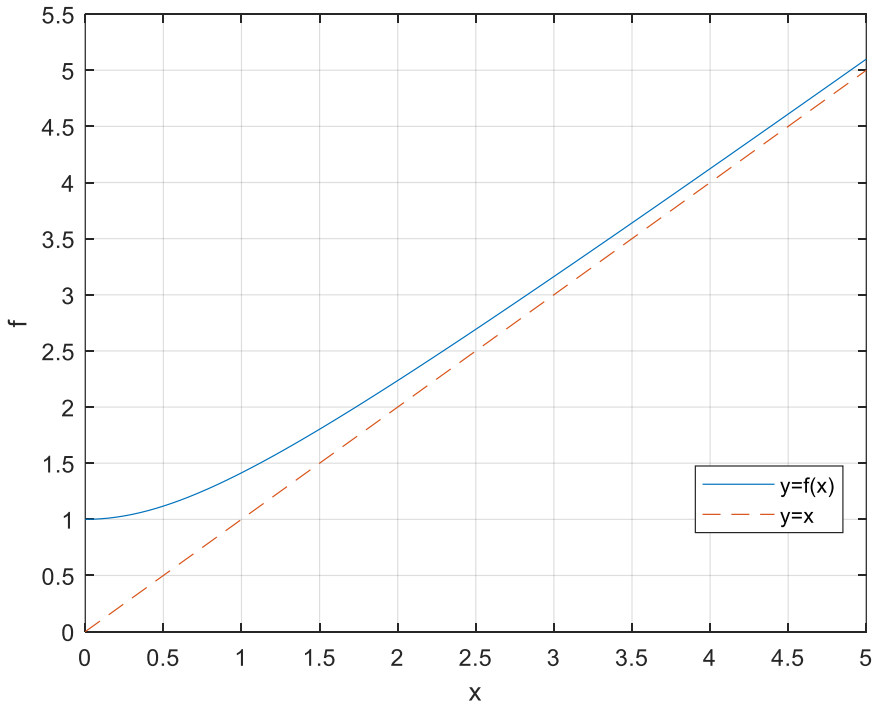


**Figure 41 Graph of the function *f***

To give further evidence to this concept, let us set $x_{\max} = \dfrac{H - z_{\min}}{r_{\min}} = 399.75$; the optimization procedure leads to the discretizing points plotted with the purple dots in Figure 42, which are not so different from the other ones, confirming the aforementioned considerations.

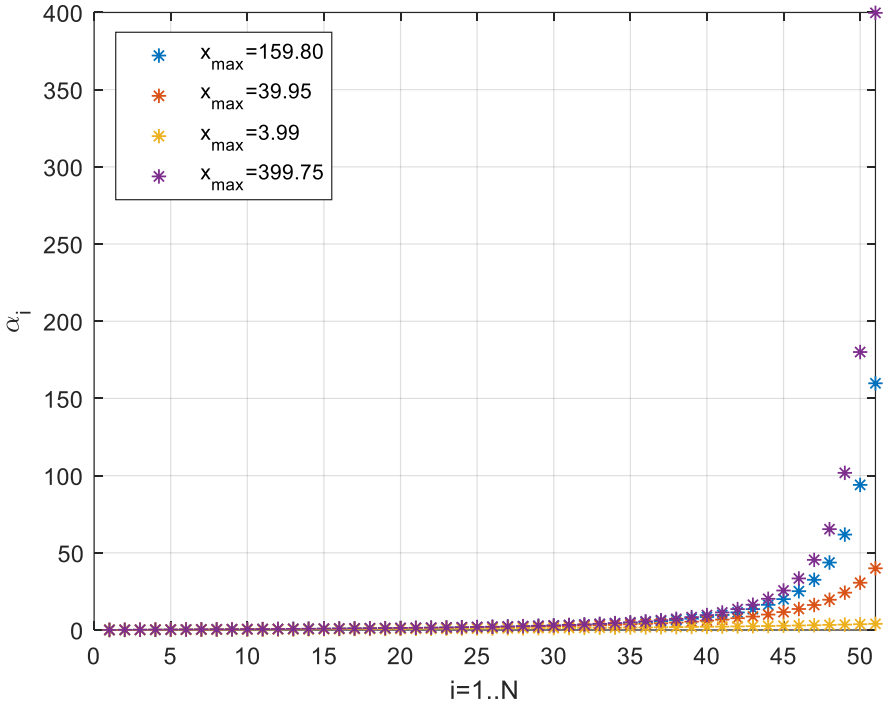


**Figure 42 Discretizing point for N=50 and different values of $x_{max}$**

Finally, the impact of $x_{max}$ on the fields is shown in Figure 43, which is relevant to Test T1-A considering *N=50* and the following two values:

$$x_{\max} = \begin{cases} \dfrac{H-z}{r} = 159.80 \\ \dfrac{H-z_{\min}}{r_{\min}} = 399.75 \end{cases} \tag{197}$$

As shown, this different choice does not affect at all the final solution.

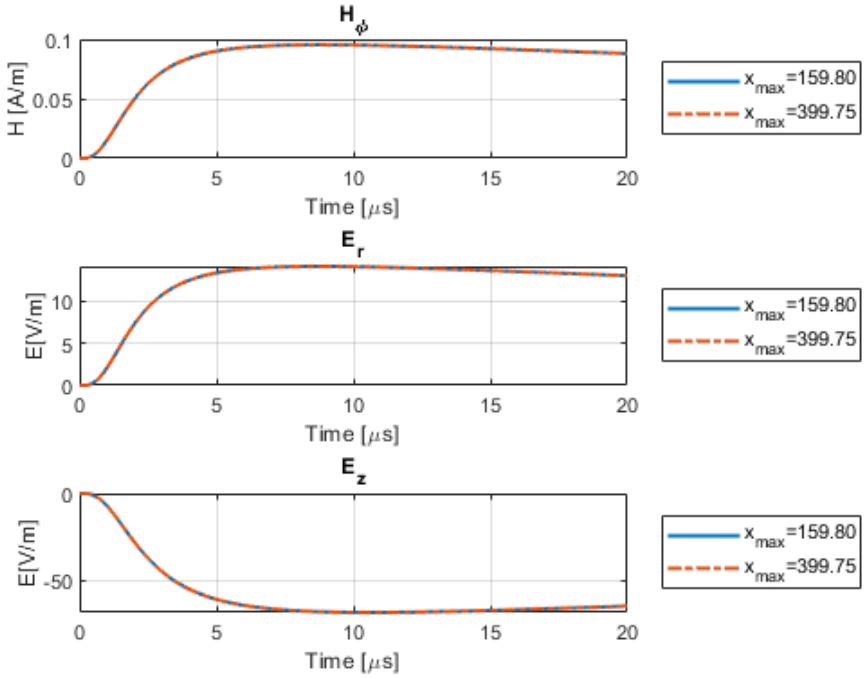


**Figure 43 Test T1-A Comparison with different values of $x_{max}$**

### 4.5.2 Computational effort of the proposed method

The computational effort is strictly related to the choice of *N*, because it represents the number of intervals in which the function *f* is discretized.

In the following, attention is focused on the influence of *N* on the computational effort and on the accuracy of the method.

For each field ($H_\varphi$, $E_r$, $E_z$) the deviation ($e_\psi$) between the proposed approach and the numerical integration is computed as follows:

$$\begin{aligned} E_\psi &= \max\left(\left|\psi_p(t)-\psi_n(t)\right|\right) \\ t_\psi^* &= t \;\Big|\; \max\left(\left|\psi_p(t)-\psi_n(t)\right|\right)=E_\psi \\ e_\psi &= 100\left|\frac{\psi_p\left(t_\psi^*\right)-\psi_n\left(t_\psi^*\right)}{\psi_n\left(t_\psi^*\right)}\right| \end{aligned} \tag{198}$$

where $\psi_{p(n)}$ is the generic field calculated with the proposed (numerical) approach.

The computational gain $G_\tau$ with respect to the numerical solution is computed as the ratio between the CPU time $\tau_{numerical}$ required by the numerical method and the time $\tau_{proposed}$ required by the proposed approach.

$$G_\tau = \frac{\tau_{numerical}}{\tau_{proposed}} \tag{199}$$

$G_\tau$ represents how fast the proposed approach is with respect to the numerical solution.

Let us consider Test T1-A and Test T4-A (these two cases have been chosen to account both for a perfect ground conductor and a finite conductivity). Table 15/Figure 44 and Table 16/Figure 45 express $e_\psi$ of each field and $G_\tau$ as a function of $N$. In the following, it has been chosen to decrease $N$ until one of the fields deviations overcomes 1%.

**Table 15 Fields deviation and computational effort gain as a function of N – Test T1-A**

| $N$ | $e_{Er}$ **[%]** | $e_{Ez}$ **[%]** | $e_{H\varphi}$ **[%]** | $G_\tau$ |
|---|---|---|---|---|
| 50 | 0.077748 | 0.085537 | 0.003387 | 2760 |
| 40 | 0.078207 | 0.134100 | 0.003913 | 3175 |
| 30 | 0.079566 | 0.229514 | 0.004975 | 4003 |
| 20 | 0.082886 | 0.451393 | 0.056404 | 5276 |
| 10 | 0.103967 | **1.220471** | 0.160328 | 9400 |

**Table 16 Fields deviation and computational effort gain as a function of N – Test T4-A**

| $N$ | $e_{Er}$ **[%]** | $e_{Ez}$ **[%]** | $e_{H\varphi}$ **[%]** | $G_\tau$ |
|---|---|---|---|---|
| 50 | 0.086965 | 0.085537 | 0.003387 | 211 |
| 40 | 0.087366 | 0.134100 | 0.003913 | 227 |
| 30 | 0.088601 | 0.229514 | 0.004975 | 241 |
| 20 | 0.094305 | 0.451393 | 0.056404 | 259 |
| 10 | 0.128086 | **1.220471** | 0.160328 | 277 |

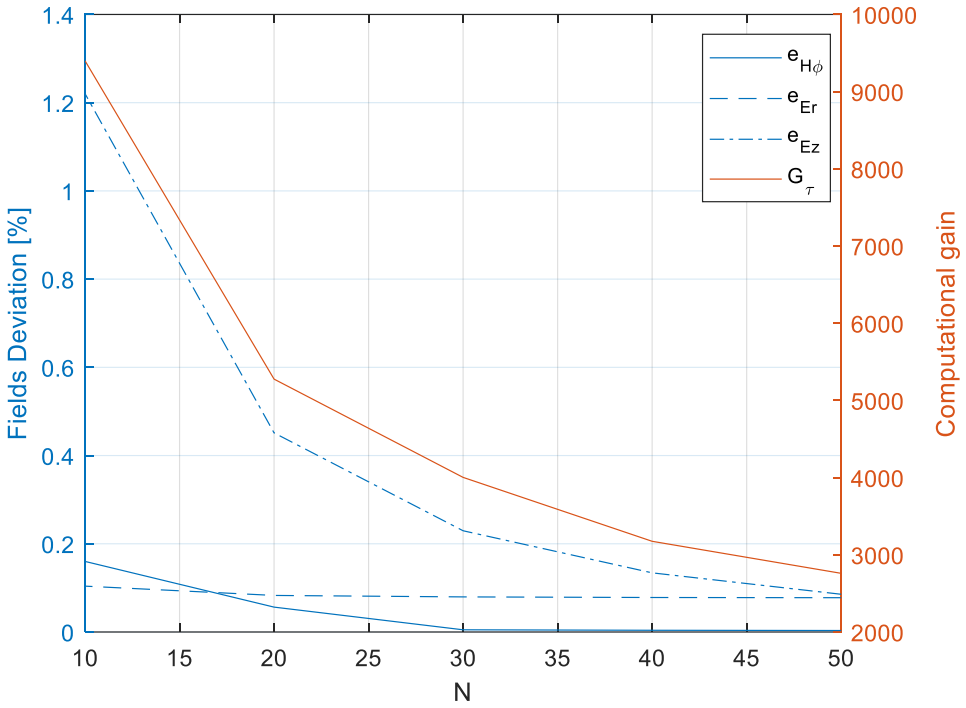


**Figure 44 Fields deviation and computational effort gain as a function of N – Test T1-A**

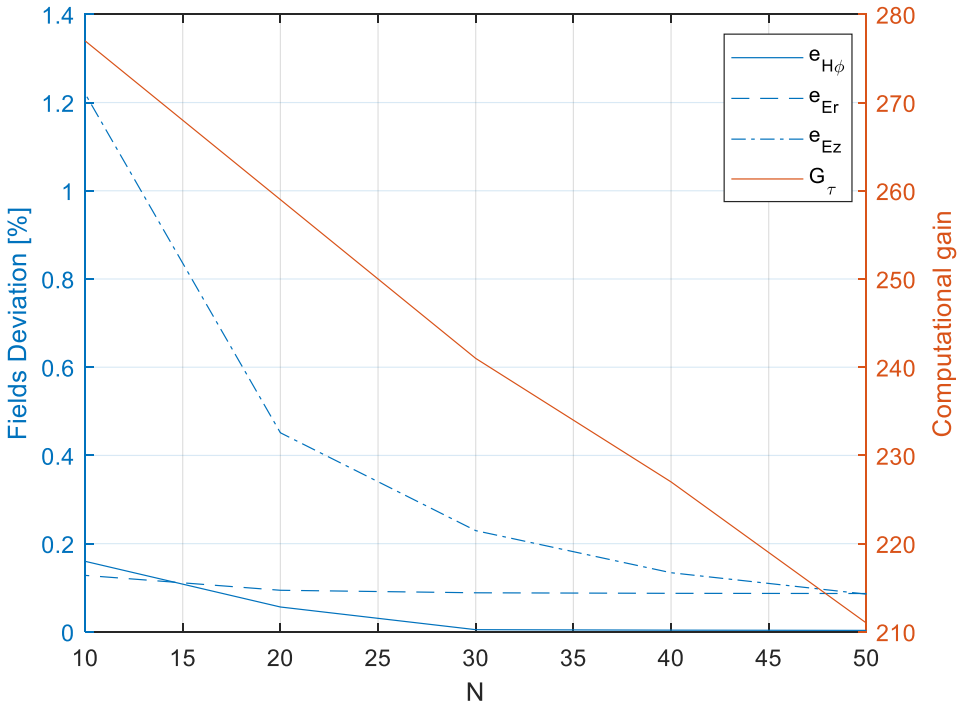


**Figure 45 Fields deviation and computational effort gain as a function of N – Test T4-A**

As can be noticed, *N* can be strongly reduced without causing a high increase in the deviation. Moreover, the last columns of Table 15 and Table 16 underline that even with high values of *N*

the computational time is reduced of more than 200 times, which represents a really impactful advantage of the proposed method. A stronger reduction of the computational time can be observed in case of perfect ground conductor.

In order to provide a comprehensive approach for the reader who wants to evaluate the electromagnetic fields with the approach proposed in this thesis, the discretizing points $\alpha_i$ and the coefficients $a_i$, $b_i$, necessary for the implementation of the proposed procedure, are here provided in Table 17 with $N$=30, which represents a good compromise between the fields deviations and the computational effort gain (note that $x_{max}$ is chosen as in sub-section 4.5.1).

**Table 17 Discretizing points $\alpha_i$ and coefficients $a_i$, $b_i$ with N=30**

| ***i*** | $\alpha_i$ | $a_i$ | $b_i$ |
|---|---|---|---|
| 1 | 0.0815 | 0.0407 | 1 |
| 2 | 0.1639 | 0.1217 | 0.9933 |
| 3 | 0.2479 | 0.2015 | 0.9803 |
| 4 | 0.3344 | 0.2793 | 0.9610 |
| 5 | 0.4245 | 0.3545 | 0.9358 |
| 6 | 0.5191 | 0.4263 | 0.9053 |
| 7 | 0.6196 | 0.4944 | 0.8700 |
| 8 | 0.7273 | 0.5582 | 0.8305 |
| 9 | 0.8440 | 0.6174 | 0.7874 |
| 10 | 0.9717 | 0.6717 | 0.7415 |
| 11 | 1.1129 | 0.7211 | 0.6935 |
| 12 | 1.2707 | 0.7656 | 0.6440 |
| 13 | 1.4490 | 0.8052 | 0.5937 |
| 14 | 1.6528 | 0.8400 | 0.5433 |
| 15 | 1.8884 | 0.8703 | 0.4932 |
| 16 | 2.1643 | 0.8964 | 0.4440 |
| 17 | 2.4918 | 0.9185 | 0.3961 |
| 18 | 2.8863 | 0.9370 | 0.3501 |
| 19 | 3.3690 | 0.9522 | 0.3061 |

| | | | |
|---|---|---|---|
| 20 | 3.9704 | 0.9646 | 0.2645 |
| 21 | 4.7350 | 0.9744 | 0.2255 |
| 22 | 5.7300 | 0.9820 | 0.1893 |
| 23 | 7.0614 | 0.9878 | 0.1561 |
| 24 | 8.9026 | 0.9921 | 0.1259 |
| 25 | 11.5559 | 0.9951 | 0.0989 |
| 26 | 15.5829 | 0.9972 | 0.0751 |
| 27 | 22.1294 | 0.9985 | 0.0545 |
| 28 | 33.8382 | 0.9993 | 0.0373 |
| 29 | 58.0277 | 0.9997 | 0.0233 |
| 30 = $N$ | 121.7485 | 0.9999 | 0.0127 |
| 31 = $N$+1 | 399.750 | 0.9999 | 0.0053 |

# 5 On the stability of FDTD-based numerical codes to evaluate lightning-induced overvoltages in overhead distribution lines

Section 2.3.2 has proposed the well-known scheme for the solution of the field-to-line coupling problem by the discretization in time and space domains. According to equation (106), the solution is achieved through a second-order FDTD scheme for the points inside the line and with a linear extrapolation at the extremities of the line (Eq. (107)).

We will show in what follows that the approach proposed in section 2.3.2 could exhibit numerical stability problems, even though the Courant condition (Eq.(103)) is satisfied (Section 5.1).

Later, in Section 5.2 a numerically stable algorithm based on the method of characteristics (briefly presented in Section 5.4) is presented and applied to a simplified case of a single conductor line and finally in Section 5.3 the extension of the proposed approach to a more realistic MTL system over a lossy ground is proposed and validated.

In the following the FDTD scheme of Section 2.3.2 is coupled with the external circuit provided by the software PSCAD-EMTDC.

## 5.1 The stability problem of the numerical field-to-line coupling codes

To highlight the stability problem, first a very simple geometry is considered that allows to evaluate voltages and currents at the line extremities also in a (semi-)analytical way [8]. As shown in Figure 46, a single-conductor line of length L=63m with diameter a=0.02 m lays over a perfectly conducting ground at a height h=10 m and is connected to ground with two equal resistances $R_0=R_L=10\ \Omega$ at its extremities.

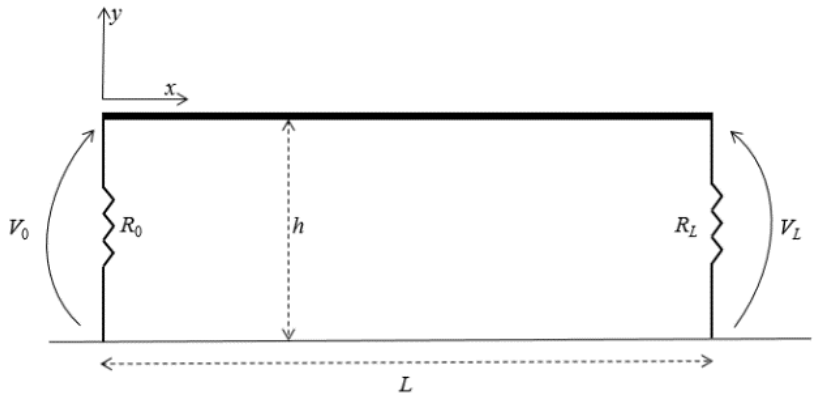


**Figure 46 Single conductor line**

The line is illuminated by an electromagnetic field due to a lightning discharge striking the ground 30 m from the middle of the line, i.e. $P_F$=(31.5, 30.0, 0.0). The lightning current propagation along the channel is described with the MTLE engineering model [15, 91] while the channel-base current is represented by a sum of two Heidler's functions [51].

The time step $\Delta t = 10ns$ and the spatial step $\Delta x = 9\text{m}$ have been set so that condition (103) is satisfied (with $C = 1/3$).

In Figure 47, the voltages at both extremities of the line are plotted as computed with the FDTD-PSCAD approach and via the characteristic method (see Section 5.4 for details); the exam of the figures highlights the unstable oscillations of the numerical approach, while the characteristic method appears to be stable.

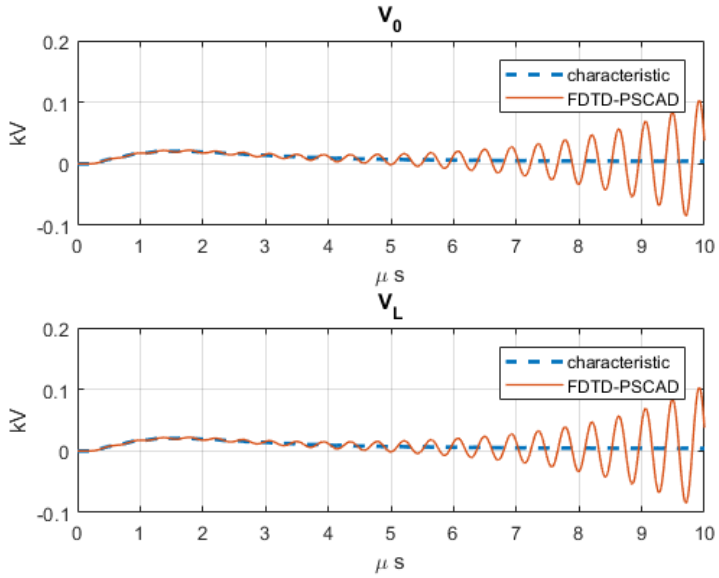


**Figure 47 Voltage at the beginning of the line ($V_0$) and at the end of the line ($V_L$) obtained with the FDTD-PSCAD approach (solid line) and via characteristic method (dashed line). Here $\Delta t = 10ns$ and $\Delta x = 9\text{m}$.**

Simulations have suggested that instability phenomena seem to be related to the ratio $L/\Delta x$; as a matter of fact, decreasing by ten times both the time and the space step ( $\Delta t = 1ns$ and $\Delta x = 0.9\text{m}$ ), it is possible to observe that analytical (method of characteristics) and numerical solutions are in perfect agreement (see Figure 48).

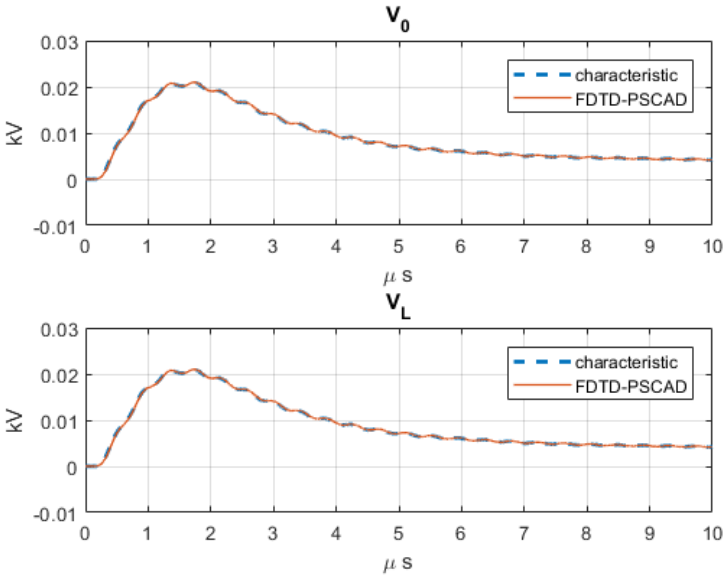


**Figure 48 Voltage at the beginning of the line (V0) and at the end of the line (VL) obtained by the FDTD-PSCAD approach (solid line) and via the method of characteristics (dashed line). Here $\Delta t = 1ns$ and $\Delta x = 0.9\text{m}$.**

A possible explanation of this behaviour lays in the fact that the ratio $L/\Delta x$ intrinsically influences the updating procedure (107) of the currents at the line extremities: the smaller is the

spatial step, the more accurate is (107). To confirm this hypothesis, Figure 49 plots the numerical solution of the problem with time step $\Delta t = 10ns$ and the spatial step $\Delta x = 9\text{m}$ but with analytical imposition of the boundary conditions (i.e., $V_1^n = -R_0 I_1^n$ and $V_{K_m}^n = R_L I_{K_m}^n$). In this case, substantially, the characteristic method, which requires the knowledge of the voltage-current law at the extremities, is used in order to evaluate the current at the extremities which are then passed, for each time step, to the coupling code instead of those calculated with the extrapolation. The perfect agreement with the analytical solution allows to state that the numerical instability problem occurs when (107) is used to update the currents at the line extremities and the ratio $L/\Delta x$ is not sufficiently small.

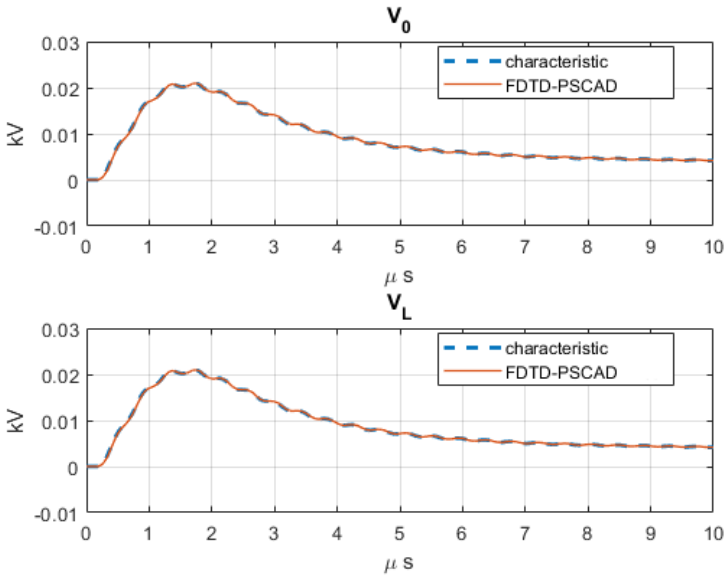


**Figure 49 Voltage at the beginning of the line (V0) and at the end of the line (VL) obtained by the FDTD-PSCAD approach (solid line) with analytical imposition of boundary conditions, and via characteristic method (dashed line). Here $\Delta t = 10ns$ and $\Delta x = 9\text{m}$ .**

The presented analysis suggests that, whenever it is not possible to impose boundary conditions in analytical way, a very small time and space has to be used in order to make the extrapolation (107) effective. However, this might require too high computational effort.

## 5.2 Proposed solution for a single conductor line

As the numerical instability problem depends mostly on the use of extrapolation (107) when the space step is not sufficiently small with respect to the line length *L*, it is necessary to use another method to update the currents in the first and in the last point of the line (and in all the eventual discontinuities). The approach proposed in the present thesis provides the current updating applying the characteristics method [8] in the first and in the last line segments.

The main requirement is that there exists an integer $N_T$ s.t.

$$N_T \Delta t = \frac{\Delta x}{c_0} \tag{200}$$

In this way the travel time T defined in (213) is an integer multiple of the time step, so that applying (211) and (212) one gets

$$V_{K_m}^{\text{ext},n+1} + Z_C I_{K_m}^{n+1} = \left[ V_{K_m-1}^{n+1-N_T} + Z_C I_{K_m-1}^{n+1-N_T} \right] \cdot \cdot 1(n+1-N_T) + \Theta_{K_m-1,K_m;0}^{fw}(t_{n+1}) \tag{201}$$

$$V_1^{\text{ext},n+1} - Z_C I_1^{n+1} = \left[ V_2^{n+1-N_T} - Z_C I_2^{n+1-N_T} \right] \cdot \cdot 1(n+1-N_T) + \Theta_{1,2;0}^{bw}(t_{n+1}) \tag{202}$$

As can be seen from (201)-(202), the method of characteristics basically defines two Thévenin equivalents of the analyzed line at its extremities. So, in order to know the voltage/current at such extremities, the functional relationship between them as dictated by the external circuit should be known, which is not possible when dealing with a numerical electromagnetic simulator. To solve this problem, one can suppose that

$$V_1^{\text{ext},n+1} \approx V_1^{\text{ext},n} \quad \text{and} \quad V_{K_m}^{\text{ext},n+1} \approx V_{K_m}^{\text{ext},n} \tag{203}$$

Inserting (203) into (201)-(202), it is possible to write the following updating relations for currents

$$I_{K_m}^{n+1} = \frac{1}{Z_C} \left\{ -V_{K_m}^{\text{ext},n} + \left[ V_{K_m-1}^{n+1-N_T} + Z_C I_{K_m-1}^{n+1-N_T} \right] \cdot \cdot 1(n+1-N_T) + \Theta_{K_m-1,K_m;0}^{fw}(t_{n+1}) \right\} \tag{204}$$

$$I_1^{n+1} = \frac{-1}{Z_C} \left\{ -V_1^{\text{ext},n} + \left[ V_2^{n+1-N_T} - Z_C I_2^{n+1-N_T} \right] \cdot \cdot 1(n+1-N_T) + \Theta_{1,2;0}^{bw}(t_{n+1}) \right\} \tag{205}$$

If one updates the currents with (204)-(205) instead of (107), even with $\Delta t = 10ns$ and $\Delta x = 9\text{m}$, a perfect agreement between the proposed approach (labeled as FDTD-PSCAD (new) in the following) and the analytical solution is obtained for the case presented in Section 5.1 (see Figure 50).

The reason why this approach is more effective than the previous one probably lies in the fact that the only condition to be satisfied is that the voltage does not change much from one time step to the subsequent one in order to make (203) hold. This hypothesis is typically satisfied with time steps normally adopted in these studies (about 10 ns necessary to correctly reproduce the waveform of the lightning electromagnetic fields).

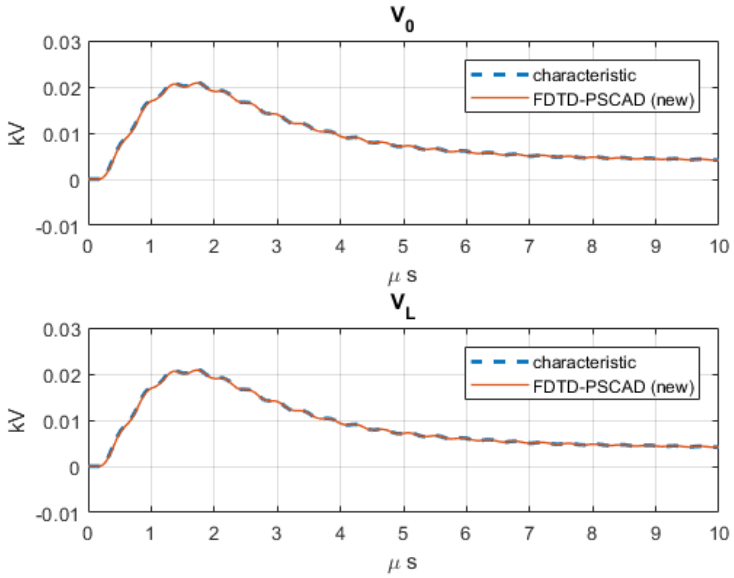


**Figure 50 Voltage at the beginning of the line ($V_0$) and at the end of the line ($V_L$) obtained by the FDTD-PSCAD (new) approach (solid line) and via characteristic method (dashed line). Here $\Delta t = 10ns$ and $\Delta x = 9\text{m}$**

## 5.3 Generalization to a MTL over a conducting ground and discontinuities along the line

Although the method of characteristics is applicable only to a single conductor line over a perfectly conducting ground, one can assume that the proposed strategy (201)-(202) for updating currents is still valid also for a MTL system over a lossy ground. This hypothesis basically neglects the effect of: i) the line ohmic, ii) the finite ground conductivity in the coupling equations and iii) the inductive coupling among conductors. Notwithstanding the above, the hypothesis can be considered as reasonable since it applies only to a small portion of the whole system.

Starting from this assumption, the generalization of (201)-(202) is very simple: for the *i*-th conductor one has:

$$I_{i,K_m}^{n+1} = \frac{1}{Z_{C,i}}\left\{-V_{i,K_m}^{\text{ext},n} + \left[V_{i,K_m-1}^{n+1-N_T} + Z_{C,i} I_{i,K_m-1}^{n+1-N_T}\right]\cdot \cdot 1(n+1-N_T) + \Theta_{K_m-1,K_m;y_i}^{fw}(t_{n+1})\right\} \tag{206}$$

$$I_{i,1}^{n+1} = \frac{-1}{Z_{C,i}}\left\{-V_{i,1}^{\text{ext},n} + \left[V_{i,2}^{n+1-N_T} - Z_{C,i} I_{i,2}^{n+1-N_T}\right]\cdot \cdot 1(n+1-N_T) + \Theta_{1,2;y_i}^{bw}(t_{n+1})\right\} \tag{207}$$

$Z_{C,i}$ being the characteristic impedance of the *i*-th conductor, evaluated for the case of a lossless wire.

In the case of discontinuities (i.e., points connected to the ground by means of suitable devices like arresters or line junctions), the same procedure can be adopted, treating each of these discontinuity points in the same way as the terminations. Following [34], if one indicates with $x_d$ the abscissa of the generic discontinuity point ($d=1..D$) and defines the corresponding index $k_d = x_d / \Delta x + 1$, it is possible to evaluate the left and right limits $I_{i,k_d}^{-,n+1}$ and $I_{i,k_d}^{+,n+1}$ of the current for $x$ approaching $x_d$ by means of (206) and (207). More precisely,

$$I_{i,k_d}^{-,n+1} = \frac{1}{Z_{C,i}} \left\{ -V_{i,k_d}^{\text{ext},n} + \left[ V_{i,k_d-1}^{n+1-N_T} + Z_{C,i} I_{i,k_d-1}^{n+1-N_T} \right] \cdot \right. \\ \left. \cdot 1(n+1-N_T) + \Theta_{k_d-1,k_d;y_i}^{fw}(t_{n+1}) \right\} \tag{208}$$

$$I_{i,k_d}^{+,n+1} = \frac{-1}{Z_{C,i}} \left\{ -V_{i,k_d}^{\text{ext},n} + \left[ V_{i,k_d+1}^{n+1-N_T} - Z_{C,i} I_{i,k_d+1}^{n+1-N_T} \right] \cdot \right. \\ \left. \cdot 1(n+1-N_T) + \Theta_{k_d,k_d+1;y_i}^{bw}(t_{n+1}) \right\} \tag{209}$$

Then, the KCL allows to find out the update of the current flowing in the device connected to the line in the point $x_d$ as:

$$I_{i,k_d}^{n+1} = I_{i,k_d}^{-,n+1} - I_{i,k_d}^{+,n+1} \tag{210}$$

The validation of the proposed approach has been performed on a realistic Italian distribution network MTL (see Figure 12) consisting of 3 conductors of length $L$=189m, whose details are summarized in Table 18.

**Table 18 Geometry of the MTL system**

| | *Cond. 1* | *Cond. 2* | *Cond. 3* |
|---|---|---|---|
| height from ground | 8.0 m | 8.0 m | 8.6 m |
| distance from *y* axis | −1.2 m | 1.2 m | 0.0 m |
| conductor diameter | 0.64 cm | 0.64 cm | 0.64 cm |

A lossy ($\sigma_g$=0.005 S/m) ground has been considered with a relative dielectric constant equal to 10. Regarding the terminations, two cases are presented: 1) each conductor is terminated at both ends with a 10 Ω resistor and connected to ground every 63 m with a 20 Ω resistor, and 2) each conductor is connected to ground every 63 m through a typical 10 kV surge arrester [92] (Figure 51 shows its V-I characteristic), so that the line has four surge arresters: two at the terminations and two at the discontinuities

Such MTL is illuminated by an electromagnetic field due to a lightning return stroke that occurs 30m far from the middle of the line, i.e. $P_F$=(94.5, 30.0, 0.0) with the current distribution modeled as in the previous section.

For the numerical simulation of the FDTD-PSCAD (new) approach, again $\Delta t = 10ns$ and $\Delta x = 9\text{m}$ have been considered.

In order to test its performances, the FDTD-PSCAD with extrapolation presented in [34] has been used with $\Delta t = 1ns$ and $\Delta x = 0.9\text{m}$ for guaranteeing stable results, as proved at the beginning of this contribution in Figure 48.

Figure 52 and Figure 53 present the voltages in four points on the first half of the line for cases 1) and 2), respectively. Note that the symmetry of the considered geometry allows to state that the other half line exhibits the same behaviour. For both cases, a perfect agreement between the benchmark and the new approach can be observed, with a meaningful reduction in the computational effort. In particular, a simulation performed with the time and spatial steps here presented (i.e. 10 ns and 9 m) requires about 1/8 of the time required by a simulation performed with a time step of 1 ns and a spatial step of 1 m.

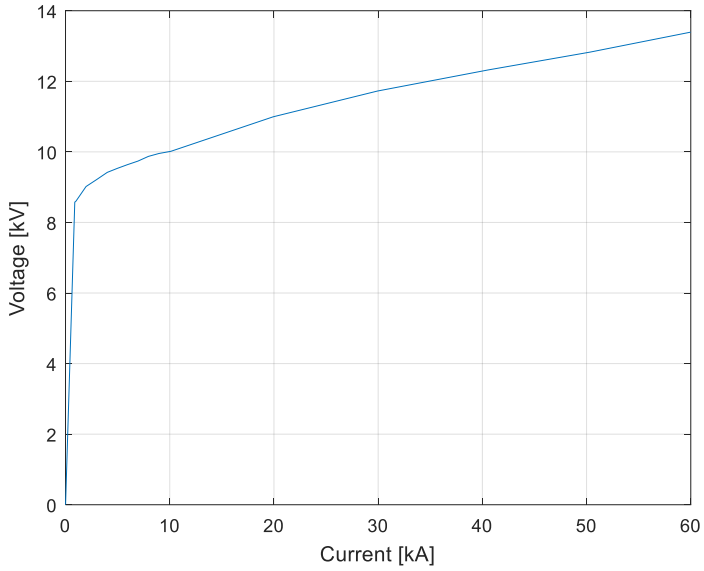


**Figure 51 Surge arrester V-I characteristic**

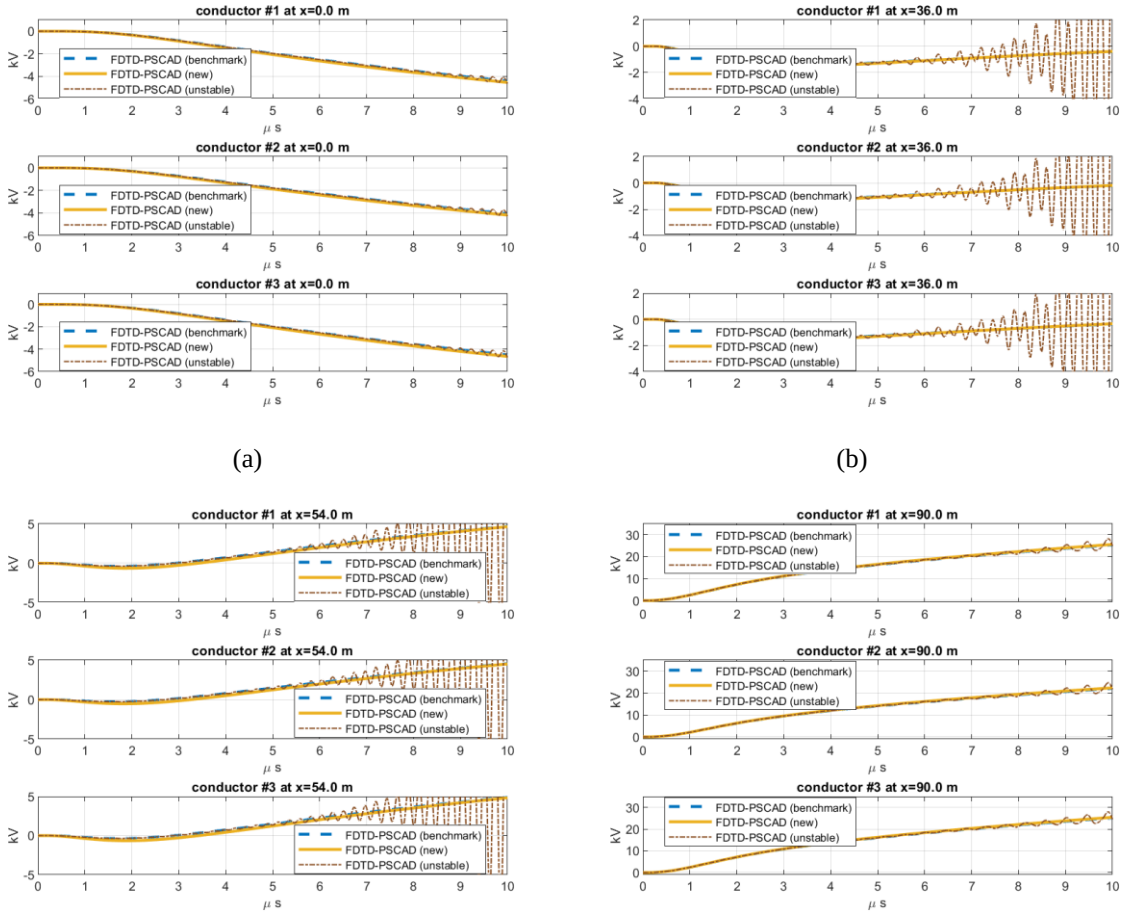


**Figure 52 Case 1) Voltages for the three conductors at the distances of: 0m (a), 36m (b), 54m (c) and 90m (d) from the beginning of the line. The solid lines are obtained by using the FDTD-PSCAD (new) approach with $\Delta t = 10ns$ & $\Delta x = 9\text{m}$ . The FDTD-PSCAD (unstable) plot (dash-dotted lines) and the FDTD-PSCAD (benchmark) one (dashed lines) have been both obtained using the FDTD-PSCAD approach with $\Delta t = 10ns$ & $\Delta x = 9\text{m}$ and $\Delta t = 1ns$ & $\Delta x = 0.9\text{ m}$ respectively.**

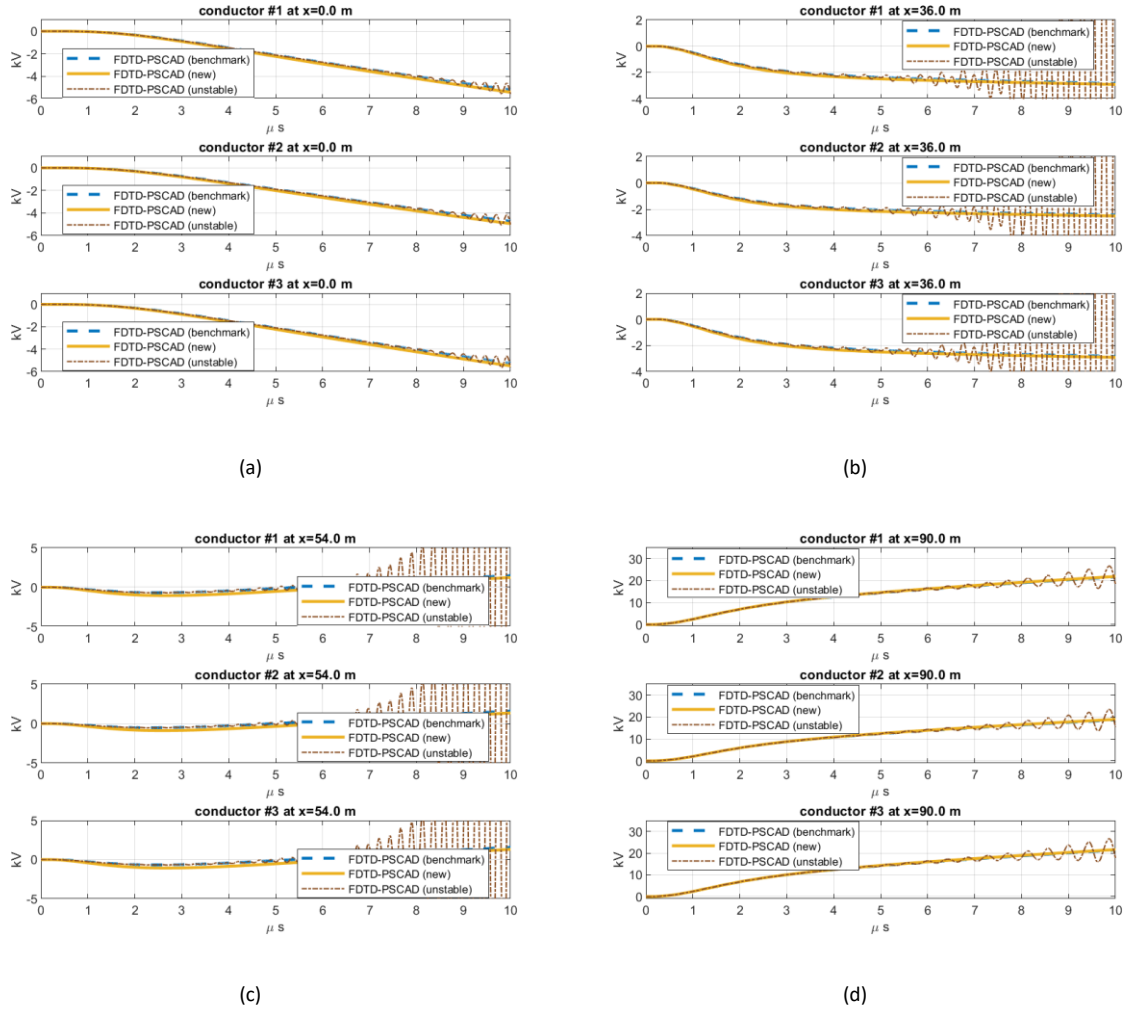


**Figure 53 Case 2) Voltages for the three conductors at the distances of: 0m (a), 36m (b), 54m (c) and 90m (d) from the beginning of the line. The solid lines are obtained by using the FDTD-PSCAD (new) approach with $\Delta t = 10ns$ & $\Delta x = 9\text{m}$ . The FDTD-PSCAD (unstable) plot (dash-dotted lines) and the FDTD-PSCAD (benchmark) one (dashed lines) have been both obtained using the FDTD-PSCAD approach with $\Delta t = 10ns$ & $\Delta x = 9\text{m}$ and $\Delta t = 1ns$ & $\Delta x = 0.9\text{ m}$ respectively.**

## 5.4 Appendix - the method of characteristics

Let us consider a single conductor line of extremities *A* and *B* and length $L_{AB}$ which lays over a perfectly conducting ground at height *h* and at distance *y* from the reference system. The method of characteristics [8] states that the voltages $V(\cdot,t)$ and the currents $I(\cdot,t)$ at the line extremities are related by:

$$V(B,t)+Z_C I(B,t)=\left[V(A,t-T)+ +Z_C I(A,t-T)\right]1(t-T)+\Theta^{fw}_{A,B;y}(t) \tag{211}$$

$$V(A,t)-Z_C I(A,t)=\left[V(B,t-T)+ -Z_C I(B,t-T)\right]1(t-T)+\Theta^{bw}_{A,B;y}(t) \tag{212}$$

where $z_C$ is the characteristic impedance of the line [8], $T$ is the travel time defined as:

$$T = \frac{L_{AB}}{c_0} \tag{213}$$

and finally, as usual, $1(t)$ is the Heaviside function, i.e.

$$1(t) = \begin{cases} 1 & t > 0 \\ 0 & \text{otherwise} \end{cases} \tag{214}$$

The quantities $\Theta^{fw}_{A,B;y}$ and $\Theta^{bw}_{A,B;y}$ are completely defined by the incident electric field according to the following

$$\Theta^{fw}_{A,B;y}(t) = \mathscr{E}_T(A, t-T) - \mathscr{E}_T(B,t) + \int_0^{L_{AB}} \mathscr{E}_{L,y}\left(x, t-T+\frac{x}{c_0}\right)dx \tag{215}$$

$$\Theta^{bw}_{A,B;y}(t) = \mathscr{E}_T(B, t-T) - \mathscr{E}_T(A,t) - \int_0^{L_{AB}} \mathscr{E}_{L,y}\left(x, t-\frac{x}{c_0}\right)dx \tag{216}$$

where

$$\mathscr{E}_{T,y}(x,t) \approx hE^e_z(r(x,y),t)1(t) \tag{217}$$

and $\mathscr{E}_{L,y}$ is the projection onto the line of the radial component of the electric field, i.e.

$$\mathscr{E}_{L,y}(x,t) = E_r(r(x,y),t)\frac{x-x_F}{r(x,y)}1(t) \tag{218}$$

The presence of the function $1(t)$ accounts for the fact that the lightning is supposed to strike at t=0. The function $r(x,y) = \sqrt{(x-x_F)^2 + (y-y_F)^2}$ is the distance of the generic point $(x,y)$ belonging to the line from the lightning impact point $P_F=(x_F,y_F,0)$. Notice that for a single conductor the x-axis of the reference system typically coincides with the line, so that $y=0$. The presence of the distance $y$ is important for the generalization to a MTL system.

# 6 An approximate formula for the evaluation of the lightning-induced overvoltages distribution on overhead distribution lines applicable to lightning performance procedure

When we deal with lightning-induced overvoltages on distribution lines the most impactful analysis is no-doubt the lightning performance [1, 32, 33, 35, 37]. Being the maximum lightning-induced overvoltage a function of the return stroke current peak, front time, engineering model, point of impact and velocity, if one wants to evaluate the lightning performance of a distribution line, he has to [35, 51]: i) generate a large number of lightning events, each one characterized by a peak current, a point of impact, a front time and a return stroke velocity extracted according to their probability density functions. The return stroke model is usually chosen from one of the EM deeply studied in literature [2]; ii) Compute the maximum lightning-induced overvoltage occurred on the considered line associated to each event; iii) Compare the maximum overvoltage with the line Critical Flashover (CFO); iv) Compute the ratio between the number of events that exceed the CFO and the total number of events and v) Multiply the value obtained for the Ground Flash Density. This procedure would imply a high computational effort.

In order to simplify it, it is well-known that the return stroke velocity does not significantly affect the maximum lightning-induced overvoltages [51, 93], thus it can be neglected in the lightning performance procedure. However, even with this assumption, the computational effort is still high, in particular because the return stroke front time affects the computation of electromagnetic fields, which is no-doubt the heaviest part.

In order to reduce the computational effort, the lightning performance computation can be evaluated through the use of some analytical formulas [1],[77, 78] or with the use of the methodologies proposed in [33, 35] for the evaluation of the maximum induced voltage. The advantages of the analytical methods rely on the low computational effort but they are valid only with some assumptions, such as the presence of only one infinite line. On the other hand, the methodologies proposed in [33, 35] are able to account for complex line topology, but still have a high computational effort.

In this section the author proposes a methodology for the evaluation of the maximum lightning-induced overvoltage suited for the lightning performance computation, based on a few number of field-to-line coupling simulations. With respect to the analytical methods, it takes into account all the selected variables (peak current, front time and stroke location) and is able to evaluate the results also in presence of a non-infinite line. On the other hand, the computational

effort is extremely reduced with respect to [33, 35]. Moreover, being based on the coupling code presented in [34] (and in principle it can be applied to any numerical method), it can consider any input current and any connections type at the line terminals and discontinuities.

Section 6.1 presents the preliminary analysis aimed at getting some insight on the functional relationship between stroke location, current peak and front duration and the system overvoltage. Section 6.2 describes the proposed methodology, Section 6.3 is devoted to the validation.

## 6.1 Preliminary analysis

The main aim of the chapter is to obtain an approximate formula linking lightning striking point ($x_F$, $y_F$), current peak ($I$) and front time ($\tau_d$) with the maximum induced overvoltage ($V$) experienced by a power (distribution) system.

This is done postulating a functional relationship among such quantities and then performing a (reduced) number of simulations to determine the numerical values of the involved parameters. To do this, one should first get a physical insight on how the system maximum overvoltage depends on the aforementioned parameters. The present section aims at reaching this goal considering one variable at a time.

Let us consider a 15 kV single conductor line of length $L$=1 km, diameter $d$=0.64 cm, connected at both extremities to two surge arresters (with V-I characteristic of [92]) and lying at height $h$=8 m over a ground with a conductivity $\sigma$= 1 mS/m and relative permittivity $\varepsilon_r$=10.

Introducing a Cartesian coordinate system such that the line ends are points (0,0,$h$) and ($L$,0,$h$), then $y_F$ basically measures the distance between the line and the lightning channel. The well-known Rusck's formula states that the overvoltage peak is proportional to the inverse of such distance; so, once fixed $x_F$, $I$ and $\tau_d$, let's try to use a quadratic fitting in the variable $1/y_F$, i.e.

$$V = a_{y,0} + a_{y,1}\left(\frac{1}{y_F}\right) + a_{y,2}\left(\frac{1}{y_F}\right)^2 \tag{219}$$

where $a_{y,i}$ ($i$=0,1,2) are suitable coefficients to be fixed. To verify this, simulations have been performed with the code described in [34] and presented in Figure 54 (blue stars).

For this test we supposed $I$=30 kA, $\tau_d$=5.5 μs (corresponding to the median values of Berger's distribution for first strokes), three horizontal positions $x_F$=–500 m (outside the line), $x_F$=0 m (left end of the line) and $x_F$=500 m (middle point of the line) with ten values of $y_F$ in the range [50m, 1000m]. Applying a fitting procedure to function (219), the red lines reveal an excellent agreement with complete simulation results for point $x_F$=0 and $x_F$=500 m, while some deviations occur if the lightning strikes outside the line. Repeating the analysis with $I$=12 kA

and $\tau_d$=1.1 μs (median values of subsequent strokes of Berger's distributions), one gets similar results (Figure 55). This confirms the initial guess to consider a second order polynomial expression in the variable $1/y_F$ could be employed to derive the final formula.

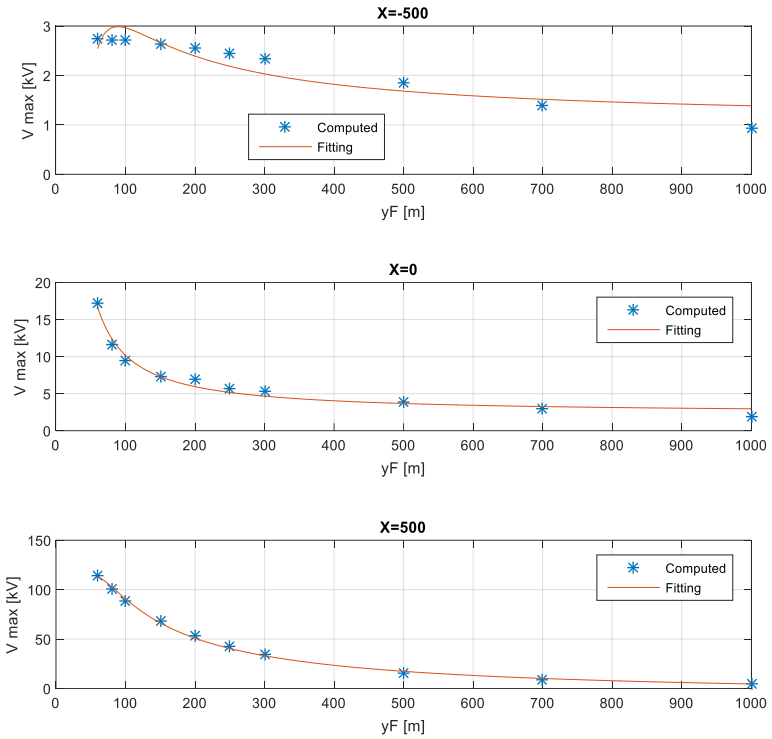


**Figure 54 First stroke – $y_F$ influence**

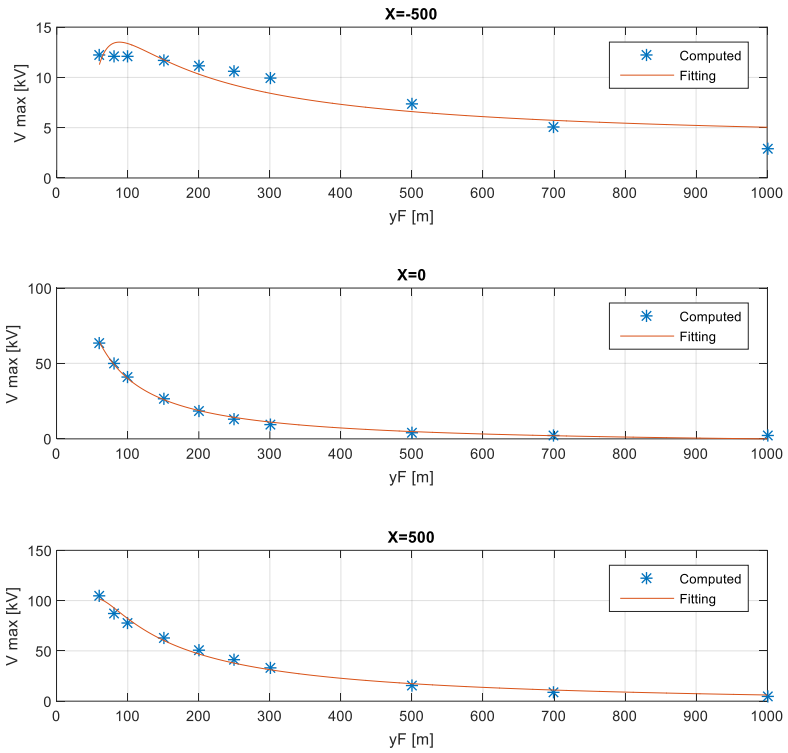


**Figure 55 Subsequent stroke – $y_F$ influence**

Moreover, the Rusck's formula states that the overvoltage is proportional to the current. However, to account saturation behavior introduced by non-linear devices, one can suppose that, at fixed $x_F$, $y_F$ and $\tau_d$, the overvoltage appears again as a quadratic polynomial in the variable $\sqrt{I}$ , i.e

$$V = a_{I,0} + a_{I,1}\sqrt{I} + a_{I,2}\left(\sqrt{I}\right)^2 \tag{220}$$

where $a_{I,i}$ (i=0,1,2) are suitable parameters to be fixed. Assessment of relationship (220) can be done again with simulation supposing $\tau_d$=5.5 μs (first stroke), four stroke positions characterized by the following coordinates ([500m, 60m], [0m, 60m], [0m, 300m], [500m, 300m]) and six values of current in the range (5-30 kA) obtaining the blue stars of Figure 56. The fitting algorithm produces the red curves that are always in excellent agreement with the simulation assessing the possibility of considering a relationship of the kind (220). Repeating the analysis for $\tau_d$=1.1 μs (subsequent stroke) one can draw the same conclusions (Figure 57).

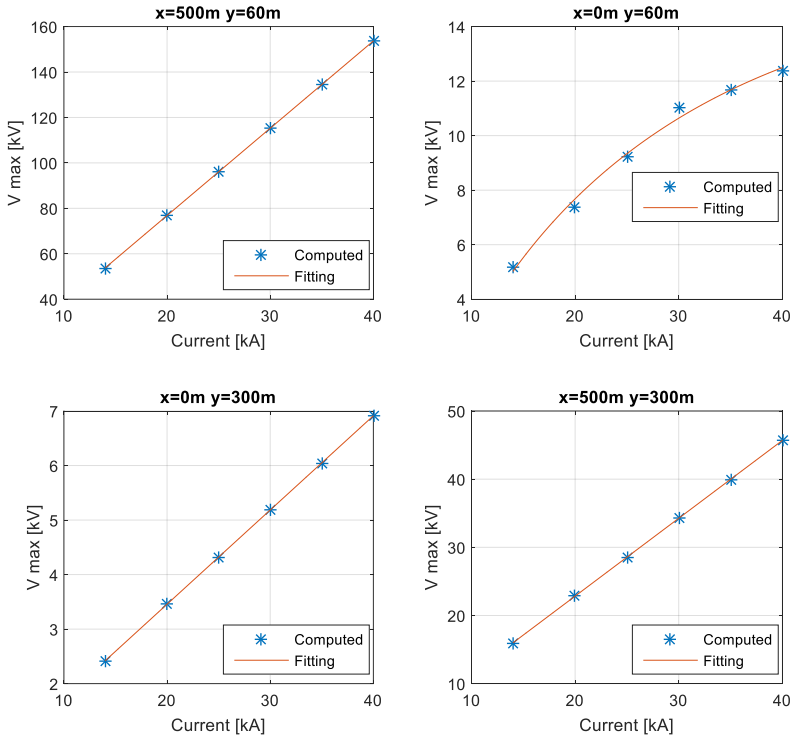


**Figure 56 First stroke - *I* influence**

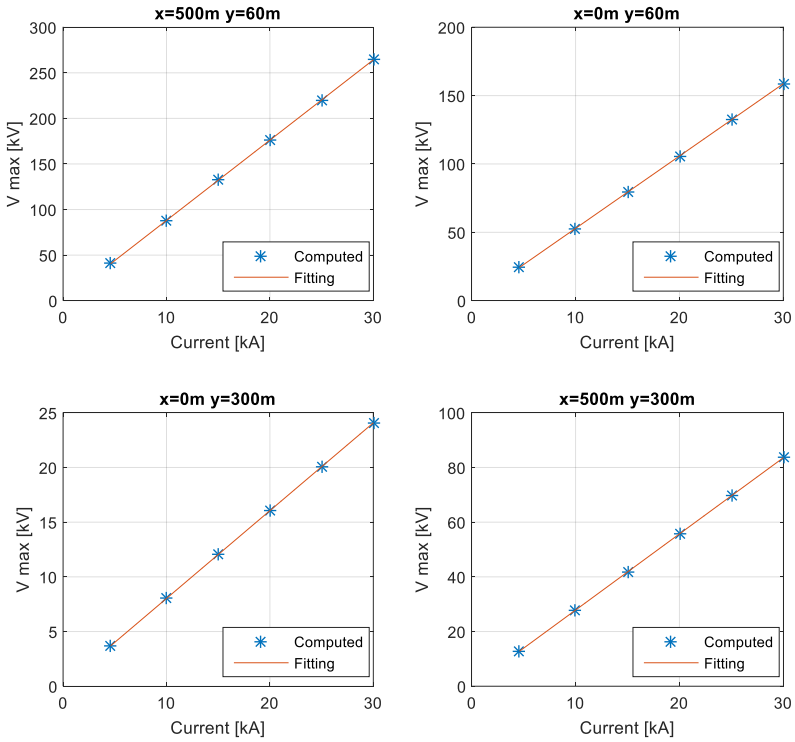


**Figure 57 Subsequent stroke – *I* influence**

The dependence on the front time is a bit more complicated, first of all because no simplified formulas to rely on are at disposal. Similarly to the previous analysis, once fixed $I$, $x_F$ and $y_F$, a

different behavior for first and second stroke current has been observed. More precisely, considering the same striking points as before a quadratic behaviour

$$V = a_{\tau_{d1},0} + a_{\tau_{d1},1}\tau_d + a_{\tau_{d1},2}\left(\tau_d\right)^2 \tag{221}$$

in the variable $\tau_d$ of the overvoltage seems to be a good choice as shown in Figure 58, for first stroke currents characterized $\tau_d \in [1.1\,\mu s, 18\mu s]$. On the contrary, a quadratic behavior

$$V = a_{\tau_{d2},0} + a_{\tau_{d2},1}\frac{1}{\tau_d} + a_{\tau_{d2},2}\left(\frac{1}{\tau_d}\right)^2 \tag{222}$$

on the variable $1/\tau_d$ seems to be optimal, as shown in Figure 59 for describing second stroke currents characterized by $\tau_d \in [0.22\,\mu s, 4.5\mu s]$.

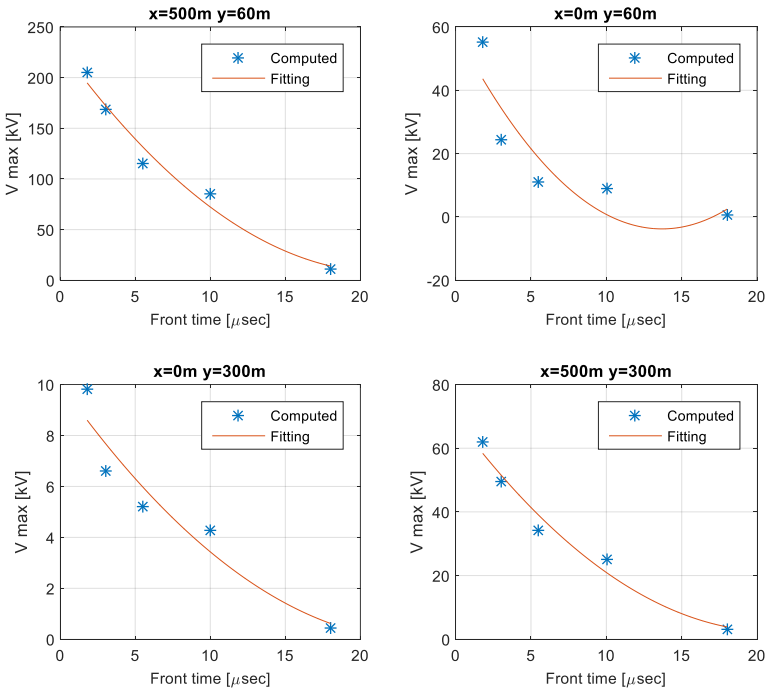


**Figure 58 First stroke – $\tau_d$ influence**

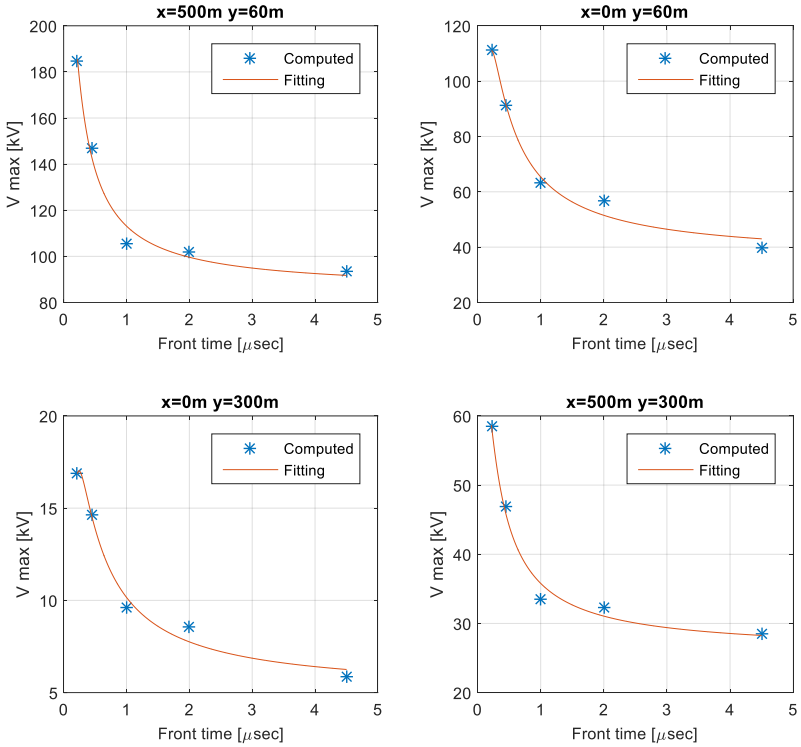


**Figure 59 Subsequent stroke – $\tau_d$ influence**

Finally, as concern the lightning horizontal position $x_F$ overvoltage dependence, a more complex scenario appears, for example, due to the line ends and/or discontinuities inside the line. For this reason, a different approach has been adopted, which will be described in the next section.

As a conclusion, one can guess that, for fixed $x_F$, the overvoltage peak could be described with a second order polynomial in the variables $\frac{1}{y_F}, \tau_d, \sqrt{I}$ for the first stroke and $\frac{1}{y_F}, \frac{1}{\tau_d}, \sqrt{I}$ for the subsequent one.

## 6.2 Derivation of the approximate formula

The aim of the present section is to describe the approximate formula that links the lightning strike point and current parameters to the system overvoltage. This has been done in two steps: the first the method to describe such formula for fixed $x_F$ has been presented (subsection 6.2.1), and then the dependence on the lightning horizontal position $x_F$ has been analyzed in subsection 6.2.2.

### *6.2.1* Approximate function at assigned $x_f$

The preliminary analysis conducted in the previous section allows to postulate, for an assigned $x_F = \bar{x}_F$, a formula of the kind

$$V\left(\bar{x}_F, y_F, I, \tau_d\right) = c_0 + c_1\sqrt{I} + c_2\tau_d^k + \\ + \frac{c_3}{y_F} + c_{11}I + c_{22}\tau_d^{2k} + \frac{c_{33}}{y_F^2} + c_{12}I\tau_d^k + \\ + c_{13}\frac{I}{y_F} + c_{23}\frac{\tau_d^k}{y_F} \tag{223}$$

with $k$=1 for first stroke and $k$=−1 for subsequent stroke.

Such formula should be valued in a specific domain $D = \left[\tau_{d,\min}, \tau_{d,\max}\right] \times \left[y_{F,\min}, y_{F,\max}\right] \times \left[I_{\min}, I_{\max}\right]$.

Upper and lower bounds for peak current and front time can be evaluated according to their classical distribution (e.g 5$^{th}$ percentile and 95$^{th}$ percentile of Berger's distributions for first and subsequent strokes). Maximum and minimum distances can be evaluated as proposed in [35]. However, two considerations can be done on the domain of interest of (223).

1. The Electro-Geometric Model (EGM) or any other attachment model establishes a relationship between distance and peak current of the kind $f\left(y_F, I\right) = 0$. Such function defines a surface that divides *D* in two zones: one (*D1*) in which only direct strikes occur and the other (*D2*) characterized by indirect strikes (Figure 60). Of course, the evaluation of (223) is of interest only in *D2*

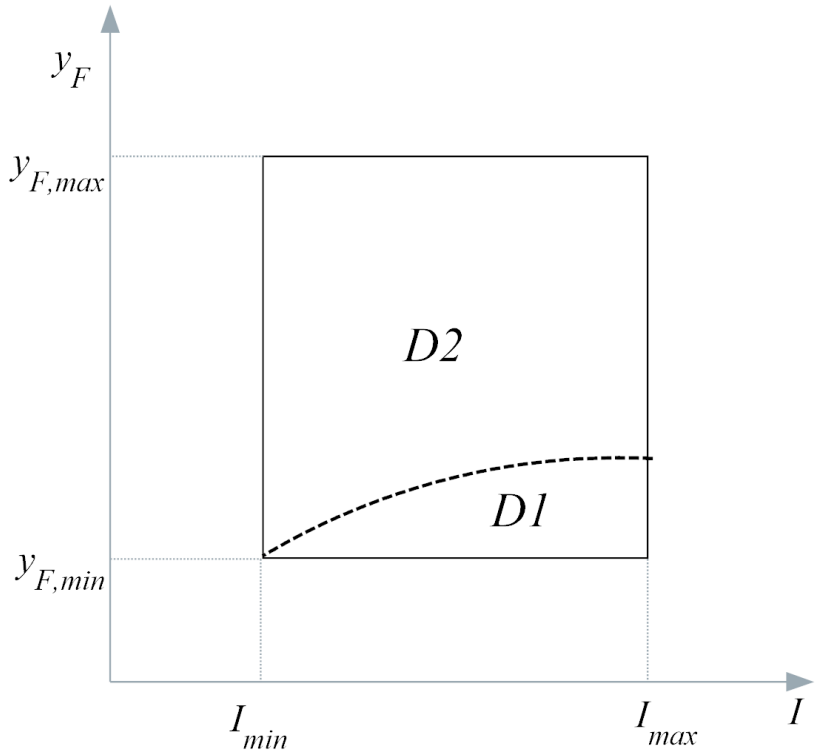


**Figure 60 τ section of the domain *D* and subdivision between direct strokes and indirect strokes areas.**

2. The Rusck-Darveniza formula [60] provides a (conservative) estimation of peak voltage as a function of $I$ and $y_F$. So, once the line CFO is known, the following inequality defines a region *D3* in which indirect strikes can cause dangerous overvoltage (see Figure 60)

$$\frac{I}{y_F} > \frac{CFO}{38.8\left(h + \frac{0.15}{\sqrt{\sigma_g}}\right)} \tag{224}$$

where $h$ is the conductors height, and σ the ground conductivity.

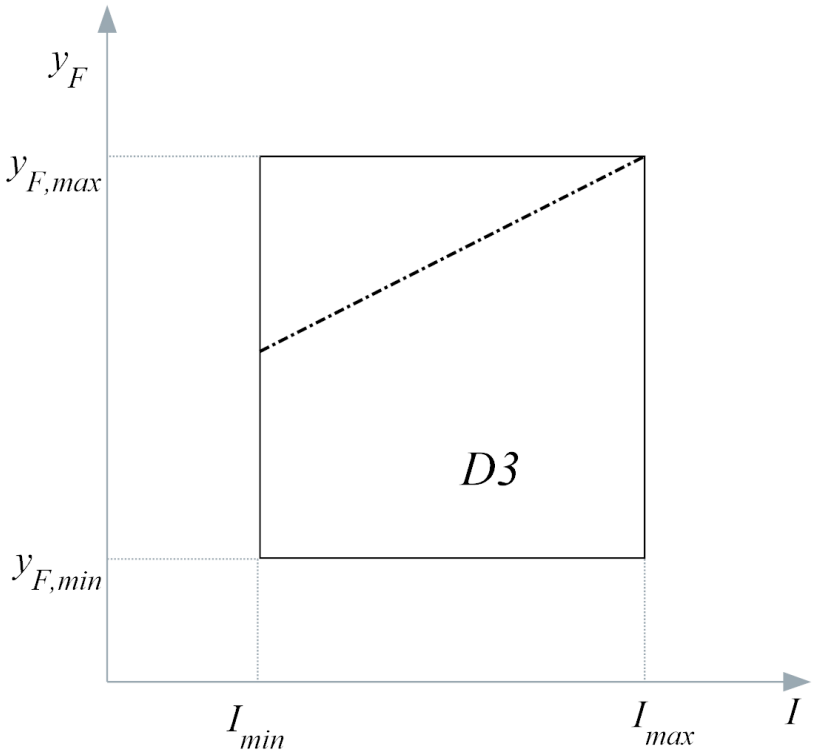


**Figure 61 $\tau_d$ section of the domain *D* and subdivision according to Rusck's formula**

As a consequence the domain of interest where (223) has to be evaluated is $D2 \cap D3$.

The key point is to evaluate the best values of coefficients appearing in the formula. This is done performing complete simulations with the code [34] for a set of $KHL$ specified points

$$\left(I_k, \tau_{d,h}, y_{F,l}\right) \in D2 \cap D3 \tag{225}$$

for $h = 1,...,H$, $k = 1,...,K$ and $l = 1,...,L$. The variables appearing in (223) are normalized in such a way that *D* is mapped into $[-1,1]\times[-1,1]\times[-1,1]$ and a least square method is applied to find the coefficients that minimize the difference between the exact values of *V* coming out of the simulations and the ones predicted by (223) in the $K \cdot H \cdot L$ chosen points. Empirical evaluations have shown that *K*=*L*=3 and *H*=2 provide a good fitting if points have been chosen according to Figure 62 in correspondence of $\tau_{d,min}$ and $\tau_{d,max}$. Please note that the points chosen on the y-axis correspond to the minimum, mean and maximum values of the stroke location corresponding to the minimum, median and maximum value of the current distribution. In this way, the described procedure requires only 18 code runs.

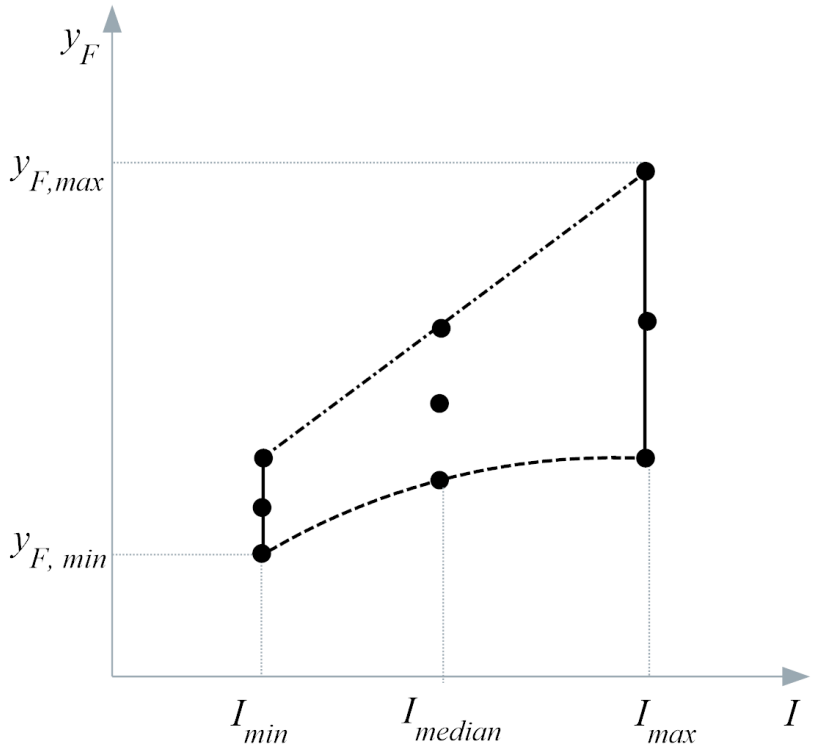


**Figure 62 $\tau_d$ section of the domain *D* and points of evaluation of the exact formula**

### 6.2.2 Dependence of the overvoltage on the horizontal position

The dependence on the horizontal position can be treated as proposed in [35].

Let us suppose to choose an initial guess sequence $x_{F,m}, m=1,...,M$ such that $x_{F,1}=x_{F,\min}$ and $x_{F,M}=x_{F,\max}$ (choice of $x_{F,\min}$ and $x_{F,\max}$ can be done as in [35]). Then, for $m=1,\ldots,M-1$ calculate the middle point $\frac{x_{F,m}+x_{F,m+1}}{2}$ of the $m^{th}$ interval and evaluate for any $h=1,...,H$, $k=1,...,K$ and $l=1,...,L$

$$V_{khl}=V\left(\frac{x_{F,m}+x_{F,m+1}}{2},I_k,\tau_{d,h},y_{F,l}\right) \tag{226}$$

and the corresponding "exact" values $V_{exact,khl}=V_{exact}\left(\frac{x_{F,m}+x_{F,m+1}}{2},I_k,\tau_{d,h},y_{F,l}\right)$ by means of simulation.

Then, for all the values that could be potentially dangerous (i.e. above a specified threshold $V_T$), calculate the deviation between exact and approximate values, i.e.

$$f_{khl}=\begin{cases}1 & if\ V_{exact,khl}\geq V_T\ i\\ 0 & otherwise\end{cases} \tag{227}$$

and evaluate the $e_{\%}$ error as

$$e_{\%} = 100 \sum_{k=1}^{K} \sum_{l=1}^{L} \sum_{h=1}^{H} \frac{\left| V_{exact,khl} - V_{khl} \right| f_{khl}}{V_{exact,khl}} \tag{228}$$

If $e_{\%}$ is higher than a threshold $e_T$, one has to continue in the "bisection" procedure, else it is possible to stop the process. The whole process appears in the flowchart of Figure 63.

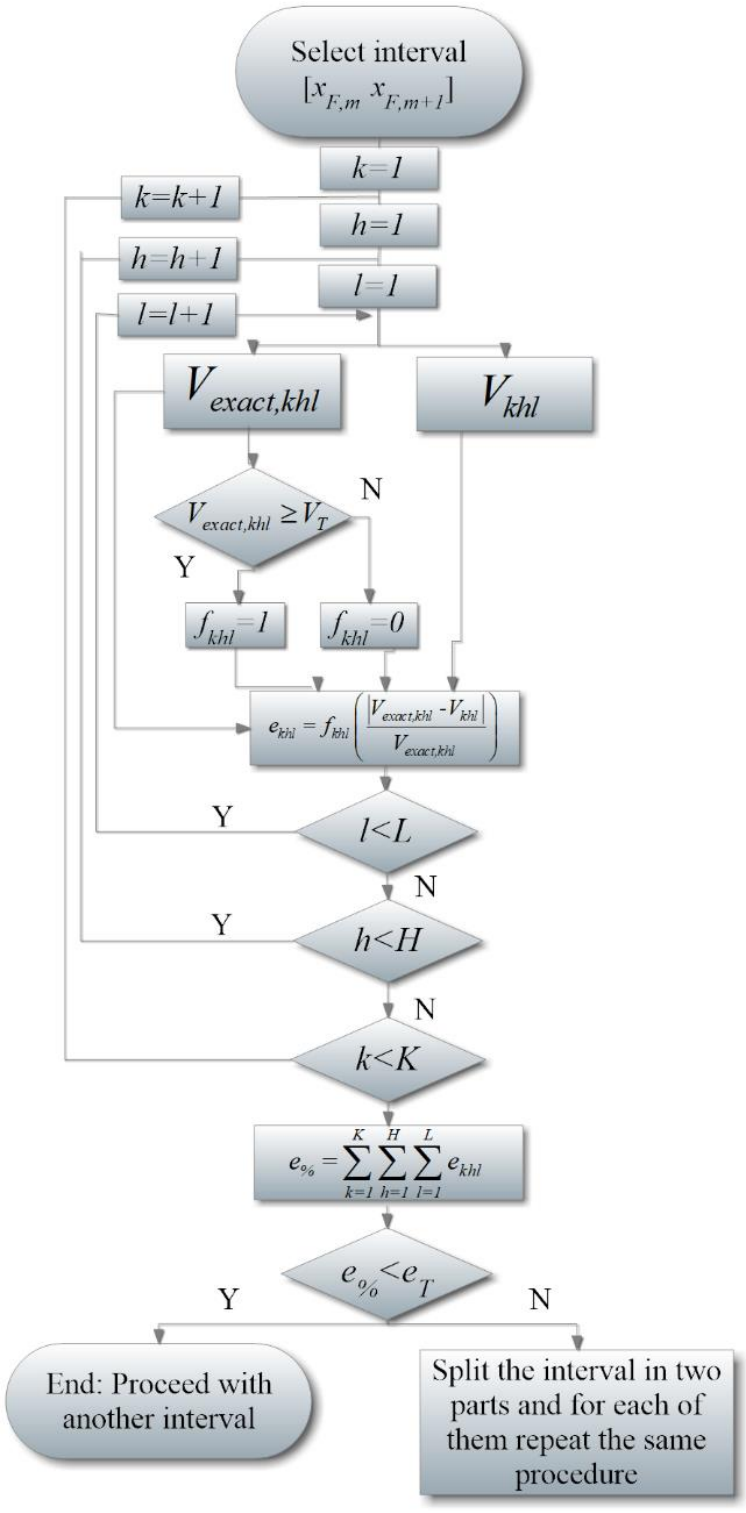


**Figure 63 Flowchart**

For each one of the intervals in which $\left[x_{F,\min}, x_{F,\max}\right]$ is divided, two formulas of the kind (223) are available corresponding to the two extremes of the interval itself. A linear interpolation

between them is then sufficient to calculate the overvoltage in any position $x_F$ belonging to such interval.

## 6.3 Validation of the proposed method

Let us consider the distribution line presented in Section 6.1. The validation consists of two different analyses:

1. Comparison of the proposed method with the exact one, computed with the coupling code in terms of punctual values of the maximum lightning induced overvoltages.
2. Comparison of the proposed method with the exact results, computed with the coupling code in terms of probability density functions of the maximum lightning induced overvoltages.

It is important to remind that 1) overcomes the aim of the proposed methodology. In fact, the analytical formula's main aim is to provide a simplified and fast formula for the overvoltage analysis in a probabilistic framework.

As outlined before, the knowledge of the input data in terms of current and front time distributions is mandatory. In this work the well-known distributions proposed by Berger are used [9].

Due to the fact that the proposed methodology provides an analytical formula as a function of 4 variables, in order to represent the comparison it has been chosen to keep constant $x_F$ to three different values (–500m, 0m, 500m) and to keep constant $\tau_d$ to the values corresponding to the 5$^{th}$, 50$^{th}$ and 95$^{th}$ percentile of its distribution. The following figures show the curves $V(y_F)$ parametrized to different values of $I$.

As apparent looking at Figure 61, the domain of each one dimensional curve depends on the current. So, for the sake of clarity, such curves are depicted in Figure 64 on a normalized range (0,1).

Figure 64 shows the results of the first validation for the negative first and subsequent strokes. The continuous line represents the approximate method, while the "stars" are the results of the exact one.

Horizontal line represent the 50 kV level (value chosen for $V_T$ in the procedure of the previous section) because the whole algorithm has been designed to adequately reproduce voltages greater than such $V_T$. Thus, the curves have to be judged above this line.

The exam of Figure 64 suggests that: i) when a lightning strikes outside the line the agreement between simulations and the proposed approach is quite good but, in any case, the induced overvoltages are quite far from assuming dangerous values (panels A and B); ii) for point of impact abscissa equal to the line end, there are some differences for very close distances

between line and stroke location, but it never happens that the proposed approach predicts values below the threshold and simulation above it or vice versa (panels C and D); iii) if the lightning strikes in the middle of the line, there is a good agreement between the two approaches with some overestimation of the approximate method (panels E and F a part from the case of $\tau_d = 18\mu s$, which, by the way, does not produce dangerous overvoltages).

Figure 65 and Figure 66 present the validation of the proposed approach in terms of probability, considering 10000 events of first/subsequent strokes extracted inside the domain of Figure 61. The Probability Density Functions (PDF) and the Cumulative Density Functions (CDF) of the maximum voltage are shown, confirming a good agreement between the two approaches. Table 19 shows the results of Figure 66 in terms of intersections with the 5th, 50th and 95th percentile.

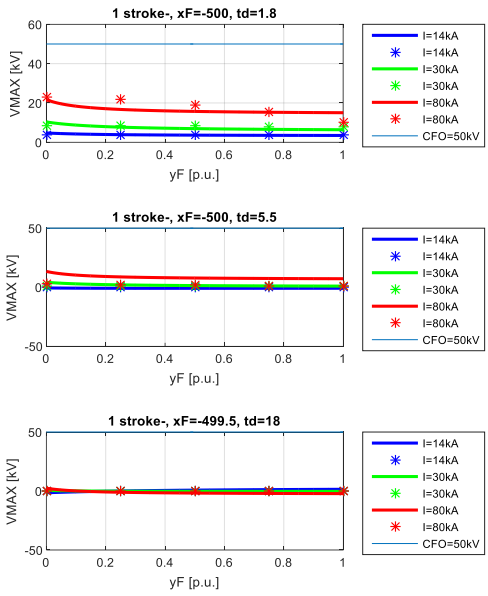


A)

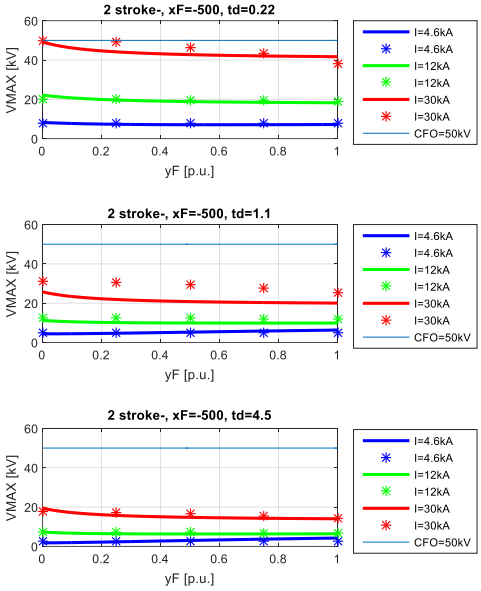


B)

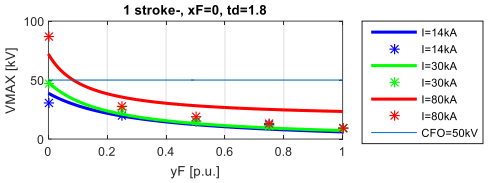
1 stroke-, xF=0, td=1.8
VMAX [kV]
yF [p.u.]
I=14kA
I=14kA
I=30kA
I=30kA
I=80kA
I=80kA
CFO=50kV

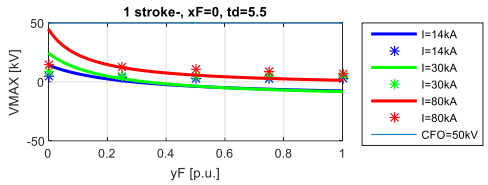
1 stroke-, xF=0, td=5.5
VMAX [kV]
yF [p.u.]
I=14kA
I=14kA
I=30kA
I=30kA
I=80kA
I=80kA
CFO=50kV

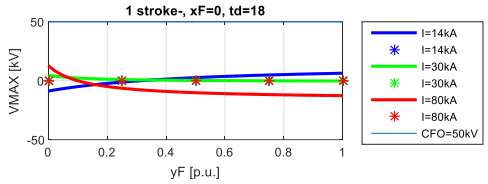
1 stroke-, xF=0, td=18
VMAX [kV]
yF [p.u.]
I=14kA
I=14kA
I=30kA
I=30kA
I=80kA
I=80kA
CFO=50kV

C)

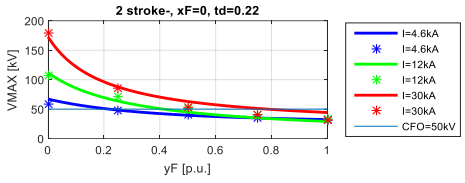
2 stroke-, xF=0, td=0.22
VMAX [kV]
yF [p.u.]
I=4.6kA
I=4.6kA
I=12kA
I=12kA
I=30kA
I=30kA
CFO=50kV

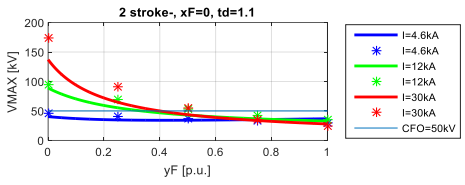
2 stroke-, xF=0, td=1.1
VMAX [kV]
yF [p.u.]
I=4.6kA
I=4.6kA
I=12kA
I=12kA
I=30kA
I=30kA
CFO=50kV

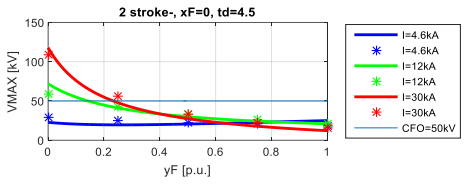
2 stroke-, xF=0, td=4.5
VMAX [kV]
yF [p.u.]
I=4.6kA
I=4.6kA
I=12kA
I=12kA
I=30kA
I=30kA
CFO=50kV

D)

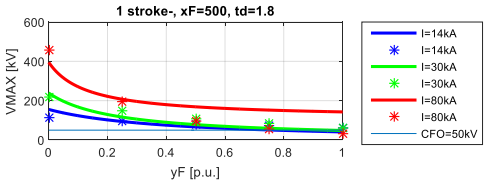
1 stroke-, xF=500, td=1.8
VMAX [kV]
yF [p.u.]
I=14kA
I=14kA
I=30kA
I=30kA
I=80kA
I=80kA
CFO=50kV

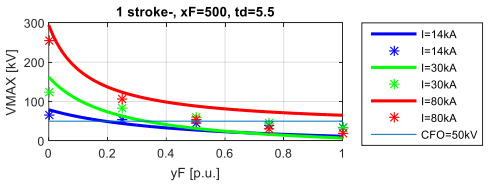
1 stroke-, xF=500, td=5.5
VMAX [kV]
yF [p.u.]
I=14kA
I=14kA
I=30kA
I=30kA
I=80kA
I=80kA
CFO=50kV

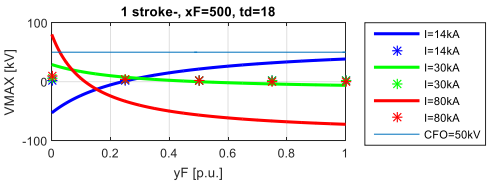
1 stroke-, xF=500, td=18
VMAX [kV]
yF [p.u.]
I=14kA
I=14kA
I=30kA
I=30kA
I=80kA
I=80kA
CFO=50kV

E)

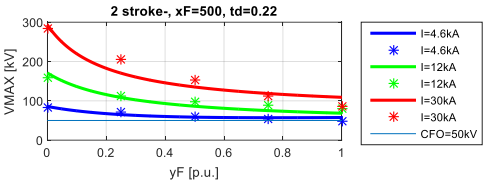
2 stroke-, xF=500, td=0.22
VMAX [kV]
yF [p.u.]
I=4.6kA
I=4.6kA
I=12kA
I=12kA
I=30kA
I=30kA
CFO=50kV

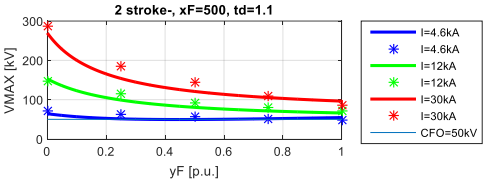
2 stroke-, xF=500, td=1.1
VMAX [kV]
yF [p.u.]
I=4.6kA
I=4.6kA
I=12kA
I=12kA
I=30kA
I=30kA
CFO=50kV

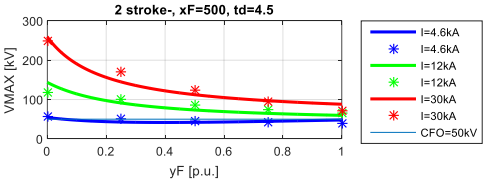
2 stroke-, xF=500, td=4.5
VMAX [kV]
yF [p.u.]
I=4.6kA
I=4.6kA
I=12kA
I=12kA
I=30kA
I=30kA
CFO=50kV

F)

**Figure 64 A), B) $x_F$= -500m First and Subsequent strokes C), D) $x_F$= 0m First and Subsequent strokes E), F), $x_F$= 500m First and Subsequent strokes**

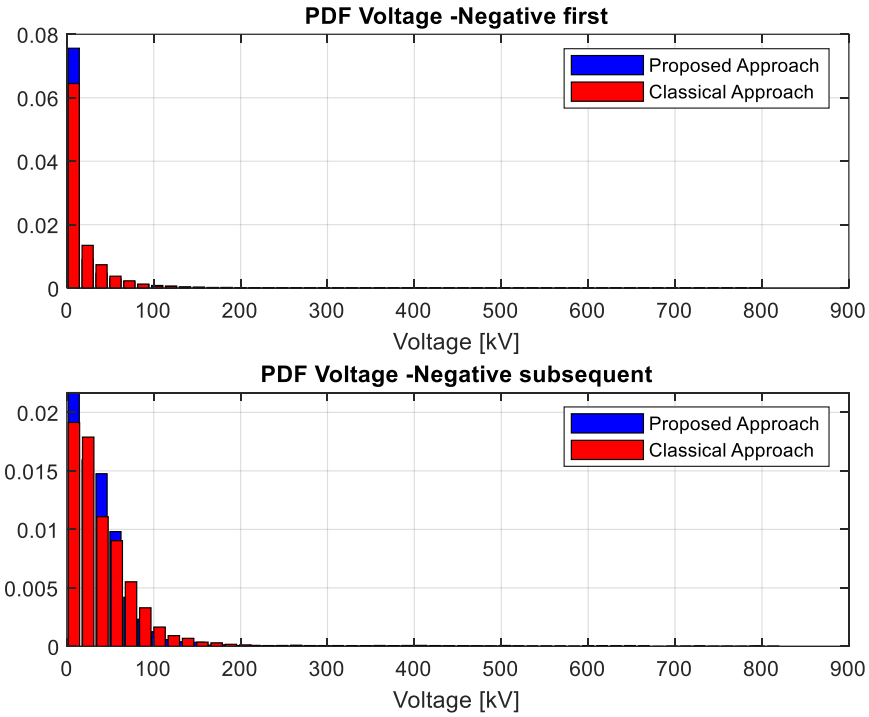


**Figure 65 PDF of the maximum voltage occurred on the line**

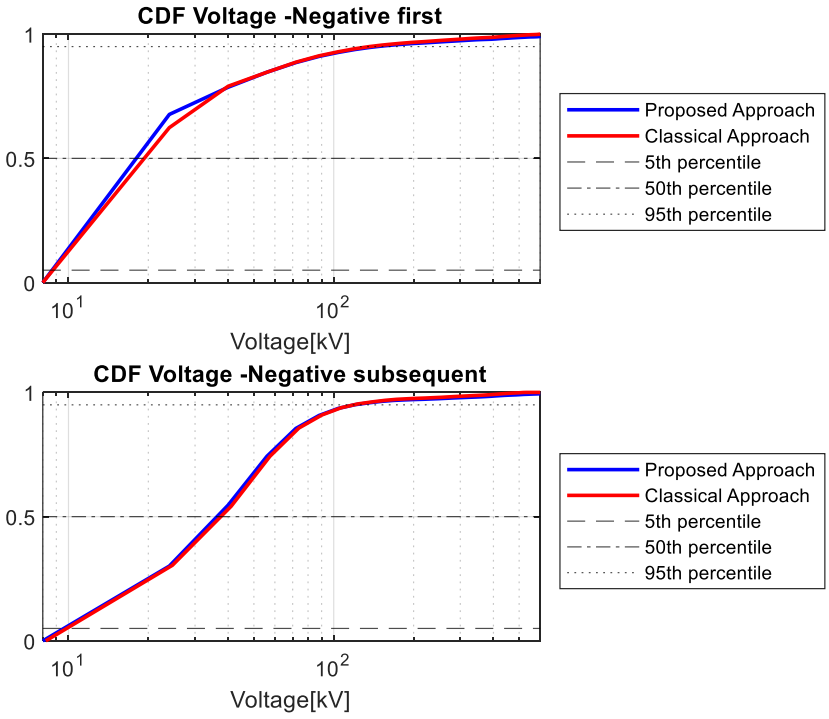


**Figure 66 CDF of the maximum voltage occurred on the line**

**Table 19 Validation in terms of probability**

| | Negative first | | Subsequent | |
|---|---|---|---|---|
| | Proposed approach | Classical approach | Proposed approach | Classical approach |
| 5$^{th}$ percentile | 8.65 kV | 8.73 kV | 9.6 kV | 9.8 kV |
| 50$^{th}$ percentile | 18.01 kV | 19.3 kV | 36.2 kV | 37.5 kV |
| 95$^{th}$ percentile | 143 kV | 136.1 kV | 119 kV | 120.8 kV |
| P($V_{max}$>*50 kV*) | 18.1% | 17% | 32% | 34% |

The initial number of selected horizontal points is M=4 and the iterative process of Figure 63 leads to M=6, considering $e_T$=*5%*. So, the number of code calls is 18x6. This requires less than 15 minutes, while the exact evaluation of voltage PDF needs more than 16 hours. These results have been obtained using a Microsoft Windows 10 PC equipped with 16 Gb of RAM and Intel Core i7-2600 CPU at 3.4GHz.

The obtained validation in terms of pdf of the induced voltage is extremely important because allow to say that the proposed formula can be used in the lightning performance procedure where it is then necessary to multiply the obtained result for the GFD.

# 7 Mitigation of lightning-induced overvoltages using shield wires: application of the Response Surface Method (RSM)

Many papers have dealt with the use of shield wires, discussing the effect of parameters such as the distance between two subsequent grounding points [38, 53, 54], or presenting experimental results to assess their effectiveness [55-58].

The studies presented in [54] have focused on the parameters that affect the effectiveness of shield wires on the mitigation of lightning-induced voltages. The results obtained have demonstrated that the most relevant ones are the relative position of the shield wire with respect to the phase conductors, the grounding interval and the ground resistance. The individual effect of each parameter is well described in [1, 54], but a thorough analysis on their combined effect is still missing. Moreover, the aforementioned papers presented the effectiveness of the shield wire calculating the overvoltage in the point closest to the strike location and not in the overall system.

In this context, a statistical approach that takes into account all the involved parameters effects can be very useful in designing the lightning protection system of MV networks.

RSM represents a very powerful tool to analyse how the response of a very complex system depends on its input parameters without requiring a prohibitive number of runs of the numerical simulation to describe the response of the system [94]. This method has been frequently applied in reliability analysis (e.g., [95-99]) and has found some applications also in power system [100-102] and control analysis [103]. In [100], the size of a PV/wind hybrid energy conversion system with battery storage is optimized using RSM based on an hourly operating cost. The work in [101] presents a new probabilistic power flow method based on the Stochastic Response Surface Method (SRSM), while the same method is used in [102] for the evaluation of optimal power flow with wind generators.

This chapter proposes an analysis in which the RSM is used to evaluate the lightning performance of a realistic distribution network equipped with shield wires, and how their configuration (position, grounding spacing and grounding resistance) affects their performance.

The proposed approach is efficient from a computational point of view because the RSM method requires a limited number of simulation runs. Furthermore, the lightning performance computation for different shield wire configurations dictated by the RSM method is performed using an efficient code described in [35] and [34]. The main advantages of the proposed method are: the possibility of dealing with a realistic configuration, accounting for the probability

distribution functions of both the current peak and the lightning strike position, and modelling the lightning channel base current with any desired expression (in the chapter, the well-known Heidler's formula is used [15]). Moreover, the use of a statistical approach allows not to limit the lightning performance analysis to the overvoltage experienced by the point of the line closest to the lightning strike location (which is not guaranteed to be the maximum system overvoltage), but rather to consider all the points along the overall system.

Finally, the method allows obtaining a simple formula linking the system response (the overvoltage reduction or the lightning performance) to the shield wires parameters. Such formula can be used: i) to find an estimate of the optimal shield wires configuration together with its confidence strip, ii) to perform a sensitivity analysis on the dependence of the response on each input variable, iii) to evaluate the effect of the interactions among the variables and iv) to check whether some of them do not influence the reduction on the system overvoltage in a meaningful way. The chapter is organized as follows: Section 7.1 is dedicated to an overview of the RSM method. Section 7.2 describes the test case network and the shield wires parameters. Section 7.3 illustrates the application of the RSM method to assess the effectiveness of shield wires in the mitigation of lightning induced overvoltages. Section 7.4 presents a sensitivity analysis on the shield wire parameters.

## 7.1 Overview of the RSM Method

The RSM aims at describing the response of a complex process by means of a polynomial relation, providing also an estimation of the error due to the use of the obtained approximate model. A complete description of the RSM can be found in [94]. The aim of this section is to provide the reader with an overview of the method, whose conceptual flowchart, consists of the following steps:

1. Definition of the input variables and their domain

The first step consists of defining the $n$ variables $z_i$ that affect the system response estimation $\tilde{y}$ together with their physical domain $[z_{imin}, z_{imax}]$. The choice of the domain is crucial as the response surface, being calculated starting from the system response at the domain boundaries, strongly depends on it. For the future derivation, for each variable $z_i$, a linear transformation is needed that maps $[z_{imin}, z_{imax}]$ into $[-1,1]$, leading to the definition of $n$ new variables $x_i$:

$$x_i = \frac{2}{z_{i\max} - z_{i\min}}\left(z_i - z_{i\min}\right) - 1 \tag{229}$$

2. Model definition

Typically, the considered models for describing the response surface are polynomial models, more precisely: a first order model (230), a first order model with interaction (231) (where binary interactions are included), and a complete second-order model (232):

$$\tilde{y} = a_0 + \sum_{i=1}^{n} a_i x_i \tag{230}$$

$$\tilde{y} = a_0 + \sum_{i=1}^{n} a_i x_i + \sum_{\substack{i,j=1 \\ i<j}}^{n} a_{ij} x_i x_j \tag{231}$$

$$\tilde{y} = a_0 + \sum_{i=1}^{n} a_i x_i + \sum_{\substack{i,j=1 \\ i<j}}^{n} a_{ij} x_i x_j + \sum_{i=1}^{n} a_{ii} x_i^2 \tag{232}$$

$a_i$ being the unknown tuning coefficients.

3. Number of observations definition

In order to estimate the tuning coefficients, a number of system response observations $y_p$ (function of the selected model) has to be provided. The choice of the optimal number of the provided observations and their position in the space is a crucial point. It was established [94] that the best choice to fit a second order model is to consider:

- the vertexes of the hyper-cube $[-1,1]^n$, i.e. all the $2^n$ points $\left((-1)^{\beta_1},\ldots,(-1)^{\beta_n}\right)$ with $\beta_i \in \{0,1\}$ for all $i = 1,\ldots,n$;
- the center of the hypercube, i.e. the point $(0,\ldots,0)$;
- the $2n$ points $\left(0,\ldots,-\sqrt{n},\ldots,0\right)$ and $\left(0,\ldots,\sqrt{n},\ldots,0\right)$, or $(0,\ldots,\pm 1,\ldots,0)$, whenever one of them is not physically consistent, that correspond to the $2n$ points on the smallest sphere that contains the cube.
- the central point of the corresponding face of the hypercube

In this way $2^n+2n+1$ observations are at disposal. It should be observed that, when dealing with experimental campaigns, each observation consists of a measurement. Here, this will be surrogated by numerical simulations [34] and extrapolating the desired system response, as will be detailed later in the chapter.

4. Estimation of the tuning parameters

Equations (230)-(232) represent multiple regression models with $n$ independent variables. It can be observed that, introducing the $N = (n^2+3n+2)/2 - 1$ coefficients $\alpha_i$ such that

- $\alpha_i = a_i$ for any $i = 1,\ldots,n$

- $\alpha_{ni+j} = a_{ij}$ for any $i = 1,\ldots,n$ and $i < j$
- $\alpha_{i+(n^2+n)/2} = a_{ii}$ for any $i = 1,\ldots,n$

and similarly the new *N* coordinates $\xi_i$ such that

- $\xi_i = x_i$ for any $i = 1,\ldots,n$
- $\xi_{ni+j} = x_i x_j$ for any $i = 1,\ldots,n$ and $i < j$
- $\xi_{i+(n^2+n)/2} = x_i^2$ for any $i = 1,\ldots,n$

the model presented in (230)-(232) can be written in the linear form:

$$\tilde{y} = a_0 + \sum_{i=1}^{N} \alpha_i \xi_i \tag{233}$$

The tuning coefficients are then estimated with the well-known least squares method, that consists of choosing the set $\boldsymbol{\alpha} = [a_0, \alpha_1, ..., \alpha_N]^T$ which minimizes the sum of squares *L* of the errors vector, defined in (234), where *P* is the number of observations, $\mathbf{y} = [y_1,\ldots,y_P]^T$ collects the *P* observations and $(x_{p,1},\ldots,x_{p,n})$ corresponds to the *p*-th observation $y_p$

$$L = \sum_{p=1}^{P} \left( y_p - a_0 - \sum_{i=1}^{N} \alpha_i \xi_{p,i} \right)^2 \tag{234}$$

The minimum occurs in correspondence of the values of $\boldsymbol{\alpha}$ that nullify the gradient of *L* [94], that is to say:

$$\frac{\partial L}{\partial \boldsymbol{\alpha}} = -2\boldsymbol{\Xi}^T \mathbf{y} + 2\boldsymbol{\Xi}^T \boldsymbol{\Xi} \boldsymbol{\alpha} = \mathbf{0} \tag{235}$$

where $\boldsymbol{\Xi} = \begin{bmatrix} 1 & \xi_{1,1} & \cdots & \xi_{1,N} \\ \vdots & \vdots & \ddots & \vdots \\ 1 & \xi_{P,1} & \cdots & \xi_{P,N} \end{bmatrix}$. The solution of (235) provides the values of the tuning coefficients $\bar{\boldsymbol{\alpha}}$ that minimize *L*:

$$\bar{\boldsymbol{\alpha}} = \left( \boldsymbol{\Xi}^T \boldsymbol{\Xi} \right)^{-1} \boldsymbol{\Xi}^T \mathbf{y} \tag{236}$$

5. Choice of the meaningful variables

In order to check whether the variables $z_i$ contribute significantly to the regression model, a procedure, called extra sum of squares method, is used. This procedure is completely described in [94] and allows to reject all the variables that do not affect the system response in a meaningful way.

6. Check of the model adequacy

Once the response surface is available, it is necessary to have some indicators on the goodness of the used methodology. In particular, for any $\beta \in (0,1)$ the 100(1−$\beta$)% confidence intervals of the regression coefficients and of the system mean response $\mu$ at the point $\mathbf{x_0} = (x_{0,1},\ldots,x_{0,n})$ can be evaluated according to the procedure described in [94].

More precisely, if $C_{ii}$ is the *ii*-entry of matrix $\boldsymbol{\Xi}^T\boldsymbol{\Xi}$ and σ represents the variance estimate, provided by $\sigma = \sqrt{\left(\mathbf{y}^T\mathbf{y} - \bar{\boldsymbol{\alpha}}^T\mathbf{X}^T\mathbf{y}\right)/(P-N)}$, then the 100(1−$\beta$)% confidence interval for the coefficient $\alpha_i$ is given by:

$$\bar{\alpha}_i - t_{\beta/2,P-N-1}\sqrt{\sigma^2 C_{ii}} \le \alpha_i \le \bar{\alpha}_i + t_{\beta/2,P-N-1}\sqrt{\sigma^2 C_{ii}} \tag{237}$$

where t is the Student's t-distribution with $P-N-1$ degrees of freedom.

Similarly, the 100(1−$\beta$)% confidence interval for the system mean response $\mu$ at the point $\mathbf{x_0} = (x_{0,1},\ldots,x_{0,n})$ is given by:

$$\begin{aligned} \hat{y}_0 - t_{\beta/2,P-N-1}\sqrt{\sigma^2\boldsymbol{\xi}_0^T\left(\boldsymbol{\Xi}^T\boldsymbol{\Xi}\right)^{-1}\boldsymbol{\xi}_0} \le \mu \\ \le \hat{y}_0 + t_{\beta/2,P-N-1}\sqrt{\sigma^2\boldsymbol{\xi}_0^T\left(\boldsymbol{\Xi}^T\boldsymbol{\Xi}\right)^{-1}\boldsymbol{\xi}_0} \end{aligned} \tag{238}$$

where $\hat{y}_0 = \bar{\boldsymbol{\alpha}}^T\boldsymbol{\xi}_0$ and $\boldsymbol{\xi}_0 = \left[1,\xi_{0,1},\ldots,\xi_{0,N}\right]^T$ is the column vector associated to $\mathbf{x_0}$.

## 7.2 The MV network test case

Let us consider the line topology shown in Figure 67, where a main feeder of length 1200 m and three laterals (at 300 m, 600 m and 900 m from the beginning of the feeder), each one of length 300 m, have been considered. Table 20 reports the main geometrical parameters of each of the lines appearing in Figure 67 and Figure 68.

**Table 20 Line Details**

| Name | Description / Value |
|---|---|
| Conductor diameters | 2 cm |
| Line configuration | 3 phase |
| Phase conductor height | 10 m |
| Phase distance | 75 cm |

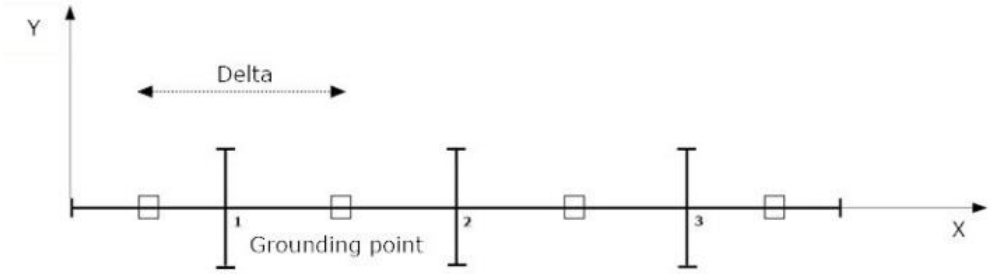


**Figure 67 Line topology**

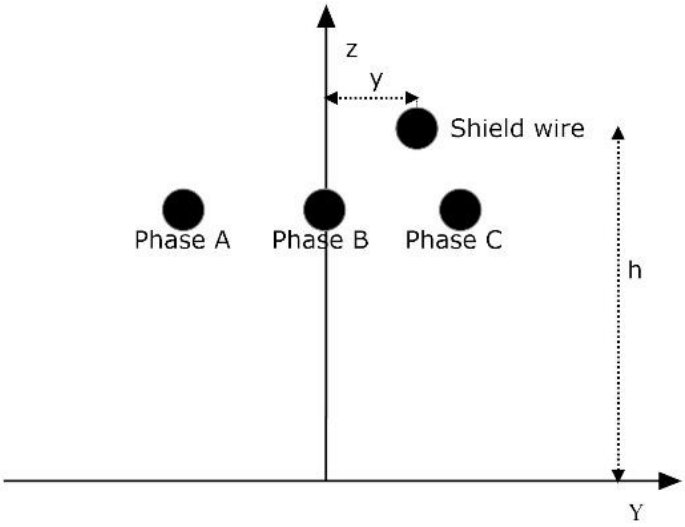


**Figure 68 Line cross section**

According to [54], four parameters that affect the performance of the shield wires have been considered in the proposed model: the shield wire height *h*, the distance between two subsequent grounding points *Delta*, the ground resistance $R_g$ and the horizontal distance *y* of the shield wire from the middle phase conductor. The chosen range of variability of each parameter is shown in Table 21, where $z_i$ is the generic name given to each parameter, as described in Section 7.1.

**Table 21 Range of variability of the parameters affecting the shield wire performance**

| Name | DESCRIPTION | Min | Max |
|---|---|---|---|
| *Delta* ($z_1$) | Distance between two subsequent groundings | 100 m | 300 m |
| $R_g$ ($z_2$) | ground resistance | 1 Ω | 200 Ω |
| $h$ ($z_3$) | height of the shield wire | 7 m | 12 m |
| $y$ ($z_4$) | Horizontal distance of the shield wire from the middle phase conductor | -0.75 m | 0.75 m |

## 7.3 Shield wire efficiency assessment

In this section, the RSM method is applied to assess the effectiveness of the shield wires in mitigating lightning induced overvoltages. The first important point is to define the "system response". In the present analysis, two possibilities are considered. The first is aimed at checking whether the shield wires are always effective in reducing the induced overvoltages no matter their configurations and for any possible lightning strike. The second follows the objective of enhancing the system lightning performance.

### 7.3.1 Reduction of the maximum overvoltage

The first analysis is performed according to the following steps:

1) Consider the test case of Figure 67 without any shield wires.
2) Define a domain $D$ for the lightning point of impact. The present choice is to consider the region limited by the red and the blue lines in Figure 69. The red line delimits the zone in which the probability of a direct stroke is greater than 99.9% according to the Electrogeometrical Model (EGM) [51]. The region outside the blue one, on the other hand, is characterized by a probability of having an overvoltage greater than the network Critical Flashover Voltage (*CFO*) smaller than 0.1%. These two regions have been obtained as follows: a) the red area has been computed with the EGM inputted with the line details and with the current representing the first thousandth of the cumulative probabilistic distribution (i.e., the 99.9% of the currents are higher than that value); b) the blue area has been computed with the Rusck's model [38] inputted with the line details and with the current representing the 999$^{th}$ thousandth of the cumulative distribution function (i.e. the 0.1% of the currents are higher than that value).

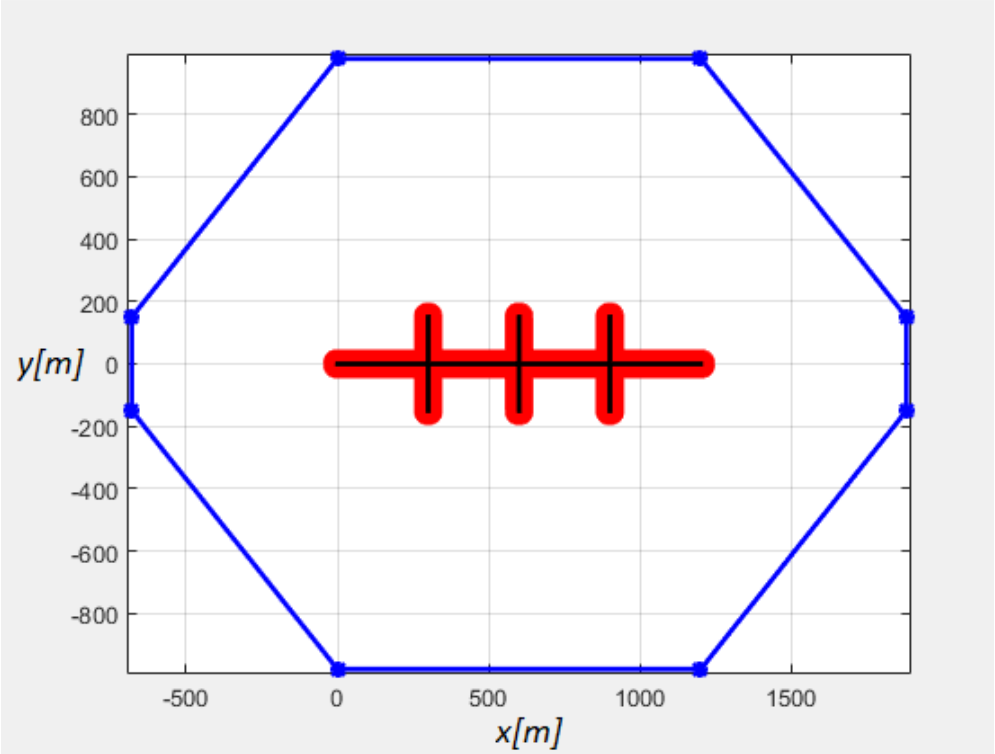


**Figure 69 Coordinates domain**

Concerning the ground electrical parameters, they in principle depend on the frequency [104, 105] and on the ground stratification. However, these effects have been not considered firstly because this would be quite complex [24, 34, 35] and case dependent, secondly because most of the studies dealing with the lightning performance analysis of power lines assume constant and frequency-independent ground electrical parameters. Thus, the soil is supposed to be characterized by a conductivity equal to $5 \cdot 10^{-3}$ S/m, while the conductor lines are supposed to be perfect conductors, as the wire impedance is generally negligible with respect to the ground impedance.

3) Define a sequence of points of impact $P_{hk}=(x_h,y_k)$ inside the domain (in the present analysis, 45×26 points have been considered)
4) For each of these points, run the code developed in [34] to calculate the maximum overvoltage $V_{\max}^{noSW}(x_h, y_k, I_F)$ occurring in the whole system assuming a Heidler's waveform [15] for the lightning channel-base current with a peak value equal to $I_F$ and front time of about 3.2 μs (the other parameters are the ones taken from [32]).
5) Consider the presence of the shield wires, repeat point 4 for all the $2^4+2\cdot 4+1=25$ combinations of the shield wire parameters appearing in Table 22 and evaluate the corresponding maximum overvoltage $V_{\max}^{TEST,j}(x_h, y_k, I_F) \quad j=1,\ldots,25$

**Table 22 25 Test details (the values of the parameters, after the transformation (229) correspond to the points defined in section 7.1.**

| Test | Delta (m) | $R_g$ (Ohm) | h (m) | y (m) |
|---|---|---|---|---|
| *Test 1* | 100.0 | 1.0 | 7.0 | -0.75 |
| *Test 2* | 100.0 | 1.0 | 7.0 | 0.75 |
| *Test 3* | 100.0 | 1.0 | 12.0 | -0.75 |
| *Test 4* | 100.0 | 1.0 | 12.0 | 0.75 |
| *Test 5* | 100.0 | 200.0 | 7.0 | -0.75 |
| *Test 6* | 100.0 | 200.0 | 7.0 | 0.75 |
| *Test 7* | 100.0 | 200.0 | 12.0 | -0.75 |
| *Test 8* | 100.0 | 200.0 | 12.0 | 0.75 |
| *Test 9* | 300.0 | 1.0 | 7.0 | -0.75 |
| *Test 10* | 300.0 | 1.0 | 7.0 | 0.75 |
| *Test 11* | 300.0 | 1.0 | 12.0 | -0.75 |
| *Test 12* | 300.0 | 1.0 | 12.0 | 0.75 |
| *Test 13* | 300.0 | 200.0 | 7.0 | -0.75 |
| *Test 14* | 300.0 | 200.0 | 7.0 | 0.75 |
| *Test 15* | 300.0 | 200.0 | 12.0 | -0.75 |
| *Test 16* | 300.0 | 200.0 | 12.0 | 0.75 |
| *Test 17* | 100.0 | 100.5 | 9.5 | 0.00 |
| *Test 18* | 400.0 | 100.5 | 9.5 | 0.00 |
| *Test 19* | 200.0 | 1.0 | 9.5 | 0.00 |
| *Test 20* | 200.0 | 299.5 | 9.5 | 0.00 |
| *Test 21* | 200.0 | 100.5 | 7.0 | 0.00 |
| *Test 22* | 200.0 | 100.5 | 14.5 | 0.00 |
| *Test 23* | 200.0 | 100.5 | 9.5 | -1.50 |
| *Test 24* | 200.0 | 100.5 | 9.5 | 1.50 |
| *Test 25* | 200.0 | 100.5 | 9.5 | 0.00 |

6) Calculate the following Key Performance Indicators (KPIs) choosing them as the system response:

$$KPI_{\min}(j) = \min_{\substack{P_{hk} \in D \\ I_F > 0}} f(P_{hk}, I_F; j) \tag{239}$$

$$KPI_{\max}(j) = \max_{\substack{P_{hk} \in D \\ I_F > 0}} f(P_{hk}, I_F; j) \tag{240}$$

where

$$f(P_{hk}, I_F; j) = \frac{V_{\max}^{noSW}(x_h, y_k, I_F) - V_{\max}^{TESTj}(x_h, y_k, I_F)}{V_{\max}^{noSW}(x_h, y_k, I_F)} \tag{241}$$

It should be observed that the chosen test case networks do not contain any nonlinear device (e.g. surge arresters) because the aim of the chapter is to assess the effectiveness of the shield wires. If a combined protection system was used (shield wires + arresters), the procedure could be repeated without any meaningful modification.

Let us observe that, due to the symmetry of the chosen network, the domain $D$ can be reduced to the positive region for the $y$ coordinate. More precisely, let us split $D = D_+ \cup D_-$, where $D_+ = \{(x,y) \in D : y \geq 0\}$, and $D_- = \{(x,y) \in D : y \leq 0\}$. In this framework,

$$\begin{aligned} KPI_{\min}(j) &= \min\left\{ \min_{\substack{P_{hk} \in D_+ \\ I_F > 0}} f(P_{hk}, I_F; j), \min_{\substack{P_{hk} \in D_- \\ I_F > 0}} f(P_{hk}, I_F; j) \right\} \\ &= \min\left\{ \min_{\substack{P_{hk} \in D_+ \\ I_F > 0}} f(P_{hk}, I_F; j), \min_{\substack{P_{hk} \in D_+ \\ I_F > 0}} f(P_{hk}, I_F; j^*) \right\} \end{aligned} \tag{242}$$

Where test $j^*$ represents the symmetric configuration with respect $y$ to test $j$, i.e.

$$j^* = \begin{cases} j+1 & j \in \{1,3,5,7,9,11,13,15,23\} \\ j-1 & j \in \{2,4,6,8,10,12,14,16,24\} \\ j & j \in \{17,18,19,20,21,22,25\} \end{cases} \tag{243}$$

The values of the two chosen KPIs are reported in Table 23, where one can appreciate that, no matter its configuration, the shield wire is always effective, since $KPI_{\min}$ is always positive. The evaluation of $KPI_{\min}$ can be used in those cases when a certain threshold of positive effect has to be reached, while $KPI_{\max}$ has to be used when the maximum positive effect is necessary. Applying the RSM to this problem, it is possible to obtain the coefficients of the polynomial relationship (232) between the KPIs and the four above defined parameters (see Table 24).

**Table 23 Maximum overvoltage reduction – KPI results**

| Test | $KPI_{MIN}$ | $KPI_{MAX}$ |
|---|---|---|
| *Test 1* | 0.04 | 0.16 |
| *Test 2* | 0.04 | 0.16 |
| *Test 3* | 0.08 | 0.30 |
| *Test 4* | 0.08 | 0.30 |
| *Test 5* | 0.04 | 0.10 |
| *Test 6* | 0.04 | 0.10 |
| *Test 7* | 0.08 | 0.20 |
| *Test 8* | 0.08 | 0.20 |
| *Test 9* | 0.02 | 0.12 |
| *Test 10* | 0.02 | 0.12 |
| *Test 11* | 0.04 | 0.25 |
| *Test 12* | 0.04 | 0.25 |
| *Test 13* | 0.01 | 0.06 |
| *Test 14* | 0.01 | 0.06 |
| *Test 15* | 0.03 | 0.13 |
| *Test 16* | 0.03 | 0.13 |
| *Test 17* | 0.08 | 0.25 |
| *Test 18* | 0.03 | 0.22 |
| *Test 19* | 0.08 | 0.34 |
| *Test 20* | 0.07 | 0.13 |
| *Test 21* | 0.04 | 0.10 |
| *Test 22* | 0.06 | 0.18 |
| *Test 23* | 0.05 | 0.16 |
| *Test 24* | 0.05 | 0.16 |
| *Test 25* | 0.07 | 0.21 |

**Table 24 Coefficients for system response (239) and (240)**

| | Value | |
|---|---|---|
| Coefficients | $KPI_{min}$ | $KPI_{max}$ |
| $a_0$ | 0.068640 | 0.235366 |
| $a_1$ | -0.017030 | -0.020256 |
| $a_2$ | 0 | -0.046689 |
| $a_3$ | 0.016268 | 0.058405 |
| $a_4$ | 0 | 0 |
| $a_{12}$ | 0 | 0 |
| $a_{13}$ | -0.004372 | 0 |
| $a_{14}$ | 0 | 0 |
| $a_{23}$ | 0 | -0.013147 |
| $a_{24}$ | 0 | 0 |
| $a_{34}$ | 0 | 0 |
| $a_{11}$ | -0.004807 | 0 |
| $a_{22}$ | 0 | 0 |
| $a_{33}$ | -0.013100 | -0.047513 |
| $a_{44}$ | -0.005185 | -0.019616 |

Examining Table 24, the following considerations can be made:

- The $KPI_{min}$ appears to be independent from the ground resistance, which implies that a minimum benefit due to the introduction of the shield wire in the system is guaranteed independently of the value of this parameter.
- The effect of the interactions among the variables is quite modest
- The dependence of the system response on the spacing is almost linear, while the other two parameters (height and horizontal position) affect the KPIs in a quadratic way. This sounds reasonable especially for the horizontal position due to the symmetry of the configuration.

The optimal point, the best KPI value and its confidence strip at 95% level of confidence are reported in for both cases.

**Table 25 Optimal point, best value and confidence strip for system response (239) and (240)**

| Case | OPTIMAL POINT | BEST VALUE | CONFIDENCE STRIP (95%) |
|---|---|---|---|
| $KPI_{min}$ | Delta = 100.0 m<br>$R_g$ = -<br>h = 11.4 m<br>y = 0.00 m | 0.089 | [0.083, 0.095] |
| $KPI_{max}$ | Delta = 100.0 m<br>$R_g$ = 1.0 Ω<br>h = 11.4 m<br>y = 0.00 m | 0.329 | [0.310, 0.349] |

The RSM ensures that the best performances (a reduction of at least 9%) can be obtained with the configuration reported in Table 25. The two optimal points are very close to each other and lead substantially to the same practical configuration, characterized by *Delta* = 100.0 m, $h$ = 11.4 m, $y$ = 0.0 m, and $R_g$ = 1 Ω (as $KPI_{min}$ does not depend on $R_g$, one can choose the one that maximizes $KPI_{max}$). This confirms the results reported in [54] according to which the smaller the grounding spacing and resistance, the more effective the shield wire action. Such best value ensures that, no matter the lightning point of impact, a reduction of the maximum overvoltage is guaranteed between 9% and 32%. Moreover, the two confidence strips show the reliability of the results.

Another case has been considered in which the front time is about 0.4 μs (typical of a subsequent stroke), while the ground wire parameters still vary according to Table 21 . The exam of Figure 70, plotting the two KPIs, highlights that $KPI_{max}$ does not change significantly, while $KPI_{min}$ is much smaller in all the analyzed cases, which means that decreasing the lightning current front time makes the ground wire action less effective. This is related to the fact that the proposed front time is fast enough so that the induced voltage peak will not see the grounding effect. As far as the tuning parameter analysis is concerned, the application of the RSM method (whose details are not reported for the sake of brevity) shows that the optimal configuration in terms of ground wire parameters is the same as the other case.

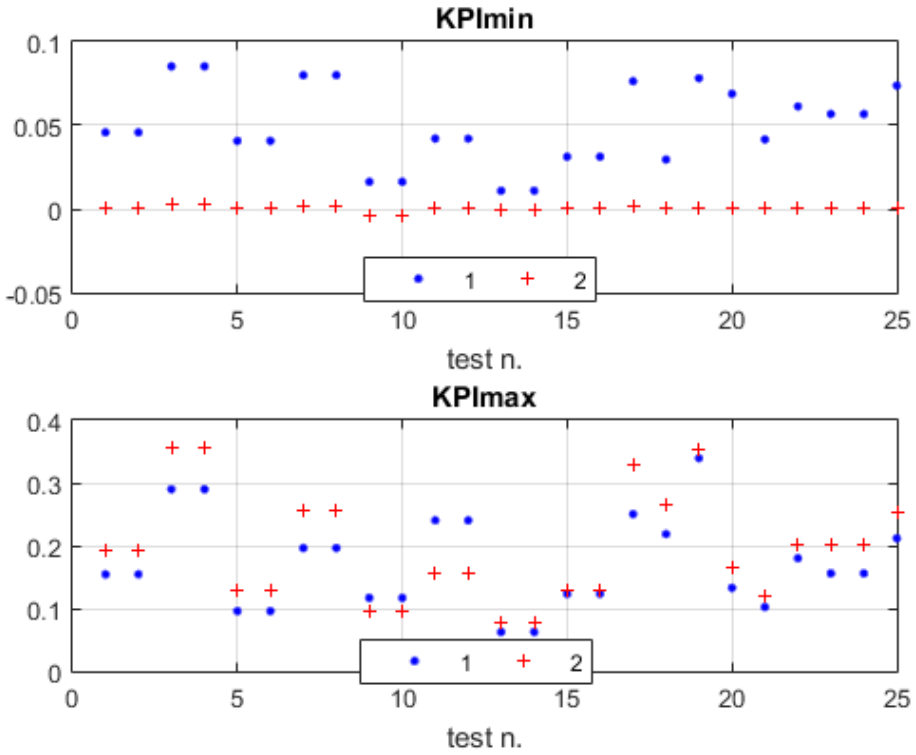


**Figure 70 KPIs with front time of 3.2 µs (test 1 - blue dots) and 0.4 µs (test2 – red dots)**

### 7.3.2 Lightning performance enhancement

In the following, the system lightning performance (i.e. the probability $P_D(V_{\max}^{\bullet} \geq CFO)$ to have an overvoltage $V_{max}$ greater than a prefixed value of the line CFO when the stroke impact point belong to the region D) has been computed according to the approach presented in [35]. A uniform distribution for the stroke position and a log-normal distribution for its peak current have been considered [35] [51]. Consequently, the lightning performance enhancement can be measured by the following KPI that quantifies the gain, in terms of probability, in the j-th test with respect to the base configuration without shield wire:

$$KPI(j,CFO) = \frac{P_D(V_{\max}^{noSW} \geq CFO) - P_D(V_{\max}^{TESTj} \geq CFO)}{P_D(V_{\max}^{noSW} \geq CFO)} \tag{244}$$

Also for this KPI, exploiting the symmetry of the network, the domain *D* can be reduced again to the $D_+$ region defined earlier, considering that

$$P_D(V_{\max}^{TESTj} \geq CFO) = \frac{P_{D_+}(V_{\max}^{TESTj} \geq CFO) + P_{D_+}(V_{\max}^{TESTj^*} \geq CFO)}{2} \tag{245}$$

where $j^*$ is related to j according to (243).

Three different values for *CFO* have been considered, respectively 50, 100 and 150 kV [32], leading to the KPI values appearing in Table 26.

**Table 26 Lightning performance enhancement – KPI results**

| | KPI | | |
|---|---|---|---|
| **Test** | **CFO = 50 kV** | **CFO = 100 kV** | **CFO = 150 kV** |
| *Test 1* | 0.17 | 0.36 | 0.59 |
| *Test 2* | 0.17 | 0.35 | 0.69 |
| *Test 3* | 0.30 | 0.65 | 0.79 |
| *Test 4* | 0.30 | 0.62 | 1.00 |
| *Test 5* | 0.13 | 0.22 | 0.57 |
| *Test 6* | 0.13 | 0.24 | 0.47 |
| *Test 7* | 0.21 | 0.39 | 0.73 |
| *Test 8* | 0.21 | 0.56 | 0.88 |
| *Test 9* | 0.12 | 0.32 | 0.21 |
| *Test 10* | 0.12 | 0.28 | 0.50 |
| *Test 11* | 0.24 | 0.47 | 1.00 |
| *Test 12* | 0.24 | 0.55 | 0.88 |
| *Test 13* | 0.10 | 0.12 | 0.11 |
| *Test 14* | 0.10 | 0.16 | 0.55 |
| *Test 15* | 0.17 | 0.31 | 0.64 |
| *Test 16* | 0.17 | 0.33 | 0.58 |
| *Test 17* | 0.28 | 0.51 | 0.95 |
| *Test 18* | 0.21 | 0.46 | 0.82 |
| *Test 19* | 0.28 | 0.58 | 0.77 |
| *Test 20* | 0.18 | 0.38 | 0.76 |
| *Test 21* | 0.13 | 0.31 | 0.60 |
| *Test 22* | 0.19 | 0.36 | 0.64 |
| *Test 23* | 0.15 | 0.31 | 0.38 |
| *Test 24* | 0.15 | 0.40 | 0.80 |
| *Test 25* | 0.22 | 0.43 | 0.75 |

Analysing the entries of Table 26, one can observe that the lightning performance is at least enhanced by 10%. Moreover, for very high *CFO* values, a 100% improvement is possible; this is basically due to the fact that, when the line insulation level is high, the base case probability is already very small, so that any reduction of the probability can change the *KPI* in a meaningful way.

By applying the RSM to this problem, it is possible to obtain the coefficients of the polynomial relationship (232) between the KPI and the four above defined parameters (Table 27) for each *CFO* case.

**Table 27 Lightning performance enhancement – KPI coefficients**

| | Value | | |
|---|---|---|---|
| **Coefficients** | **CFO = 50 kV** | **CFO = 100 kV** | **CFO = 150 kV** |
| $a_0$ | 0.237176 | 0.462358 | 0.839519 |
| $a_1$ | -0.023223 | -0.048304 | -0.066079 |
| $a_2$ | -0.027930 | -0.078856 | -0.057290 |
| $a_3$ | 0.052172 | 0.112425 | 0.171244 |
| $a_4$ | 0 | 0 | 0 |
| $a_{12}$ | 0.003848 | 0 | 0 |
| $a_{13}$ | 0 | -0.016998 | 0.040552 |
| $a_{14}$ | 0 | 0 | 0 |
| $a_{23}$ | -0.012015 | 0 | -0.033096 |
| $a_{24}$ | 0 | 0 | 0 |
| $a_{34}$ | 0 | 0 | 0 |
| $a_{11}$ | 0.005313 | 0.016199 | 0 |
| $a_{22}$ | 0 | 0.012907 | 0 |
| $a_{33}$ | -0.039791 | -0.084549 | -0.135868 |
| $a_{44}$ | -0.021842 | -0.029747 | -0.063644 |

The relation that links the KPI to the ground wire parameters can be easily obtained from (229) and (232) as follows:

$$\tilde{y} = a_0 + \sum_{i=1}^{4} a_i x_i + \sum_{\substack{i,j=1 \\ i<j}}^{4} a_{ij} x_i x_j + \sum_{i=1}^{4} a_{ii} x_i^2 \qquad (246)$$

where

$$x_1 = (Delta - 200)/100 \quad x_2 = (2R_g - 201)/199$$
$$x_3 = (2h - 19)/5 \quad x_4 = 4y/3 \tag{247}$$

The exam of the coefficient suggests the following considerations:

- No matter the line insulation level, the functional dependence of the system response on the shield wire parameters has always the same form, in which the interaction among the variables is negligible
- As earlier, the dependence of the lightning performance enhancement on the grounding spacing and resistance is almost linear, while the relationship with the horizontal position is purely quadratic so that a symmetry with respect to the axis is confirmed

As in the previous section, for each case an optimal point can be calculated in order to maximize the defined *KPI*. Table 28 reports the optimal point, the best value and its confidence strip at 95% level of confidence.

**Table 28 Lightning performance enhancement: optimal point, best value and confidence strip**

| Case | OPTIMAL POINT | BEST VALUE | CONFIDENCE STRIP (95%) |
|---|---|---|---|
| *CFO* = 50 kV | *Delta* = 100.0 m<br>$R_g$ = 1.0 Ω<br>*h* = 11.5 m<br>*y* = 0.00 m | 0.323 | [0.316, 0.331] |
| *CFO* = 100 kV | *Delta* = 100.0 m<br>$R_g$ = 1.0 Ω<br>*h* = 11.4 m<br>*y* = 0.00 m | 0.668 | [0.646, 0.691] |
| *CFO* = 150 kV | *Delta* = 100.0<br>$R_g$ = 1.0 Ω<br>*h* = 11.0 m<br>*y* = 0.00 m | 1.012 | [0.952, 1.072] |

The proposed *KPI*, in spite of being strongly dependent on the *CFO*, leads substantially to the same optimal configuration for the shield wires in all the three cases. Moreover, the optimal point is practically the same as the one of the previous analysis. Indeed, from a physical point of view, the RSM method looks for the configuration that minimizes the system overvoltage.

The lightning performance evaluation basically consists of a comparison between such overvoltage and a specified threshold (the CFO). As a consequence, it can be expected that the value of the KPI changes, but the values of the shield wire parameters in correspondence of which such value occurs remain essentially the same.

## 7.4 Sensitivity analysis

In order to assess the individual effect of each parameter, some one-dimensional plots are here reported, in which three variables are set to the best value, while the fourth has been varied along the chosen range.

### 7.4.1 Effect of the grounding spacing

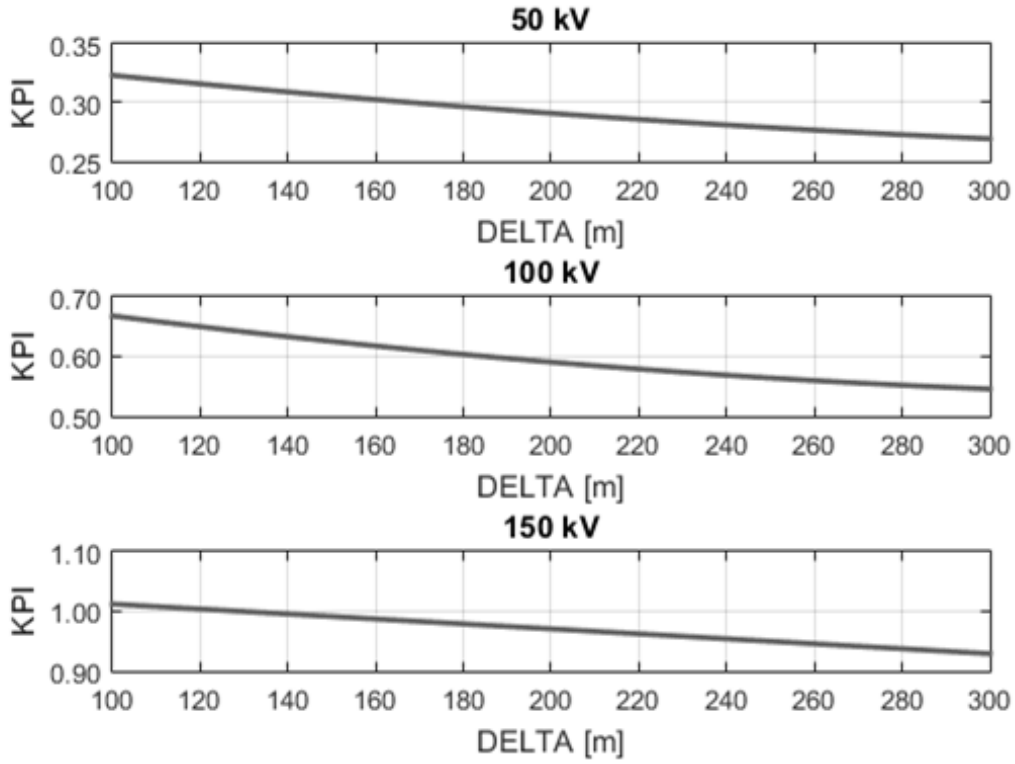


**Figure 71 Grounding spacing effect.**

In Figure 71 the effect of the grounding spacing on the proposed *KPI* is presented for each case of *CFO*. As already highlighted examining the RSM coefficients, the waveform is practically linear with a (negative) mean slope that depends on the *CFO*. For example, at 50 kV the mean slope is 0.03%/m, which means that, increasing the grounding spacing from 100 m to 200 m, the enhancement in the lightning performance moves from about 32% to about 29%.

### 7.4.2 Effect of the grounding resistance

In Figure 72 the effect of the grounding resistance on the proposed *KPI* is presented for each case of *CFO*. As already highlighted examining the RSM coefficients, the waveform is practically linear with a (negative) mean slope that depends on the *CFO*. For example, at 50 kV the mean slope is 0.04%/Ω, which means that, increasing the grounding resistance from 1 Ω to 100 Ω, the enhancement in the lightning performance moves from about 32% to about 28%.

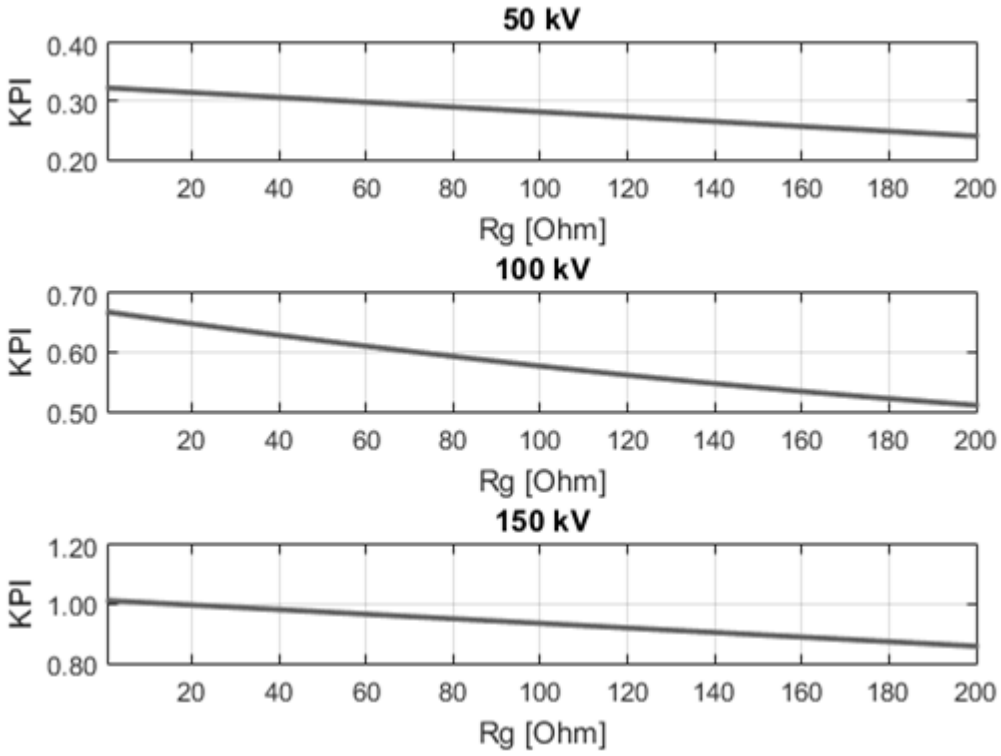


**Figure 72** ***Grounding resistance effect.***

### 7.4.3 Effect of the shield wire height

Figure 73 shows that, for the considered range of shield wire heights, the best results are obtained when the shield wire is posed over the phase conductors, but the exam of the figure allows to conclude that between 10 and 12 m there are no significant variations in the shield wire effectiveness

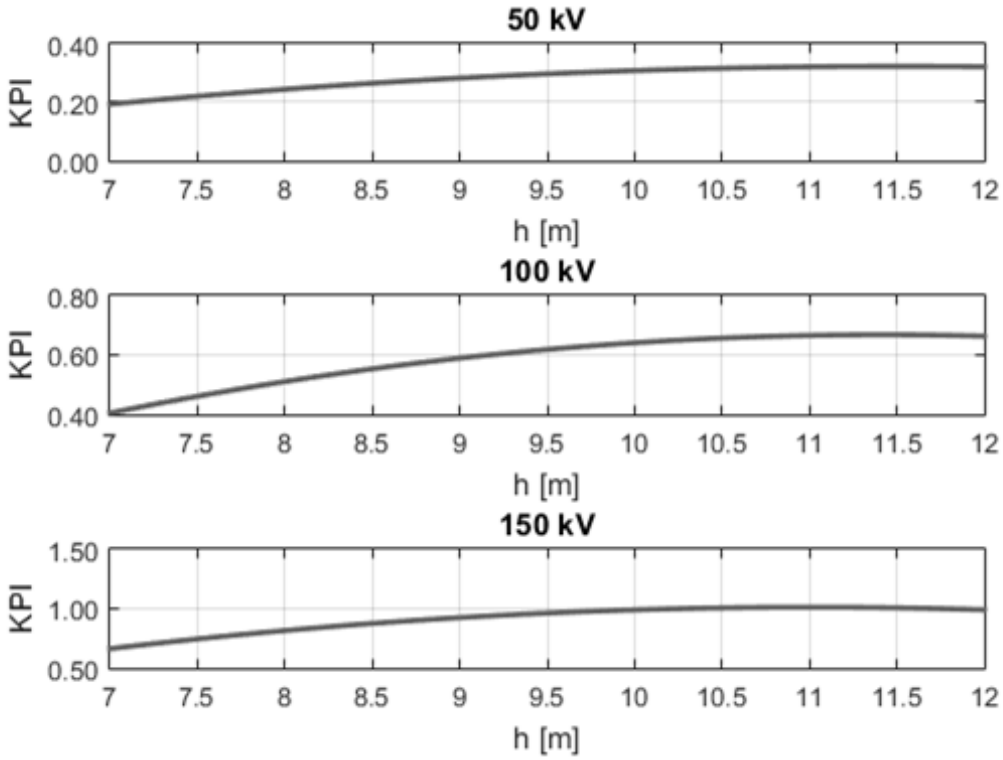


**Figure 73 Shield wire height effect**

### 7.4.4 Effect of the shield wire horizontal position

Concerning the horizontal position of the shield wire, as confirmed by the results of Table 28, the best position is when the shield wire is above the middle phase conductor, with a reduction in the overvoltage mitigation occurring when the shield wire is moved from this position. However, as can be seen from Figure 74, such reduction is quite small, especially for low *CFO* levels.

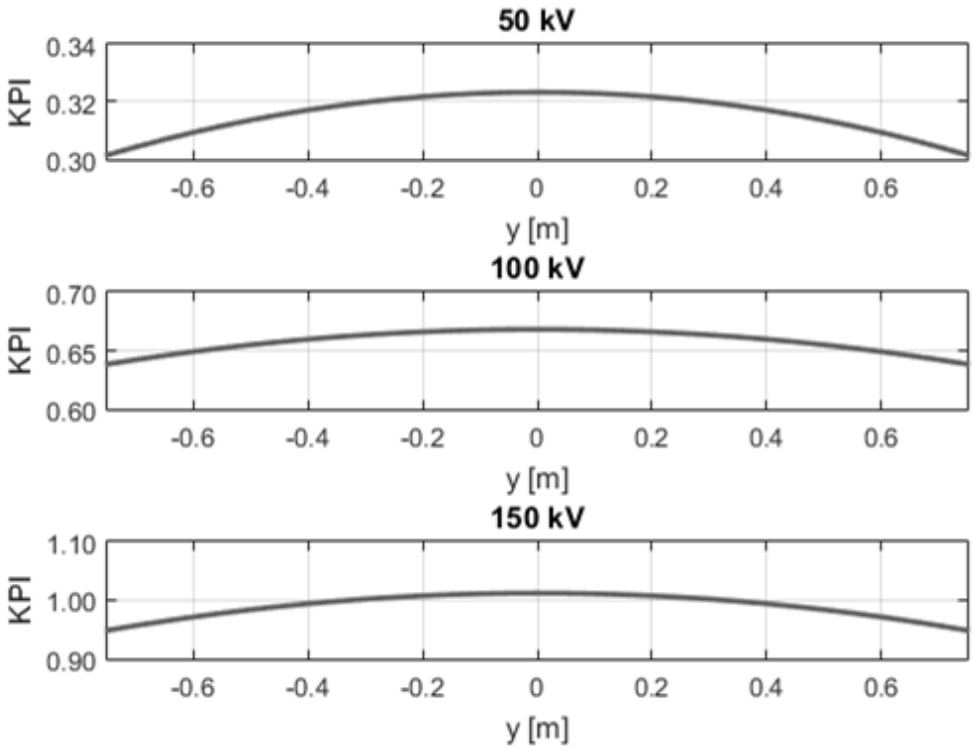


**Figure 74 Shield wire horizontal position effect**

# 8 Conclusions

This thesis has focused on improving the problem of the lightning-induced voltages evaluation in the overhead distribution lines in terms of three main concepts: models innovation, computational effort optimization and introduction of innovative tools.

The model innovation is discussed with the proposal of a new channel base current model aiming at representing in the best way the characteristics of the measured lightning strokes. The validation has shown a good agreement with the already existing models and the main advantages and drawbacks of the new model have been pointed out.

The computational effort optimization has been faced in three different topics: an analytical expression for the electromagnetic fields induced by the lightning current, a new FDTD scheme for the improvement of the stability problem in FDTD-based numerical codes that compute the lightning-induced voltages in distribution lines and the evaluation of a new approach for reducing the computational effort in the lighting performance procedure.

On one side the analytical expression for the electromagnetic fields allows the user to reduce the computational time of at least two orders without losing the precision with respect to the numerical method. On the other hand, the new scheme for the improvement of the stability allows keeping constant the spatial and temporal discretization step in the FDTD scheme even if the considered distribution line is short or present a huge number of discontinuities (poles, surge arresters, …). Finally, the new approach for reducing the computational effort in the lightning performance procedure allows to find a simplified formula for the induced-voltage in a distribution line based on a few number of field-to-line coupling simulations.

The introduction of innovative tools is discussed with the introduction of the application of the RSM method in the mitigation of lightning-induced voltages using shield wires. The method can be used to find the optimal configuration of the shield wire in terms of height, distance from the other conductors, grounding location and grounding resistance.

# 9 Bibliography


[1] "IEEE Guide for Improving the Lightning Performance of Electric Power Overhead Distribution Lines," *IEEE Std 1410-2010 (Revision of IEEE Std 1410-2004)*, pp. 1-73, 2011.

[2] V. Rakov and M. A. Uman, "Review and evaluation of lightning return stroke models including some aspects of their application," *IEEE Trans. Electromagn. Compat*, vol. 40, pp. 403-426, 1998.

[3] M. N. Plooster, "Shock Waves from Line Sources. Numerical Solutions and Experimental Measurements," *The Physics of Fluids*, vol. 13, pp. 2665-2675, 1970.

[4] M. N. Plooster, "Numerical Simulation of Spark Discharges in Air," *The Physics of Fluids*, vol. 14, pp. 2111-2123, 1971.

[5] S. I. Braginskii, "Theory of the Development of a Spark Channel," *Sov. Phys.-Tech. Phys.*, vol. 34, p. 1068, 1958 1958.

[6] R. Moini, S. H. H. Sadeghi, B. Kordi, and F. Rachidi, "An antenna-theory approach for modeling inclined lightning return stroke channels," *Electric Power Systems Research*, vol. 76, pp. 945-952, 2006/07/01/ 2006.

[7] R. Moini, B. Kordi, G. Z. Rafi, and V. A. Rakov, "A new lightning return stroke model based on antenna theory," *Journal of Geophysical Research: Atmospheres*, vol. 105, pp. 29693-29702, 2000.

[8] C. R. Paul, *Analysis of Multiconductor Transmission Lines*: Wiley-IEEE Press, 2007.

[9] K. Berger, "Parameters of lightning flashes," *ELECTRA*, vol. 41, pp. 23-37, 1975 1975.

[10] S. Visacro, A. Soares Jr., M. A. O. Schroeder, L. C. L. Cherchiglia, and V. J. de Sousa, "Statistical analysis of lightning current parameters: Measurements at Morro do Cachimbo Station," *Journal of Geophysical Research: Atmospheres*, vol. 109, 2004.

[11] A. J. Eriksson, "Fifteen Year's Data of Lightning Measurements on a 60m Mast," *Trans S. African Inst. of Elec. Engrs*, vol. 80, pp. 98-103, 1989 1989.

[12] T. Narita, T. Yamada, A. Mochizuki, E. Zaima, and M. Ishii, "Observation of current waveshapes of lightning strokes on transmission towers," *IEEE Transactions on Power Delivery*, vol. 15, pp. 429-435, 2000.

[13] G. Diendorfer, O.-A. H Zhou, K. Stockholm, and H. Pichler, *Review of 10 years of lightning measurement at the Gaisberg Tower in Austria*, 2011.

[14] R. J. Fisher, G. H. Schnetzer, R. Thottappillil, V. A. Rakov, M. A. Uman, and J. D. Goldberg, "Parameters of triggered-lightning flashes in Florida and Alabama," *Journal of Geophysical Research: Atmospheres*, vol. 98, pp. 22887-22902, 1993/12/20 1993.

[15] H. Heidler, "Analytische Blitzstromfunktion zur LEMP-Berechnung," *18th ICLP, Munich, Germany*, 1985.

[16] A. Andreotti, A. Pierno, and L. Verolino, "A New Channel-Base Current Model for Lightning-Induced Voltage Calculations," *IEEE Transactions on Electromagnetic Compatibility*, vol. 61, pp. 617-622, 2019.

[17] V. Javor and P. D. Rancic, "A Channel-Base Current Function for Lightning Return-Stroke Modeling," *IEEE Transactions on Electromagnetic Compatibility*, vol. 53, pp. 245-249, 2011.

[18] C. E. R. Bruce and R. H. Golde, "The lightning discharge," *Journal of the Institution of Electrical Engineers - Part II: Power Engineering,* vol. 88, pp. 487-505, 1941.

[19] M. Brignone, D. Mestriner, R. Procopio, and F. Delfino, "A review on the return stroke engineering models attenuation function: Proposed expressions, validation and identification methods," *Electric Power Systems Research,* vol. 172, pp. 230-241, 2019/07/01/ 2019.

[20] F. Rachidi, C. A. Nucci, M. Ianoz, and C. Mazzetti, "Influence of a lossy ground on lightning-induced voltages on overhead lines," *IEEE Transactions on Electromagnetic Compatibility,* vol. 38, pp. 250-264, 1996.

[21] Vernon Cooray, *Lightning Electromagnetics*: Institution of Engineering and Technology, 2012.

[22] F. Delfino, R. Procopio, M. Rossi, A. Shoory, and F. Rachidi, "Lightning electromagnetic radiation over a stratified conducting ground: Formulation and numerical evaluation of the electromagnetic fields," *Journal of Geophysical Research: Atmospheres,* vol. 116, 2011.

[23] A. Shoory, F. Rachidi, F. Delfino, R. Procopio, and M. Rossi, "Lightning electromagnetic radiation over a stratified conducting ground: 2. Validity of simplified approaches," *Journal of Geophysical Research: Atmospheres,* vol. 116, 2011.

[24] F. Delfino, R. Procopio, M. Rossi, and F. Rachidi, "Influence of frequency-dependent soil electrical parameters on the evaluation of lightning electromagnetic fields in air and underground," *Journal of Geophysical Research Atmospheres,* vol. 114, 2009.

[25] V. Cooray and V. Scuka, "Lightning-induced overvoltages in power lines: validity of various approximations made in overvoltage calculations," *IEEE Transactions on Electromagnetic Compatibility,* vol. 40, pp. 355-363, 1998.

[26] M. Rubinstein, "An approximate formula for the calculation of the horizontal electric field from lightning at close, intermediate, and long range," *IEEE Transactions on Electromagnetic Compatibility,* vol. 38, pp. 531-535, 1996.

[27] F. Delfino, P. Girdinio, R. Procopio, M. Rossi, and F. Rachidi, "Time-Domain Implementation of Cooray–Rubinstein Formula via Convolution Integral and Rational Approximation," *IEEE Transactions on Electromagnetic Compatibility,* vol. 53, pp. 755-763, 2011.

[28] A. Andreotti, F. Rachidi, and L. Verolino, "A New Formulation of the Cooray–Rubinstein Expression in Time Domain," *IEEE Transactions on Electromagnetic Compatibility,* vol. 57, pp. 391-396, 2015.

[29] A. Andreotti, F. Rachidi, and L. Verolino, "Some Developments of the Cooray–Rubinstein Formula in the Time Domain," *IEEE Transactions on Electromagnetic Compatibility,* vol. 57, pp. 1079-1085, 2015.

[30] C. Caligaris, F. Delfino, and R. Procopio, "Cooray–Rubinstein Formula for the Evaluation of Lightning Radial Electric Fields: Derivation and Implementation in the Time Domain," *IEEE Transactions on Electromagnetic Compatibility,* vol. 50, pp. 194-197, 2008.

[31] A. K. Agrawal, H. J. Price, and S. H. Gurbaxani, "Transient response of multiconductor transmission lines excited by a nonuniform electromagnetic," *IEEE Transactions on Electromagnetic Compatibility,* vol. 22, pp. 119-129, 1980.

[32] A. Borghetti, C. A. Nucci, and M. Paolone, "An Improved Procedure for the Assessment of Overhead Line Indirect Lightning Performance and Its Comparison with the IEEE Std. 1410 Method," *IEEE Transactions on Power Delivery*, vol. 22, pp. 684-692, 2007.

[33] A. Borghetti, C. A. Nucci, and M. Paolone, "Indirect-Lightning Performance of Overhead Distribution Networks With Complex Topology," *IEEE Transactions on Power Delivery*, vol. 24, pp. 2206-2213, 2009.

[34] M. Brignone, F. Delfino, R. Procopio, M. Rossi, and F. Rachidi, "Evaluation of Power System Lightning Performance,Part I: Model and Numerical Solution Using the PSCAD-EMTDC Platform," *IEEE Transactions on Electromagnetic Compatibility*, vol. 59, 2017.

[35] M. Brignone, F. Delfino, R. Procopio, M. Rossi, and F. Rachidi, "Evaluation of Power System Lightning Performance Part II: Application to an Overhead Distribution Network," *IEEE Transactions on Electromagnetic Compatibility*, vol. 59, pp. 146-153, 2017.

[36] F. Napolitano, "An Analytical Formulation of the Electromagnetic Field Generated by Lightning Return Strokes," *IEEE Transactions on Electromagnetic Compatibility*, vol. 53, pp. 108-113, 2011.

[37] A. Borghetti, F. Napolitano, C. A. Nucci, and F. Tossani, "Influence of the Return Stroke Current Waveform on the Lightning Performance of Distribution Lines," *IEEE Transactions on Power Delivery*, vol. 32, pp. 1800-1808, 2017.

[38] S. Rusck, *Induced Lightning Over-voltages on Power-transmission Lines With Special Reference to the Over-voltage Protection of Low-voltage Networks*: Lindståhl, 1957.

[39] H. D. Hoidalen, "Lightning-induced overvoltages in low-voltage systems," *PhD Dissertation Norwegian Univ. Sci. Technol.*, 1997.

[40] H. K. Hoidalen, "Calculation of lightning-induced overvoltages using MODELS," in *Proc. Fourth Int. Conf. Power Syst. Transients,*, Budapest, 1999.

[41] H. K. Hoidalen, "Analyitical formulation of lightning-induced voltages on multiconductor overhead lines above lossy ground," *IEEE Transactions on Electromagnetic Compatibility*, vol. 45, pp. 92-100, 2003.

[42] H. K. Hoidalen, "Calculation of lightning-induced overvoltages in MODELS including lossy ground effects," in *Proc. Int. Conf. Power Syst. Transients,*, New Orleans, 2003.

[43] A. Andreotti, A. Pierno, and V. A. Rakov, "A new tool for calculation of lightning induced voltages in power system - Part I: Development of circuit model," *IEEE Transactions on Power Delivery*, vol. 30, pp. 326-333, 2015.

[44] A. Andreotti, A. Pierno, and V. A. Rakov, "A New Tool for Calculation of Lightning-Induced Voltages in Power Systems Part II: Validation Study," *IEEE Transactions on Power Delivery*, vol. 30, pp. 334-341, 2015.

[45] A. C. Nucci, M. Paolone, and F. Rachidi, "A new finite difference time domain scheme for the evaluation of lightning induced overvoltage on multiconductor overhead lines," in *Int. Conf. Power System Transients* Rio De Janeiro, Brazil, 2001.

[46] M. Paolone, *Modeling of lightning-induced voltages on distribution networks for the solution of power quality problems, and relevant implementation in a tranisent program*. Bologna: Dept. Elect. Eng. Univ. Bologna, 2002.

[47] A. Borghetti, J. A. Gutierrez, A. C. Nucci, M. Paolone, E. Petrache, and F. Rachidi, "Lightning-induced voltages on complex distribution systems:Models, advanced software tools and experimental validation," *J. Electrostatics*, vol. 60, pp. 163-174, 2004.

[48] M. Paolone, F. Rachidi, M. Borghetti, C. A. Nucci, M. Rubinstein, V. A. Rakov, *et al.*, "Lightning Electromagnetic Field Coupling to Overhead Lines: Theory, Numerical Simulations, and Experimental Validation," *IEEE Transactions on Electromagnetic Compatibility*, vol. 51, pp. 532-547, 2009.

[49] F. Napolitano, A. Borghetti, C. A. Nucci, and M. Paolone, "An advanced interface between the LIOV code and the EMPT-RV," in *29th Conference Lightning protection*, Uppala,Sweden, 2008.

[50] M. Brignone, D. Mestriner, R. Procopio, A. Piantini, and F. Rachidi, "Evaluation of the Mitigation Effect of the Shield Wires on Lightning Induced Overvoltages in MV Distribution Systems Using Statistical Analysis," *IEEE Transactions on Electromagnetic Compatibility*, 2017.

[51] C. A. Nucci, "A survey on Cigré and IEEE procedures for the estimation of the lightning performance of overhead transmission and distribution lines," in *2010 Asia-Pacific International Symposium on Electromagnetic Compatibility*, 2010, pp. 1124-1133.

[52] E. Cinieri and F. Muzi, "Lightning induced overvoltages, improvement in quality of service in MV distribution lines by addition of shield wires," *IEEE Transactions on Power Delivery*, vol. 11, pp. 361-372, 1996.

[53] F. Rachidi, C. A. Nucci, and M. Ianoz, "Transient analysis of multiconductor lines above a lossy ground," *IEEE Transactions on Power Delivery*, vol. 14, pp. 294-302, 1999.

[54] A. Piantini and J. M. Janiszewski, "The use of shield wires for reducing induced voltages from lightning electromagnetic fields," *Electric Power Systems Research*, vol. 94, pp. 46-53, 2013.

[55] S. Yokoyama, "Calculation of Lightning-Induced Voltages on Overhead Multiconductor Systems," *IEEE Transactions on Power Apparatus and Systems*, vol. PAS-103, pp. 100-108, 1984.

[56] S. Yokoyama, K. Yamamoto, and H. Kinoshita, "Analogue simulation of lightning induced voltages and its application for analysis of overhead-ground-wire effects," *IEE Proceedings C - Generation, Transmission and Distribution*, vol. 132, pp. 208-216, 1985.

[57] S. Yokoyama, K. Miyake, H. Mitani, and A. Takanishi, "Simultaneous Measurement of Lightning Induced Voltages with Associated Stroke Currents," *IEEE Transactions on Power Apparatus and Systems*, vol. PAS-102, pp. 2420-2429, 1983.

[58] A. Piantini, J. M. Janiszewski, A. Borghetti, C. A. Nucci, and M. Paolone, "A Scale Model for the Study of the LEMP Response of Complex Power Distribution Networks," *IEEE Transactions on Power Delivery*, vol. 22, pp. 710-720, 2007.

[59] I. Bendato, M. Brignone, F. Delfino, R. Procopio, and F. Rachidi, "A Methodology to Reduce the Computational Effort in the Evaluation of the Lightning Performance of Distribution Networks," in *Atmosphere*, 2016.

[60] M. Darveniza, "A Practical Extension of Rusck's Formula for Maximum Lightning-Induced Voltages That Accounts for Ground Resistivity," *IEEE Transactions on Power Delivery,* vol. 22, pp. 605-612, 2007.

[61] M. Brignone, D. Mestriner, R. Procopio, A. Piantini, and F. Rachidi, "On the Stability of FDTD-Based Numerical Codes to Evaluate Lightning-Induced Overvoltages in Overhead Transmission Lines," *IEEE Transactions on Electromagnetic Compatibility,* pp. 1-8, 2019.

[62] H. M. Ren, B. H. Zhou, V. A. Rakov, L. H. Shi, C. Gao, and J. H. Yang, "Analysis of Lightning-Induced Voltages on Overhead Lines Using a 2-D FDTD Method and Agrawal Coupling Model," *IEEE Transactions on Electromagnetic Compatibility,* vol. 50, pp. 651-659, 2008.

[63] A. Piantini, "Analysis of the effectiveness of shield wires in mitigating lightning-induced voltages on power distribution lines," *Electric Power Systems Research,* 2017.

[64] V. A. Rakov and M. A. Uman, "Review and evaluation of lightning return stroke models including some aspects of their application," *IEEE transactions on electromagnetic compatibility,* vol. 40, pp. 403-426, 1998.

[65] R. Procopio and M. Brignone, "The return stroke current attenuation function: Available models and identification methods from field measurements," in *2017 International Symposium on Lightning Protection (XIV SIPDA)*, 2017, pp. 402-412.

[66] M. A. Uman and D. K. McLain, "Magnetic field of lightning return stroke," *Journal of Geophysical Research,* vol. 74, pp. 6899-6910, 1969.

[67] V. Rakov and A. Dulzon, "Results of the calculation of the electromagnetic fields of lightning discharges(Rezul'taty rascheta elektromagnitnykh polei grozovykh razriadov)," *Tekhnicheskaia Elektrodinamika,* pp. 87-89, 1987.

[68] C. A. Nucci, C. Mazzetti, F. Rachidi, and M. Ianoz, "On lightning return stroke models for LEMP calculations," in *19th International Conference on lightning protection*, 1988.

[69] V. Javor, "Modified Transmission Line Models of Lightning Strokes Using New Current Functions and Attenuation Factors," in *Engineering Mathematics I*, ed: Springer, 2016, pp. 131-149.

[70] F. Heidler, "Traveling current source model for LEMP calculation," *Proc. of 6th EMC Symp., Zurich,* 1985 1985.

[71] G. Diendorfer and M. Uman, "An improved return stroke model with specified channel-base current," *Journal of Geophysical Research: Atmospheres,* vol. 95, pp. 13621-13644, 1990.

[72] A. Andreotti and L. Verolino, "A New Channel-Base Current Function for Lightning Studies," *IEEE Transactions on Electromagnetic Compatibility,* vol. 57, pp. 1539-1546, 2015.

[73] C. A. Nucci, G. Diendorfer, M. A. Uman, F. Rachidi, M. Ianoz, and C. Mazzetti, "Lightning return stroke current models with specified channel-base current: A review and comparison," *Journal of Geophysical Research: Atmospheres,* vol. 95, pp. 20395-20408, 1990.

[74] C. A. Nucci and F. Rachidi, "Interaction of electromagnetic fields with electrical networks generated by lightning," in *The Lightning Flash: Physical and Engineering Aspects*. vol. Chapter 8, ed: IEE Press, 2003.

[75] F. H. Silveira, A. D. Conti, and S. Visacro, "Evaluation of Lightning-Induced Voltages over Lossy Ground with Frequency-dependent Soil Parameters," in *2014 International Conference on Lightning Protection (ICLP)*, 2014, pp. 950-954.

[76] F. Delfino, R. Procopio, M. Rossi, F. Rachidi, and C. A. Nucci, "Lightning return stroke current radiation in presence of a conducting ground: 2. Validity assessment of simplified approaches," *Journal of Geophysical Research: Atmospheres*, vol. 113, pp. n/a-n/a, 2008.

[77] Q. Zhang, L. Zhang, X. Tang, and J. Gao, "An Approximate Formula for Estimating the Peak Value of Lightning-Induced Overvoltage Considering the Stratified Conducting Ground," *IEEE Transactions on Power Delivery*, vol. 29, pp. 884-889, 2014.

[78] J. O. S. Paulino, C. F. Barbosa, I. J. S. Lopes, and W. d. C. Boaventura, "An Approximate Formula for the Peak Value of Lightning-Induced Voltages in Overhead Lines," *IEEE Transactions on Power Delivery*, vol. 25, pp. 843-851, 2010.

[79] S. Tkatchenko, F. Rachidi, and M. Ianoz, "Electromagnetic field couplingto a line of finite length: Theory and fast iterative solutions in frequency and time domains," *IEEE Trans. Electromagn.Compat.*, vol. 37, pp. 509-518, 1995.

[80] S. Tkatchenko, F. Rachidi, and M. Ianoz, "High-frequency electromagnetic field coupling to long terminated lines," *IEEE Trans. Electromagn.*, vol. 43, pp. 117-129, 2001.

[81] F. Rachidi, S. L. Loyka, C. A. Nucci, and M. Ianoz, "A new expression for the ground transient resistance matrix elements of multiconductor overhead transmission lines," *Electric Power Systems Research*, vol. 65, pp. 41-46, 2003/04/01/ 2003.

[82] L. Bewley, "Traveling waves due to lightning," *Transactions of the American Institute of Electrical Engineers*, vol. 48, pp. 1050-1064, 1929.

[83] Z. Feizhou and L. Shanghe, "A new function to represent the lightning return-stroke currents," *IEEE transactions on electromagnetic compatibility*, vol. 44, pp. 595-597, 2002.

[84] F. Heidler, J. M. Cvetic, and B. V. Stanic, "Calculation of lightning current parameters," *IEEE Transactions on Power Delivery*, vol. 14, pp. 399-404, 1999.

[85] A. Andreotti, S. Falco, and L. Verolino, "Some integrals involving Heidler's lightning return stroke current expression," *Electrical Engineering*, vol. 87, pp. 121-128, 2005.

[86] D. S. Prasad and G. S. Punekar, "Concerning channel base current functions for lightning studies," *IEEE transactions on electromagnetic compatibility*, vol. 54, pp. 1318-1320, 2012.

[87] A. Smorgonskiy, F. Rachidi, M. Rubinstein, N. V. Korovkin, and A. P. Vassilopoulos, "Are standardized lightning current waveforms suitable for aircraft and wind turbine blades made of composite materials?," *IEEE transactions on electromagnetic compatibility*, vol. 59, pp. 1320-1328, 2017.

[88] F. Delfino, R. Procopio, M. Rossi, and F. Rachidi, "Prony Series Representation for the Lightning Channel Base Current," *IEEE Transactions on Electromagnetic Compatibility*, vol. 54, pp. 308-315, 2012.

[89] C. A. Akemann, "The general Stone-Weierstrass problem," *Journal of Functional Analysis*, vol. 4, pp. 277-294, 1969.

[90] A. Khovanskii and S. Yakovenko, "Generalized Rolle theorem in ℝ n and ℂ," *Journal of Dynamical and Control Systems*, vol. 2, pp. 103-123, 1996.

[91] F. Rachidi and C. A. Nucci, "On the Master, Uman, Lin, Standler and the Modified Transmission Line Lightning return stroke current models," *Journal of Geophysical Research: Atmospheres*, vol. 95, pp. 20389-20393, 1990.

[92] ABB, "Overvoltage protection: Metal oxide surge arresters medium voltage systems," ed, 2011.

[93] V. Mashayekhi, R. Moini, and S. H. H. Sadeghi, "The effect of the lightning return stroke speed on voltages induced on nearby overhead lines," in *2010 30th International Conference on Lightning Protection (ICLP)*, 2010, pp. 1-3.

[94] G. E. P. Box and N. R. Draper, *Response Surfaces, Mixtures, and Ridge Analyses*: Wiley, 2007.

[95] I. Kaymaz and C. A. McMahon, "A response surface method based on weighted regression for structural reliability analysis," *Probabilistic Engineering Mechanics*, vol. 20, pp. 11-17, 2005.

[96] S. Gupta and C. S. Manohar, "An improved response surface method for the determination of failure probability and importance measures," *Structural Safety*, vol. 26, pp. 123-139, 2004.

[97] L. Ying Wei and F. Moses, "A sequential response surface method and its application in the reliability analysis of aircraft structural systems," *Structural Safety*, vol. 16, pp. 39-46, 1994.

[98] L. Faravelli, "Response Surface Approach for Reliability Analysis," *Journal of Engineering Mechanics*, vol. 115, pp. 2763-2781, 1989.

[99] N. Gayton, J. M. Bourinet, and M. Lemaire, "CQ2RS: a new statistical approach to the response surface method for reliability analysis," *Structural Safety*, vol. 25, pp. 99-121, 2003/01/01/ 2003.

[100] O. Ekren and B. Y. Ekren, "Size optimization of a PV/wind hybrid energy conversion system with battery storage using response surface methodology," *Applied Energy*, vol. 85, pp. 1086-1101, 2008/11/01/ 2008.

[101] Z. Ren, W. Li, R. Billinton, and W. Yan, "Probabilistic Power Flow Analysis Based on the Stochastic Response Surface Method," *IEEE Transactions on Power Systems*, vol. 31, pp. 2307-2315, 2016.

[102] Y. Tan and R. Ma, "Stochastic optimal power flow with wind generator based on stochastic response surface method (SRSM) and interior point methods," in *2015 5th International Conference on Electric Utility Deregulation and Restructuring and Power Technologies (DRPT)*, 2015, pp. 2079-2083.

[103] J. C. Davis, K. Vasanth, S. Saxena, P. K. Mozumder, S. Rao, C. L. Fernando, *et al.*, "Method and system for using response-surface methodologies to determine optimal tuning parameters for complex simulators," ed: Google Patents, 2002.

[104] M. Akbari, K. Sheshyekani, A. Pirayesh, F. Rachidi, M. Paolone, A. Borghetti, *et al.*, "Evaluation of lightning electromagnetic fields and their induced voltages on overhead lines considering the frequency dependence of soil electrical parameters," *IEEE Transactions on Electromagnetic Compatibility*, vol. 55, pp. 1210-1219, 2013.

[105] D. Cavka, N. Mora, and F. Rachidi, "A Comparison of frequency-dependent soil models: Application to the analysis of grounding systems," *IEEE Transactions on Electromagnetic Compatibility,* vol. 56, pp. 177-187, 2014.

# 10 PhD Publications

[1] M. Brignone, D. Mestriner, R. Procopio, A. Piantini, and F. Rachidi, "Evaluation of the Mitigation Effect of the Shield Wires on Lightning Induced Overvoltages in MV Distribution Systems Using Statistical Analysis," *IEEE Transactions on Electromagnetic Compatibility*, 2017.

[2] A. Bonfiglio, F. Delfino, A. Labella, D. Mestriner, F. Pampararo, R. Procopio, *et al.*, "Modeling and Experimental Validation of an Islanded No-Inertia Microgrid Site," *IEEE Transactions on Sustainable Energy*, vol. 9, pp. 1812-1821, 2018.

[3] A. Bonfiglio, M. Brignone, M. Invernizzi, A. Labella, D. Mestriner, and R. Procopio, "A Simplified Microgrid Model for the Validation of Islanded Control Logics," *Energies*, vol. 10, p. 1141, 2017.

[4] M. Brignone, D. Mestriner, R. Procopio, A. Piantini, and F. Rachidi, "On the Stability of FDTD-Based Numerical Codes to Evaluate Lightning-Induced Overvoltages in Overhead Transmission Lines," *IEEE Transactions on Electromagnetic Compatibility*, pp. 1-8, 2019.

[5] A. Labella, D. Mestriner, R. Procopio, and F. Delfino, "A simplified first harmonic model for the Savona Campus Smart Polygeneration Microgrid," in *2017 IEEE International Conference on Environment and Electrical Engineering and 2017 IEEE Industrial and Commercial Power Systems Europe (EEEIC / I&CPS Europe)*, 2017, pp. 1-6.

[6] A. Labella, D. Mestriner, R. Procopio, and M. Brignone, "A new method to evaluate the stability of a droop controlled micro grid," in *2017 10th International Symposium on Advanced Topics in Electrical Engineering (ATEE)*, 2017, pp. 448-453.

[7] F. Blanco, A. Labella, D. Mestriner, and A. Rosini, "Model Predictive Control for Primary Regulation of Islanded Microgrids," in *2018 IEEE International Conference on Environment and Electrical Engineering and 2018 IEEE Industrial and Commercial Power Systems Europe (EEEIC / I&CPS Europe)*, 2018, pp. 1-6.

[8] A. Labella, D. Mestriner, F. Pampararo, and R. Procopio, "Measurement campaign and experimental results of an islanded microgrid," in *2017 International Conference on ENERGY and ENVIRONMENT (CIEM)*, 2017, pp. 31-35.

[9] M. Brignone, E. Ginnante, D. Mestriner, L. Ruggi, R. Procopio, A. Piantini, *et al.*, "Evaluation of lightning-induced overvoltages on a distribution system: Validation of a dedicated code using experimental results on a reduced-scale model," in *2017 IEEE International Conference on Environment and Electrical Engineering and 2017 IEEE Industrial and Commercial Power Systems Europe (EEEIC / I&CPS Europe)*, 2017, pp. 1-6.

[10] M. Brignone, D. Mestriner, R. Procopio, F. Rachidi, and A. Piantini, "Mitigation of Lightning-Induced Overvoltages Using Shield Wires: Application of the Response Surface Method," in *2018 34th International Conference on Lightning Protection (ICLP)*, 2018, pp. 1-6.

[11] D. Mestriner, "Analysis of the Impact of the Lightning Return Stroke Models on Overhead Transmission Lines Induced Voltages," in *2018 IEEE Symposium on*

*Electromagnetic Compatibility, Signal Integrity and Power Integrity (EMC, SI & PI)*, 2018, pp. 351-356.

[12] M. Brignone, D. Mestriner, R. Procopio, D. Javor, and V. Javor, "Lightning Induced Voltages on Overhead Lines for Different Return Stroke Engineering Models," in *2018 International Symposium on Electromagnetic Compatibility (EMC EUROPE)*, 2018, pp. 1-6.

[13] M. Brignone, D. Mestriner, R. Procopio, and F. Delfino, "A review on the return stroke engineering models attenuation function: Proposed expressions, validation and identification methods," *Electric Power Systems Research*, vol. 172, pp. 230-241, 2019/07/01/ 2019.

[14] D. Mestriner, A. Labella, A. Bonfiglio, I. Benfatto, J. Li, Y. Ye, *et al.*, "ITER Reactive Power Compensation Systems: analysis on reactive power sharing strategies," in *2019 IEEE International Conference on Environment and Electrical Engineering and 2019 IEEE Industrial and Commercial Power Systems Europe (EEEIC / I&CPS Europe)*, 2019, pp. 1-6.

[15] D. Mestriner, M. Nicora, R. Procopio, M. Brignone, M. Rossi, F. Delfino, *et al.*, "Lightning Current Parameters Effects on the Induced Overvoltages in Transmission Lines," in *2019 IEEE International Conference on Environment and Electrical Engineering and 2019 IEEE Industrial and Commercial Power Systems Europe (EEEIC / I&CPS Europe)*, 2019, pp. 1-5.

[16] M. Brignone, D. Mestriner, R. Procopio, M. Rossi, A. Piantini, and F. Rachidi, "EM Fields Generated by a Scale Model Helical Antenna and Its Use in Validating a Code for Lightning-Induced Voltage Calculation," *IEEE Transactions on Electromagnetic Compatibility*, pp. 1-10, 2019.

[17] D. Mestriner and M. Invernizzi, "Analysis of lightning effects on power plant connection," *International Journal of Power and Energy Systems*, vol. 38, pp. 40-49, 2018.

[18] A. Bonfiglio, A. Labella, D. Mestriner, F. Milani, R. Procopio, and Y. Ye, "ITER Fast Discharging Units: A Black Box Model Approach for Circuital Simulations," in *2018 IEEE International Conference on Environment and Electrical Engineering and 2018 IEEE Industrial and Commercial Power Systems Europe (EEEIC / I&CPS Europe)*, 2018, pp. 1-7.